12-2009

INTER-TUBE BONDING AND DEFECTS IN CARBON NANOTUBES AND THE IMPACT ON THE TRANSPORT PROPERTIES AND MICRO-MORPHOLOGY

Keqin Yang
Clemson University, kyang@clemson.edu

Recommended Citation
Yang, Keqin, "INTER-TUBE BONDING AND DEFECTS IN CARBON NANOTUBES AND THE IMPACT ON THE TRANSPORT PROPERTIES AND MICRO-MORPHOLOGY" (2009). *All Dissertations*. 487.
https://tigerprints.clemson.edu/all_dissertations/487

INTER-TUBE BONDING AND DEFECTS IN CARBON NANOTUBES AND THE IMPACT ON THE TRANSPORT PROPERTIES AND MICRO-MORPHOLOGY

A Thesis
Presented to
the Graduate School of
Clemson University

In Partial Fulfillment
of the Requirements for the Degree
Doctor of Philosophy
Physics

---

by
Keqin Yang
December 2009

Accepted by:
Dr. Apparao M. Rao, Committee Chair
Dr. Malcolm J. Skove
Dr. Terry M. Tritt
Dr. Jian He

ABSTRACT

The transport properties of the carbon nanotubes (CNTs) are affected by the tube-tube interaction and the defects presented in the system. Inter-tube bonding, formed during spark plasma sintering (SPS) process, lowers the electrical/thermal resistivity at the tube-tube junctions and also causes new scattering mechanisms such as strong electron-phonon coupling (EPC) at low temperature. More evidences have been found by changing the SPS temperature and doping the CNTs to support the electron-phonon coupling is Kohn anomaly (KA) in as-SPSed CNTs. The phonon drag, appearing in thermoelectric power (TEP) of the as-SPSed CNTs at low temperature, can be explained in the framework of the KA. The thermal property of CNTs exhibits nearly two dimensional character when the inter-tube bonding is stronger. When orientated CNTs are SPSed, one of the highest thermal conductivity ~ 31 W/(m-K) reported in CNT bulk samples is achieved.

In certain cases, defects in the CNTs not only change the transport properties but also modify the morphology of the CNTs. Helically coiled carbon nanotubes (HCNTs) and nanowires (HCNWs) are exact examples. A rational synthesis of HCNT/HCNW using In and Sn as catalyst in a thermal chemical vapor deposition (CVD) system has been demonstrated. A thermodynamic model has been proposed, where helix/coil formation is explained on the basis of the interactions between the specific catalyst particles and the growing nanostructure. While a model based on the mutual solubility of Fe with Sn and In, could explain the growth mechanism difference between the HCNTs and the HCNWs. Experimental results agree with these models qualitatively well.

DEDICATION

To my beloved wife, Ping, and my lovable son, Jiayi.

ACKNOWLEDGMENTS

I would like to express my sincere gratitude to my advisor, Dr. Apparao M. Rao for his endless encouragement and support during my graduate career. His guidance and confidence in me has helped me accomplish my goal and tackle obstacles in academic research. I have learnt a lot from him and he continues to inspire me to do better in my work. I would also like to thank Dr. Jian He. His broad knowledge in transport provides invaluable help in data analysis. I also express my appreciation to Dr. Malcolm Skove for his valuable suggestions both in research and English writing. I would like to thank my fellow students Jason Reppert, Hitchcock Dale Austin, Zhe Su and Pooja Puneet for their guidance with synthesis and transport experiments. I would like to thank Dr. Zakhidov's group at UT Dallas for the magnetization measurements and Dr. P. R. Bandaru for his help in building a thermodynamic model for the synthesis of nanocoils. I would like to thank Dr. Jay Gaillard for providing MWCNT buckypaper for my research. I also would like to thank Dr. Terry Tritt for providing access to the SPS system. Without this system, half of the work described in this thesis could not be accomplished.

I would like to thank my parents, my sister and brother at home for supporting me through these years and, thanks to all the present and past Rao's group members.

At last, to all of those who gave their friendship and support throughout my graduate career- I offer my deepest and most sincere gratitude to them.

TABLE OF CONTENTS

Page

CHAPTER

Table of Contents (Continued)

Page

Table of Contents (Continued)

Page

LIST OF TABLES

Table Page

LIST OF FIGURES

List of Figures (Continued)

Figure Page

List of Figures (Continued)

Figure Page

Figure Page

List of Figures (Continued)

Figure Page

List of Figures (Continued)

Figure Page

List of Figures (Continued)

Figure Page

List of Figures (Continued)

CHAPTER ONE

INTRODUCTION

Carbon nanotubes (CNTs) have attracted an enormous attention from the fundamental science and the technical point of view since their discovery by Iijima in 1991 [2]. In topology, a CNT is the result of rolling a graphene sheet into a seamless cylinder with quasi-one-dimensional properties. The one-dimensional nature and unique electrical, chemical and mechanical properties of CNT promise versatile potential applications in composite functional materials and nanotube-based microdevices. In terms of the number of concentric graphene layers, there are two basic types of CNT, single-walled carbon nanotubes (SWCNTs) and multi-walled carbon naotubes (MWCNTs). The SWCNT consists of a single rolled graphene sheet involving only bezene-like hexagonal rings. On the other hand, MWCNTs can be geometrically described as multiple nested cylinders consisting of rolled graphene sheets. Theoretical works predicted that the electronic properties of "ideal" CNTs depend on their diameter and chirality [3]. Note that, CNTs are probably not as perfect as they were once thought to be. Inter-tube bonding [4] [5] and defects (such as pentagons, heptagons, dopant, etc.) [6] are found to modify drastically the electronic properties of these nano-systems. The presence of defects also reflect in the morphology of CNT, for example, CNTs with a straight cylinder shape can be transformed to a helically coiled carbon nanotube (HCNTs) by periodically insert pentagon-heptagon pairs into the seamless hexagonal network [7].

Technically, high energy processes such as electron/ion irradiation, thermal/high current treatment, and plasma etching can introduce defects in CNTs and/or modify the morphology of CNTs on the intra- and inter-tube levels. Inserting atoms other than carbon into carbon network of CNTs during the synthesis process has also been reported; however there are few reports about the effects of structure modification on the electron/phonon transport properties of CNTs. A systematic study of how inter-tube bonding and defects affect the transport properties of CNT is highly desirable and is the focus of this thesis.

Spark Plasma Sintering (SPS), also known as field assisted sintering technique (FAST) or pulsed electric current sintering (PECS), is a novel sintering technique. This is a pressure assisted fast sintering method based on a high-temperature plasma (spark plasma) momentarily generated in the gaps between powdered materials by electrical discharge during on–off d.c. pulsing. This method has been effectively used in the transformation of sp^2 bonded MWCNTs to sp^3 bonded micro-diamonds or graphitization and formation of crystalline-amorphous carbon hetero-junctions in amorphous carbon fibers.

In this thesis, the morphology and transport property of CNTs after the SPS process are studied. Defects are formed during SPS process which leads to formation of kinks, corrugation, and collapse of sidewalls in CNTs. Furthermore, carbon atoms in sidewalls of CNTs are rearranged at certain points and inter-tube bonding is formed. The SPS-induced inter-tube bonding improves the transport of electron/phonon in CNT network, but also introduces new scattering mechanism. Enhanced electron-phonon coupling (EPC) is observed at low temperatures. One manifestation of the EPC is the Kohn anomaly (KA), which has been theoretically predicted in graphite/CNTs system. Our study strongly supports the presence of the KA in the as-SPSed CNT samples. Superconductivity in boron doped SWCNTs has been reported by our group recently, in which SWNCTs are doped with boron atoms during the synthesis process. In this thesis, we explore the possibility of inserting dopants into carbon network of CNTs during the SPS process. Considering the strong EPC in as-SPSed CNTs we expect to realize superconductivity in the as-SPSed boron doped CNTs mediated through the formation of Copper pairs.

Three dimensional (3-D) carbon nanostructures such as helically coiled carbon nanowires (HCNWs) and helically coiled carbon nanotubes (HCNTs) have attracted increasing attention in carbon science. Due to their unique morphologies, they are expected to exhibit extraordinary structural, mechanical and electrical properties which may enable realization of potential devices such as the electromagnetic wave absorbers, nanosprings for microelectromechanical systems (MEMS) and nanoelectromecahnical systems (NEMS). A liquid-precursor-based synthesis method for HCNT/HCNW is also presented in this thesis. Bulk quantities of high purity HCNTs and HCNWs can be produced using this method. A thermodynamic model has been posited to explain the growth mechanism of HCNT/HCNW.

An outline of this thesis is as follows: Chapter 2 is an introduction to CNTs in which the chirality, band structure, electronic, and thermal properties of CNTs are reviewed. In Chapter 3, we briefly introduce the working principles of SPS, how we prepare aligned MWCNT bulk samples, and how the inter-tube bonding affects the transport properties of MWCNT material. In Chapter 4, the effects of different SPS temperatures on transport properties of MWCNTs are examined. In Chapter 5, we present the electrical properties of boron doped CNTs prepared by the SPS method and the interesting possibility of realizing superconductivity in these systems. Chapter 6 is devoted to the synthesis method, characterization and thermodynamic growth model of HCNTs/HCNWs. We summarize the progress and address future work in Chapter 7.

CHAPTER TWO

BACKGROUND

2.1 Introduction

The discovery of CNTs can be traced back to 1952 by Radushkevich & Lukyanovich [8]. In 1972, Oberlin et al. published a transmission electron microscopy (TEM) image showing CNTs (diameter less than 10 nm) with hollow cores. But all these results didn't attract much attention from scientific community. In 1985, fullerenes were synthesized, for the first time, by laser ablation of a carbon target under an inert gas atmosphere by Kroto et al [9]. During the study of this new carbon molecular, speculation arose on the formation of different graphitic structures [10]. In 1991, Iijiima [2] found some needle-like tubular structures with diameters between 3-40 nm and lengths up to 1 μm when he investigated the byproduct of C_{60} production under high resolution TEM (HRTEM). These CNTs were MWCNTs, which consisted of 2-7 concentric graphene layers. Less than 2 years later, SWCNTs were synthesized using an arc-discharge method by Iijima el al. [11] and Bethune et al. [12] simultaneously in 1993. These results ignited great interest in CNTs. Extensive studies have been carried on since then. In this chapter, we review the unique structure of these CNTs and the remarkable properties due to its seamless cylindrical structure.

2.2 Chirality

In the simplest case, a single SWCNT can be viewed as rolling a graphene sheet into a seamless tube. But from geometric considerations, each different angle at which the graphene sheet is rolled gives rise to a different tube, with a different diameter etc. To characterize these different SWCNTs, chirality has been used to describe the orientation of hexagonal lattice of graphene sheet relative to the axis of the tube. An example is depicted in Figure 2.1, in which a SWCNT is formed by rolling the graphite sheet so that point A overlaps with point A′. The chirality of a tube can be determined by the direction of chiral vector $\mathbf{C_h}$ (AA′ in Fig. 2.1). Using $\mathbf{a_1}$ and $\mathbf{a_2}$ as the hexagonal basis vectors, the chiral vector $\mathbf{C_h}$ can be define as following [13]:

$$\mathbf{C_h} = n\mathbf{a_1} + m\mathbf{a_2} \tag{2.1}$$

where n and m both are integers.

The vector $\mathbf{C_h}$ is perpendicular to the axis of the tube. The magnitude of the vector $|\mathbf{C_h}|$ is the circumference of the tube. Then the diameter of the tube, d_t can be expressed in terms of (n,m),

$$d_t = \frac{\sqrt{3}a_{c-c}}{\pi}\sqrt{n^2 + m^2 + nm} \tag{2.2}$$

where a_{c-c} = 1.421 Å, is the carbon-carbon distance in graphite. The chiral angle θ_C is defined with respect to the (n,0) direction as

$$\theta_C = \tan^{-1}(\frac{\sqrt{3}m}{2n+m}) \tag{2.3}$$

Depending on the chiral angle, SWCNTs can be divided into three types: armchair ($\theta_C = 30^o$), zigzag ($\theta_C = 0^o$), and chiral nanotube ($0 < \theta_C < 30^o$) (Fig. 2.2). The diameter of SWCNT is in the range of 0.5-6 nm. The electrical properties of SWCNT are determined by the chirality of the tube.

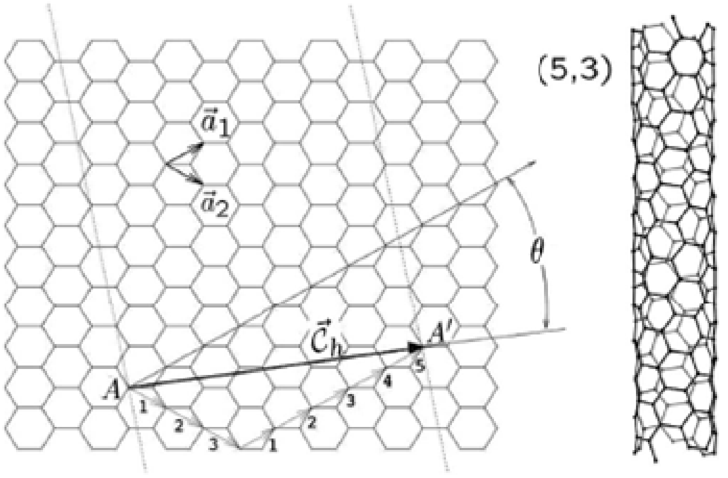

Figure 2.1. Illustration of the chiral vector and chiral angle on a 2-Dimensional graphene sheet. In the present example, a (5,3) nanotube is under construction and the resulting tube is illustrated on the right [14].

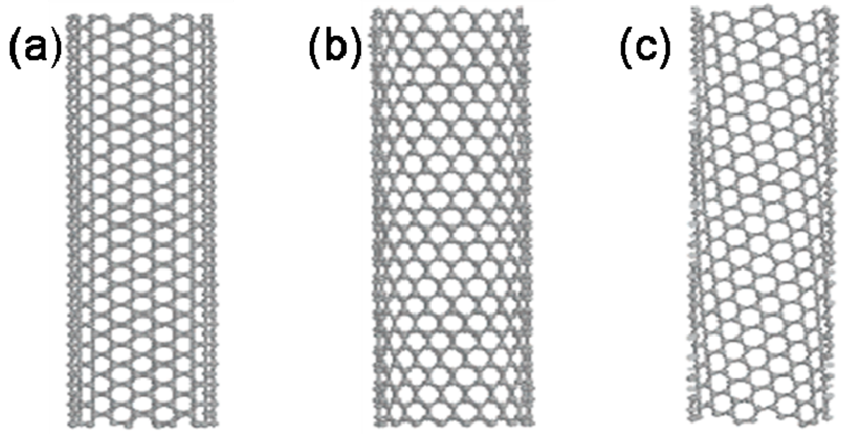

Figure 2.2. Illustration of (a) an arm chair SWCNT (8,8), (b) a zigzag SWCNT (8,0), and (c) a chiral SWCNT (10,2) [15].

The unit cell and its number of carbon atoms can be determined from the graphene lattice and chiral vector. The smallest graphene lattice vector **T** perpendicular to **C_h** defines the translational period t along the tube axis. The lattice vector **T** can be expressed in terms of the basis vectors $\mathbf{a_1}$ and $\mathbf{a_2}$ as $\mathbf{T}=t_1\mathbf{a_1}+t_2\mathbf{a_2}$. Using $\mathbf{C_h}\cdot\mathbf{T} = 0$, the expression for t_1 and t_2 is give by

$$t_1 = \frac{2m+n}{N_R}, \qquad t_2 = -\frac{2n+m}{N_R} \tag{2.4}$$

where N_R is the greatest common divisor of ($2m+n$) and ($2n+m$). Form 2.4, we can get the length of the translation vector t

$$t = |\mathbf{T}| = \sqrt{3}a\sqrt{n^2+nm+m^2}\,/\,N_R \tag{2.5}$$

Here, $a = \sqrt{3}a_{C-C}$ .From Eqn. 2.4 and 2.5, the nanotube unit cell is formed by a cylindrical surface with height t and diameter d_t. The number of carbon atoms per unit cell N_c can be expressed as a function of n and m:

$$N_C = 4(n^2+nm+m^2)/N_R \tag{2.6}$$

A MWCNT is comprised of several concentric SWCNTs (Fig.2.3). The interlayer spacing in a MWCNT is around 3.4 Å. There is no structural correlation between different concentric tubes in a MWCNT; in other words, the chirality of SWCNTs within a MWCNT is independent. So, a MWCNT can not be viewed as a stacked set of correlated SWNTs unlike the ABAB stacking of graphene in highly oriented pyrolytic graphite (HOPG). Compared with SWCNTs, the diameter of a MWCNT is pretty large, ranging from tens of nm to hundred of nm.

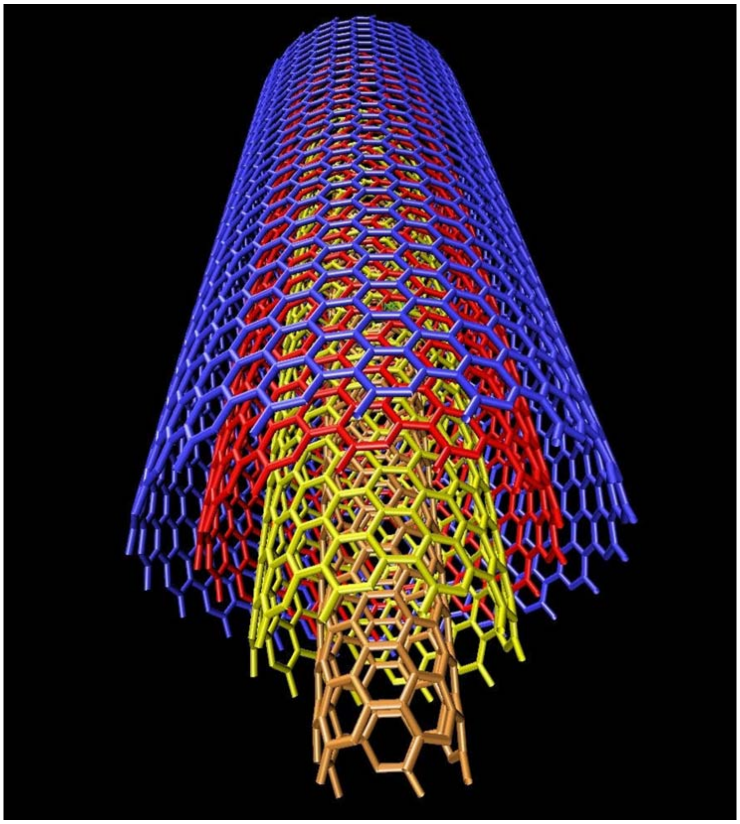

Figure 2.3 Illustration of a MWCNT [16].

2.3 Band structure of CNT

2.3.1 Isolated SWCNT

In its ground state, a carbon atom has an electron configuration of $1s^2 2s^2 sp^2$ (6 electrons in 3 orbitals). C-C bonding in graphene is sp^2 type and in this case, three of the four valence electrons form in-plane σ-bonds with adjacent lattice carbon atoms, and the fourth electron occupies a p_z orbital. The p_z states mix together forming delocalized electron states. These states are responsible for the electrical conductivity of graphene.

Considering only one orbital and neglecting the overlap along the c axis (perpendicular to the hexagonal planr of graphene), the general dispersion relation derived through a Slater-Koster tight binding scheme is [17]:

$$E_{graphene}(k_x,k_y) = \pm\gamma_0\left[1+4\cos\left(\frac{\sqrt{3}k_x a}{2}\right)\cos\left(\frac{k_y a}{2}\right)+4\cos^2\left(\frac{k_y a}{2}\right)\right]^{1/2} \quad (2.7)$$

where the positive and negative signs correspond to the conduction band and valence band, respectively, the *k*'s are wavevectors and γ_0 ~2.9 eV is the value of overlap integral. A plot of Eqn. 2.7 is illustrated in Fig. 2.4 [17], with the high symmetry points labeled. We can see that along some directions, the valence band and conduction band come together at certain points, for example, the *k* point, thus graphene is metallic; but along other directions, graphene is a semiconductor.

As a quasi one –dimensional material, the electrical structure of SWCNT can be closely approximated from the electrical structure of graphene, with periodic boundary conditions around the circumference of carbon nanotube [3]. A detail derivation of energy dispersion relation of SWCNT using tight-binding approximation is presented in Ref. 9, we only outline some major points here. Due to the quasi one dimensional (1-D) geometry of SWCNT, the electron wavevector transporting along the radial direction is confined, in other words, the electron wave number perpendicular to the direction of tube axis is quantized. In order to get the *ε*-*k* relation of SWCNTs, a periodic boundary condition can be imposed on Eqn. 2.4, as following:

$$\mathbf{C_h}\cdot\mathbf{k} = 2\pi v \quad (2.8)$$

where $\mathbf{C_h}$ is chiral vector, and v is integer. Eliminating k_x or k_y by using Eqn. 2.8, the 1-D energy bands for general chiral structures can be obtained. The density of states for two zigzag SWCNTs with $(n,m) = (10,0)$ and $(9,0)$, respectively, are depicted in Fig. 2.5 in unites of states per unit cell of two dimensional 2-D graphite. The characteristic singularities 1-D energy bands appear at the band edge of each energy band.

In Fig. 2.5a, there is an energy gap at the Fermi Level (E=0), while a finite density of states can be found in Fig. 2.5b. From Eqn 2.8, we know that the wavevector is quantized along circumference direction, which results in several lines of allowed k values in the graphene k space (discrete points in k_x/k_y, but no restriction in k_z direction for infinite tubes). It is noted above that the valence and conduction bands for graphene are degenerate at the K point. Therefore, nanotube with a set of wavevector which include the K point should be metallic, otherwise it is semiconductor. For the (9,0) tube there are nine lines of allowed wavevectors, as shown in Fig. 2.6 and one of lines passed through a K point.

The SWCNT is metallic when:

$$2n + m = 3q \tag{2.9}$$

where q is an integer. Thus, one-third of SWCNT are metallic and two-thirds are semiconducting. Close to the Fermi energy, the energy-momentum relation is nearly linear, in contrast with the quadratic energy-momentum relation followed by electrons at band edges in conventional semiconductors. This linear relation will explain the extremely good conductivity in the graphene and bears much importance in the Luttinger-liquid (LL) behavior for low-energy excitations in nanotubes. The Fermi velocity can be expressed as

$$v_F = \sqrt{3} a \gamma_0 / 2\hbar = \frac{3}{2} a_{C-C} \gamma_0 / \hbar \tag{2.10}$$

which is typically given by $v_r \approx 8 \times 10^5$ m s^{-1}, for γ_0 = 2.9 eV.

For a semiconducting nanotube, the band gap depends on the tube diameter and chirality, which is generally expressed by [13]

$$E_g = \frac{|\gamma_0| a_{C-C}}{2 d_t} \tag{2.11}$$

The effective mass of the charge carrier can also be deduced from the *ε-k* dispersion relation as follows [14]:

$$m^* = 2\pi\hbar / 3 |C_h| v_F \tag{2.12}$$

The effective mass is inversely proportional to the nanotube diameter and tends to zero as the diameter tends to infinity.

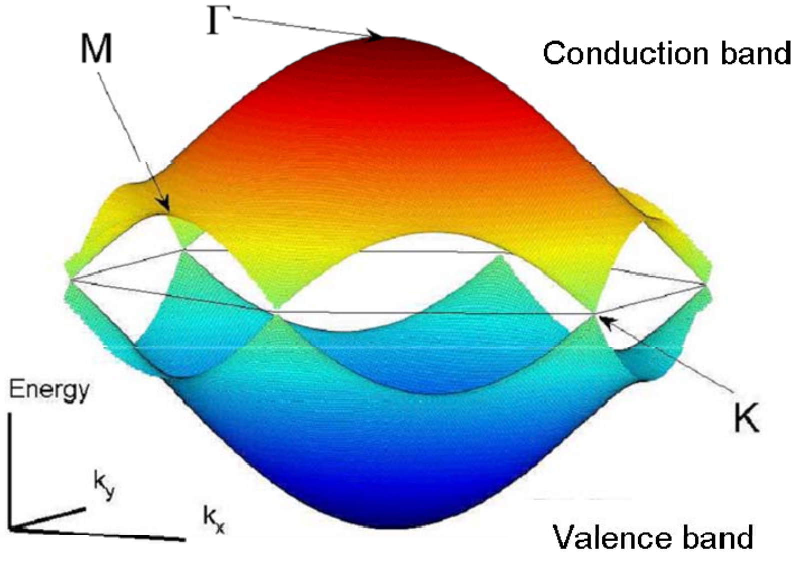

Figure 2.4 The energy dispersion relation of graphene, from the nearest-neighbour tight bonding calculation, using Slater-Koster approximation. Γ, M, and K are high symmetry points, where K-points lie on the plane of E=0 (the Fermi energy level) [17].

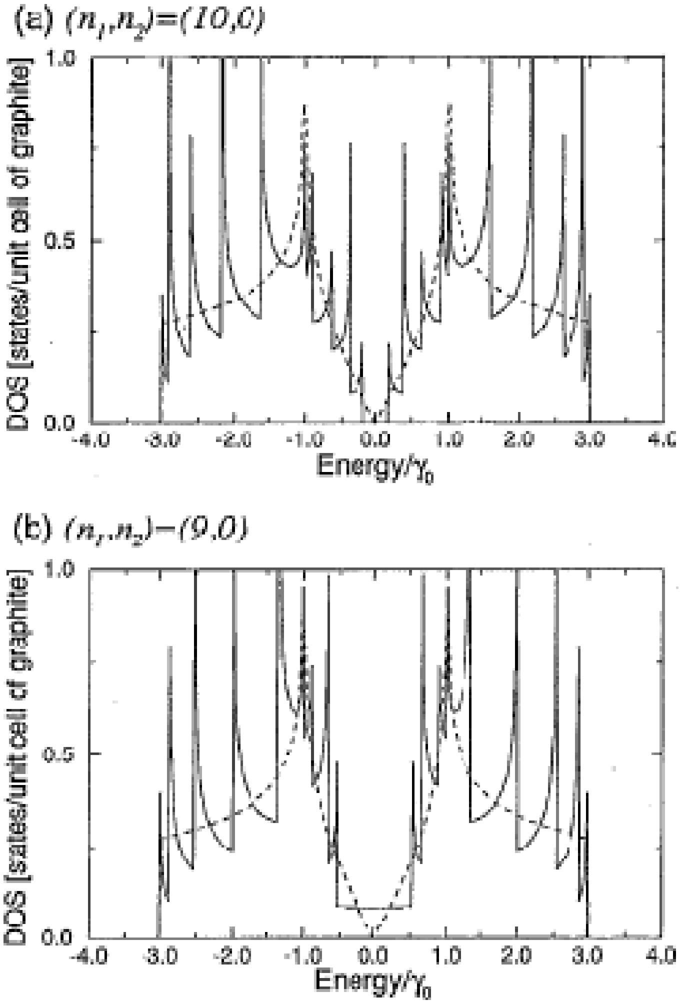

Figure 2.5 Electronic density of states for two (*n*,*m*) zigzag nanotubes: (a) (10,0) and (b) (9,0) [18].

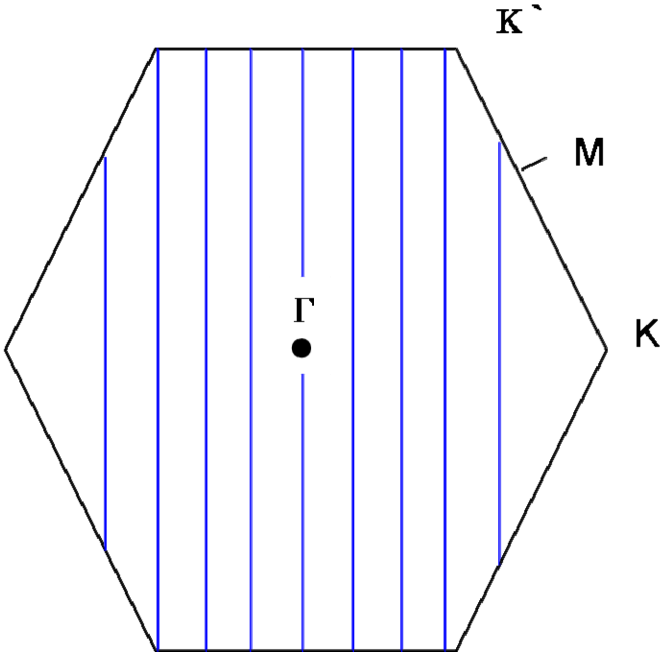

Figure 2.6 Illustration of allowed *k* values in the Brillouin zone (BZ) for a (9,0) zigzag nanotube.

In the previous discussion, we neglected the curvature of the nanotube. As a matter of a fact, a cylindrical topology will induce several effects different from those of a planar graphene sheet [14], such as the basis vectors have different length; planar symmetry is broken so that the π and σ states form hybrid orbitals that exhibit partial sp^2 and sp^3 character and so on. When accounting for curvature effects, the only zero-band-gap tubes are the (n,m) armchair nanotubes. The (n,m) tubes with $n - m = 3l$, are tiny-gap semiconductors. Also, for very small tubes, the curvature is so strong that rehybridization among the π and σ states dominates and the previous conclusions may fail completely.

2.3.2 SWCNT bundle and MWCNT

Due to the high aspect ratio and strong van der Waals force between tubes, SWCNT always exist in bundles of 10-100 nanotubes, closely packed into a triangular lattice during the synthesis. Strong tube-tube interaction will alter the properties of the constituent CNTs. Delaney et al. [4] revealed that the broken symmetry of the (10,10) tubes caused by interactions between tubes in a bundle induces a pseudogap of about 0.1 eV at the Fermi energy through first-principles calculations. This pseudogap modifies many fundamental electronic properties of the CNT, for example, the temperature dependence of the electrical conductivity and the infrared absorption spectrum. The existence of both electron and hole charge carriers will lead to qualitatively different thermoelectric power (TEP) and Hall-effect behaviors than those expected for a normal metal.

In the limit of an isolated (10,10) tube, the two linear bands (π bonding and π antibonding) crossing at the Fermi level belong to different irreducible representations with respect to the tube symmetry planes, so that crossing is allowed (Fig. 2.7). However, when the distances between tubes in a bundle are small enough, each tube can feel the potential due to all the other nanotubes. As a result of this perturbation, the Hamiltonian at any point k where the two bands used to cross becomes

$$H_k = \begin{pmatrix} \varepsilon_0 + \delta_{11} & \delta_{12} \\ \delta_{12} & \varepsilon_0 + \delta_{22} \end{pmatrix} \tag{2.13}$$

where ε_0 is the unperturbed energy. The diagonal matrix elements δ_{11} and δ_{22} merely act to shift the energy and location in k-space of the band crossing. It is the off-diagonal elements that cause quantum-mechanical level repulsion and therefore open a gap as shown schematically in Fig. 2.7b. These results have been experimentally proved by M. Ouyang, et al. [5] using low-temperature scanning tunneling spectroscopy. They observed an energy gap of 100 meV at 5 K in vacuum for armchair SWCNT bundles, which is absent in isolated armchair nanotubes. The energy gap depends inversely on the nanotube radius. For some kinds of armchair nanotubes, for example, (6.6) nanotubes arranged in a triangular lattice, which preserve the D_{6h} symmetry of the hexagonal packing, the off-diagonal matrix elements may still be zero and pseudogap due to inter-tube interaction is not observed [19]. But Reich, et al. showed that small rotation of (6,6) tubes will break the symmetry of the (6,6) bundle, and open up this expected gap at Fermi energy [20].

As stated before, MWCNTs can be considered as several SWCNTs with different diameters arranged in concentric cylinders, like a Russian doll. Interaction between the concentric shells in a MWCNT may also change the electronic properties of the nanotube. Lambin *et al.* [21] using the a tight-binding technique calculated the electronic structure of (5,5)@(10,10) double-wall carbon nanotubes (DWCNT). They found that the weak inter-tube interaction periodically opens and closes four pseudogaps near E_F due to symmetry lowering during the low-frequency liberational motion about and vibrational motion normal to the double-tube axis. In the absence of the inter-tube interaction, the band structure of each tube is characterized by two crossing linear bands near E_F , as shown in Fig. 2.8a. Switching on the inter-tube interaction in the (5,5)@(10,10) double-wall tube removes the near degeneracy of the bands near E_F as well. In the most stable orientation, the double-wall system is still characterized by the D_{10h} symmetry of the inner tube. The four bands cross with a very small change in slope (Fig. 2.8b). While the same argument also applies to the least-stable configuration, a markedly different behavior is obtained at any other tube orientation that lowers the symmetry, giving rise to four band crossings (Fig. 2.8 (c)).

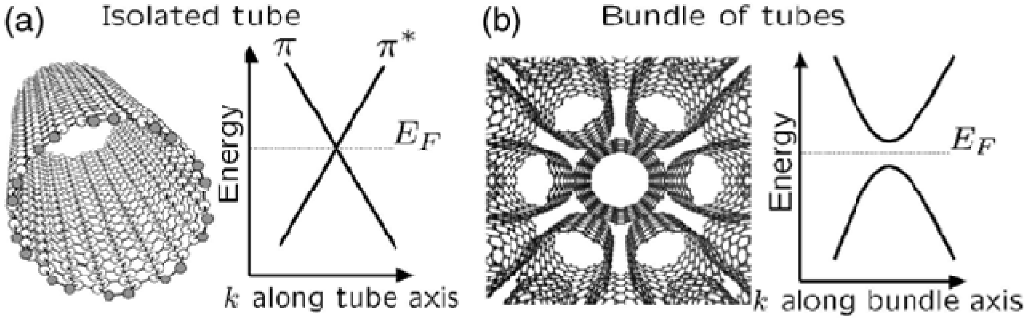

Figure. 2.7 Band crossing and band repulsion. Schematic diagram of the crossing of the two linear bands for an isolated (10, 10) carbon nanotube. One band has π-bonding character and the other has π-antibonding (π^*) character. E_F is the Fermi energy and k is the wave vector. (b) Repulsion of the bands due to breaking of mirror symmetry [4].

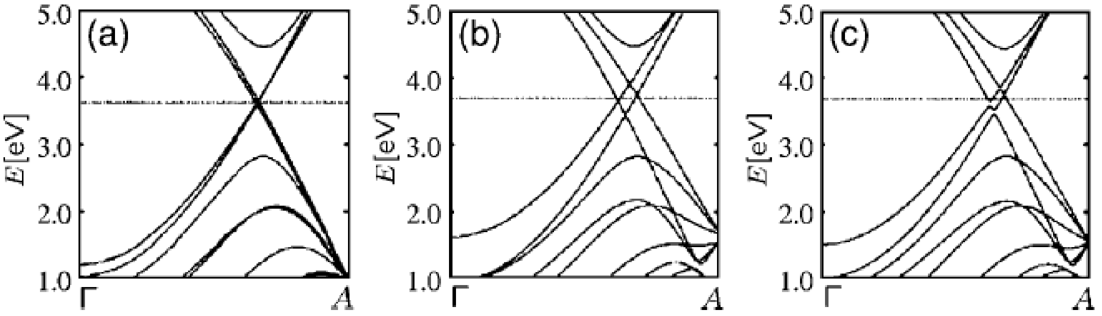

Figure 2.8 Band structures of the same double-wall tube for different relative orientations. Near-degenerate bands with no gap characterize the (5,5)@(10,10) DWCNT without inter-tube interaction (a). In the presence of inter-tube interaction, depending on the mutual tube orientation, the (5,5)@(10,10) system may show a zero gap (b) in the most symmetric (point group symmetry D_{10h}) or four pesudogaps (c) in a less symmetric and stable configuration (point group symmetry C_5) [22].

2.3.3 Defects in CNTs

All the theoretical works in Section 2.1.1 and 2.1.2 are based on “perfect” carbon nanotubes. However, during the CNT synthesis some defects are introduced with or without intention, such as pentagons, heptagons, vacancies, or dopants. These defects not only modify the topology [6-7, 23] but also, at least locally influence the electronic properties of these nano-systems [6]. The introduction of defects in the carbon networks is thus an interesting way to tailor its intrinsic properties. Systemic theoretical work about defects in carbon nanotube has been done [6]. Here we just outline some major results which are related to this thesis, especially about pentagon-heptagon (PH) membered rings and dopant in CNT. Some recent experimental works are also introduced to provide more insights into the effects of defects on the physical properties of CNTs.

F. Banhart et al. show that carbon atoms can be continually removed under uniform irradiation conditions of electrons in an electron microscope [24-26]. Vacancies in CNT due to the loss of carbon atoms are energy unstable because of dangling bonds associated with these defects and could further cluster into bigger holes in the structure. By mending these holes through atomic rearrangements, the surface of the original nanotube reconstructs into a highly defective monoatomic layer cylinder. Some non-hexagonal rings such as squares, pentagons, heptagons, octagons, nonagons, and decagons were observed at certain stages of the surface reconstruction. However, high-membered rings are found to be generically unstable and would anneal away via the Stone-Wales mechanism at a certain temperature [27]. Thus, the CNT structure are mainly constituted of five-, six-, and seven-membered rings [6].

Other theoretical works have proposed that carbon nanotube intermolecular junctions can be formed by interposing one or multiple topologic PH defects in the hexagonal structure between two nanotubes segments with different helicity [28-31]. Fig 2.9 shows such a connection using a single PH pair, which connects a (8,0) nanotube (semiconductor) and a (7,1) nanotube (metal). This kind of structure can thus be proposed as the basis of a nanodiode for nanoelectronics.

Some groups have reported the coalescence of SWCNT bundles under electron irradiation or at high temperatures [25, 32-33]. The merging process is investigated at the atomic level using molecular dynamics simulations. The calculations show that the vacancies and dangling bonds on the surface of CNTs introduce coalescence via a zipper-like mechanism, imposing a continuous reorganization of atoms on an individual tube lattice along adjacent tubes. Similar idea have been applied to form stable molecular junctions of various geometries (“X”, “Y”, and “T”) by using electron beam welding at elevated temperatures. Theoretically, to create a smooth topology for the CNT junctions, several PH member rings have to be introduced at the points where CNTs overlap. Figure 2.10 [6] depicts an ideal “X” nanotube connection, where a (5,5) armchair nanotube intersects an (11,0) zigzag tube. Six heptagons have been introduced at each crossing point to create a smooth surface. Fig. 2.10b shows the calculated local densities of states (LDOS) at the areas labeled with (1), (2) and (3) in Fig. 2.10a. There are some important features for the LDOS at the junction. One is the presence of localized donor states in the conduction band (as indicated by arrows), which is caused by the presence of heptagons. There is an additional small peak close to the Fermi energy on the valence band, which is attributed to the high curvature of the graphitic system. The van Hove singularities present in the LDOS of the two tubes are drastically less pronounced in the junction region, thus illustrating a clear loss of the one-dimensional character at this site.

On the other hand, using dopants (such as boron, nitrogen, etc.) to substitute for carbon atoms in CNTs has been explored in order to tailor the electrical properties of nanotubes. Basically, boron doping can be carried out either during the synthesis of CNT by using a boron compound as the precursor [34], or through a substitution reaction by high temperature treatment of a boron compound/CNT mixture [35]. Nitrogen doped

CNTs can be synthesized by pyrolyzing the ferrocene/melamine mixtures at high temperature [36]. Raman spectra [34], Nuclear Magnetic Resonance (NMR) [37], scanning tunneling spectroscopy [38], are among the experimental tools that have been exploited to identify the existence of boron/nitrogen in carbon atom networks.

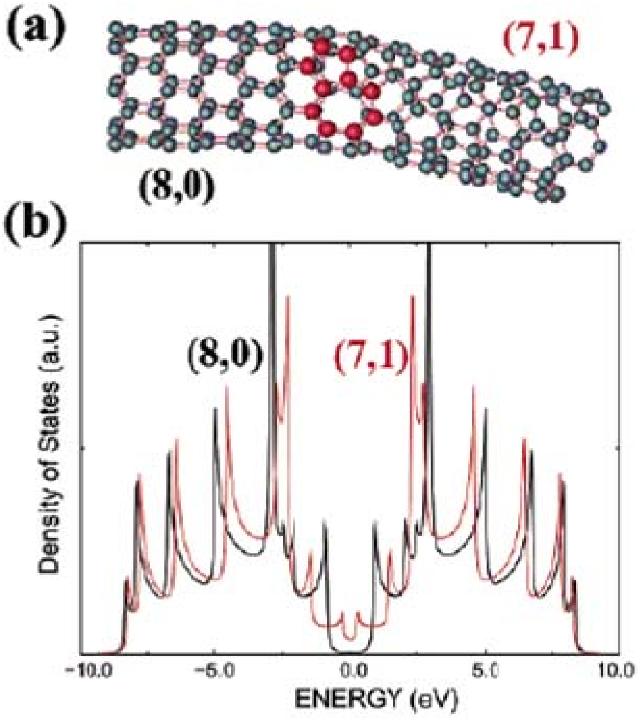

Figure 2.9 (a) Atomic structure of an (8,0)-(7,1) intra-molecular carbon junction. The large red balls denote the atoms forming the pentagon-heptagon pair. (b) the electron density of states related to the two perfect (8,0) and (7,1) nanotubes are also illustrated in black and red, respectively [6].

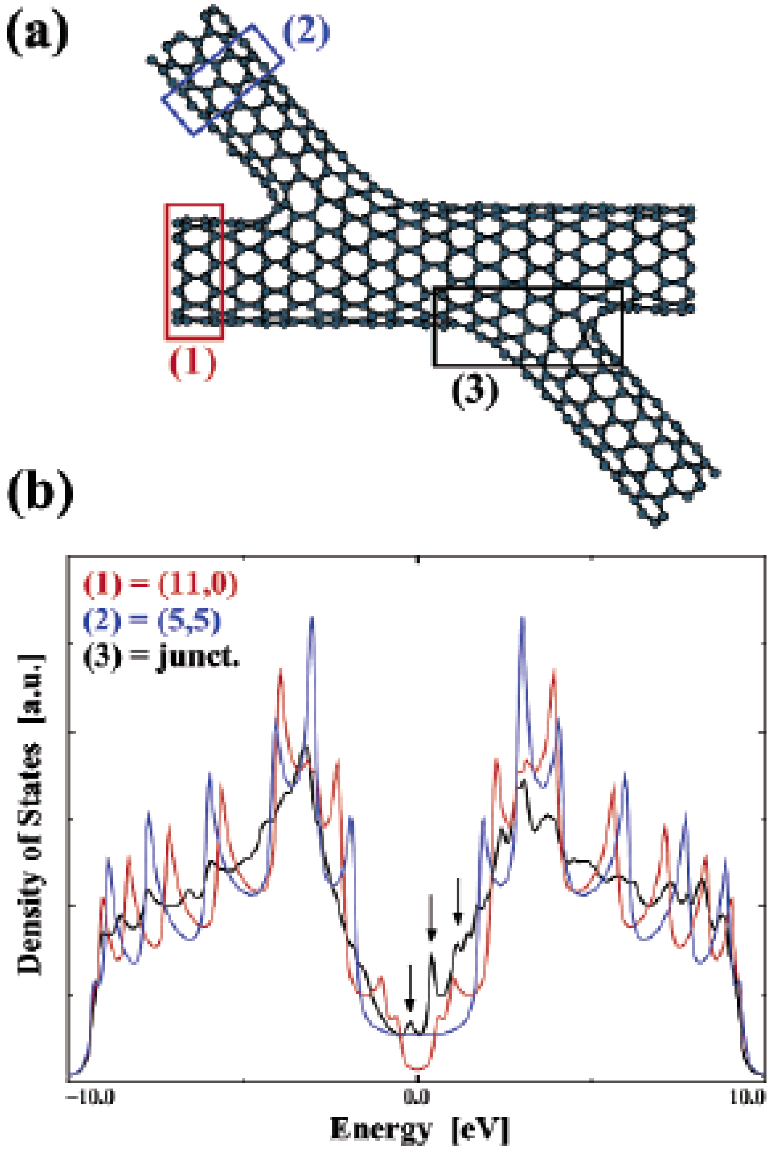

Figure 2.10 Electronic properties of an ideal X-junction (a), created by intersecting a (5,5) tube with an (11,0) tube. (b) One-dimensional electronic densities of states of a semiconducting (11,0) nanotube (red curve), a metallic (5,5) nanotube (blue curve), and an average over the intersecting region of the molecular junction (black curve). The

Fermi level is positioned at zero energy. Localized states due to the presence of defects are indicated by arrows [6].

First principle calculations show that change in the LDOS of boron doped tubes [38], as determined from tunneling microscopy, must be interpreted in terms of nano-domains of BC_3 islands and not as isolated substitional species, However, pyridine-like N structures are responsible for the metallic behavior and the strong electron donor states observed near the Fermi level in the LDOS of nitrogen-doped tubes [36]. The LDOS also exhibit strongly localized acceptor states (p-doping) or donor states (n-doping) near the Fermi level, which agree very well with the experimental results [39]. It is note worthy to point out that N. Murata et al. [37] reported a Meissner effect in a boron doped SWCNT thin film around 12 K. This result has attracted a worldwide interest in doped CNTs.

2. 4 Transport properties of CNT

2. 4.1 Electrical properties

Theoretical works have predicted that individual SWCNT can be metallic or semiconducting depending on the chirality of the tube. This prediction was experimentally confirmed by few groups using STM [40-41], which resolves simultaneously both atomic structure and the electronic density of states. Both metallic and semiconducting SWCNT were observed and the electronic properties indeed depended sensitively on the chirality. The first electrical transport measurement on an individual SWCNT was reported by S. J. Tans, et al. in 1997 [42]. In their measurements, the SWCNT acted as genuine quantum wires and electrical conduction seems to occur through well separated, discrete electron states that are quantum-mechanically coherent over long distances. Coulomb charging behavior was observed due to high contact resistance. M. Bockrath et al. [43] observed a power law dependence of conductance (differential conductance) on temperature (bias voltages), which provides strong evidence that the electrons in metallic carbon nanotubes constitute a Luttinger liquid. On the other hand, the electrical properties of individual MCWNTs have been shown to vary strongly from tube to tube and to be characterized by disorder and localization [44-45]. Both metallic and non metallic behaviors were observed in MWCNTs, which suggest that differences in geometry also play a profound part in determining their electronic behaviour. A pronounced Aharonov-Bohm resistance oscillation as a function of magnetic flux was observed by A. Bachtold et al. [46]. Their results clearly demonstrate that at low temperature quantum interference phenomena dominate the magnetoresistance of MWCNT. C. T. White et al. [47] has shown, using the tight-binding model, that electron transport through CNT is ballistic with localization lengths of 10 μm or more. In addition, ballistic transportation in 4 μm range in MWCNTs was also reported by S. Frank, et al.[48]. In the experiment, a single MWCNT attached on a STM tip was lowered into a liquid metal to establish a gentle electrical contact. Two units of quantum conductance $2G_0 =4 e^2/h$ for a SWCNT with length ~200 nm were also reported by Kong el al. [49], corresponding to the maximum conductance limit for ballistic transport in two channels of a nanotube (π and π^* channels).

The current is carried on the surface of the tube, in the same manner as current flow over metallic wires. For MWCNTs, this current is carried by the outermost tube layers, and little current flows between layers, giving multi-walled tubes similar resistances to SWCNTs. In defect-free CNTs, as a result of the strong covalent bonding and the lack of scattering due to ballistic electron transport (minimizing joule heating), the current carrying capacity can exceed 10 μ A/nm^2, a factor of one thousand greater than standard metallic wires [50].

CNT as a 1-D molecular conductor, face some obstacles that prevent them from superconducting, such as (1) non-Fermi (Luttinger) liquid behavior at low temperature due to electron-electron interactions [43], (2) a Peierls transition (charge-density wave), and (3) a small density of states, which becomes significant when the Fermi level is not aligned with van Hove singularities [43]. However, A. Y. Kasumov et al. [51] showed that a single SWCNT or SWCNT bundle becomes superconducting with a transition temperature $T_C = 1.1\ K$ when the resistance of the nanotube-electrode junction is sufficiently low. In their experiments, superconducting bilayer electrodes (Re/Au or Ta/Au) were used, which create superconducting junctions with CNTs and give rise to proximity-induced superconductivity. Two years later, Kasumove group reported superconductivity in ropes of SWCNTs below 0.55 K [52]. This time they attributed the superconductivity to the intrinsic properties of SWCNTs since the Al_2O_3/Pt/Au contacts they used in their experiments were in normal state in that temperature range. Z. K . Tang et al., also reported that 0.4 nm diameter SWCNTs become superconducting at 15 K [53-54]. On the other hand, superconductivity is also found in MWCNTs with T_C ranging from 12 K [55]to 23 K [56]. N. Murata, et al. showed for the first time evidence of superconductivity of boron doped SWCNTs with a $T_c \sim 12$ K [37]. CNTs as a new class of superconductors are attracting great interest in the scientific community.

2.4.2 Thermal properties

In addition to electronic properties, CNTs are also of great interest for their thermal properties. Because of their small size, quantum effects are important, and the low-temperature specific heat and thermal conductivity show direct evidence of 1-D quantization of the phonon bandstructure.

The specific heat C(T) of a material is a sensitive probe of the low-energy excitations. In 3-D graphite, 2-D graphene, and nanotubes, phonons are the dominant excitations, and the phonon specific heat C_{ph} dominates C(T) at most temperatures. C_{ph} can be obtained by integrating the phonon density of states $\rho(\omega)$ together with a temperature-dependent convolution factor accounting for the temperature-dependent occupation of each phonon state [57]

$$C_{ph} = \int k_B \left(\frac{\hbar \omega}{k_B T} \right)^2 \frac{e^{\frac{\hbar \omega}{k_B T}} \rho(\omega) d\omega}{\left(e^{\frac{\hbar \omega}{k_B T}} - 1 \right)^2} \tag{2.14}$$

The specific heat of CNTs can be calculated from the phonon density of states using above equation. When a graphene sheet is “rolled” into a nanotube, the 2-D bandstructure folds into a large number of 1-D subbands. A direct result of this folding is that the nanotube density of states has a number of sharp peaks as a result of 1-D van

Hove singularities, which are absent in graphene and graphite [58]. In spite of the presence of these singularities, the overall density of states is similar at high energies, so that the high temperature specific heat should be roughly equal as well. At low energies, the geometry of the nanotube causes the phonon structure to substantially differ from that of the parent graphene sheet.

At the lowest temperatures, the isolated nanotube *C(T)* is linear in *T*. The contribution of each acoustic mode to *C(T)* is can be analytically expressed [59]:

$$C_{ph} = \frac{\pi k_B T}{\hbar v \rho_m} \tag{2.15}$$

where ρ_m is the linear mass density. At high temperature, the slope of *C(T)* increases, as the optical subbands begin to contribute. The linear behavior at low T is a direct signature of the 1-D quantized nature of the nanotube phonon bandstructure. Interlayer coupling (in graphite) and inter-tube coupling (in strongly coupled bundles) depresses the *C(T)* at low-*T*. In real samples, the temperature at which the measured *C(T)* diverges from the single-tube curve provides measure of the actual inter-tube coupling. Ref. [59] also shown that the phonon contribution will dominate the electron contribution.

In general, the thermal conductivity can also be expressed as: $\kappa = Cvl/3$, where l is the phonon mean free path. Berber et al. [60] have calculated the phonon κ of isolated nanotubes. Figure 2.11 shows the results of theoretical calculations of the phonon κ of an isolated SWCNT. $\kappa_{ph}(T)$ peaks near 100 K, and then decreases with increasing T. The value of κ at the peak (37 kW/(m-K)) is comparable to the highest κ ever measured (41 kW/(m-K) for an isotropically pure diamond sample at 104 K). Even at room temperature, the κ is quite high (6.6 kW/(m-K)), exceeding the reported room temperature κ of isotropically pure diamond by almost a factor of 2. Kim et al. [61] directly measured the κ of individual MCWNTs using a micro fabricated structure (inset to Fig. 2.12). The data in Fig. 2.12 show the measured κ of one MWCWNT. $\kappa(T)$ increases as T^2 up to 100 K, peaks near 300 K, and decreases above this T. The quadratic T dependence is exactly what would be expected for large-diameter nanotubes that essentially act as 2-D sheets. The room-temperature value of $\kappa(T)$ for an individual MWCNT is over 3000 W/(m-K). C. Yu et al. [62], also measured κ of an individual SWCNT, which showed a ballistic thermal transportation. The κ they measured is of the same order of magnitude as that reported in Ref. [61]. However, with increasing dimensionality the magnitude of κ decreased dramatically: for 2-D CNT film/bucky paper, the room temperature value of κ is in the range of 20-300 W/(m-K) [63]; For 3-D CNT bulk material, the room temperature κ is between 3-15 W/(m-K) [64-65].

In a CNT network, the thermal conductivity is likely to be limited by tube-tube junctions, tube-tube interaction and defects in the nanotubes. Because of this, R. S. Prasher et al. also proposed using a packed bed of 3-D random networks of CNTs as heat insulators [66].

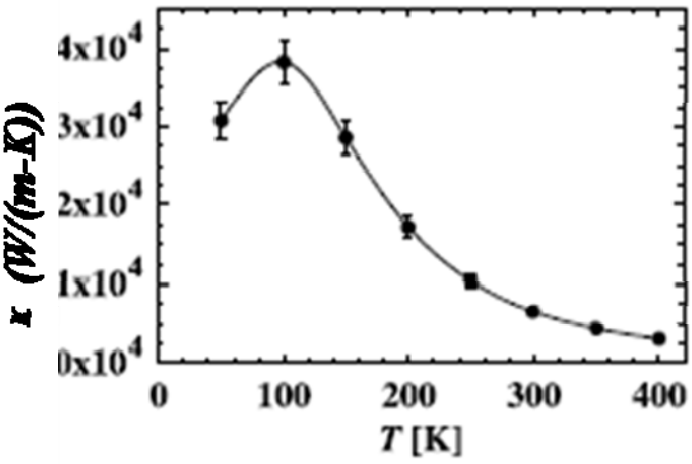

Figure 2.11 Calculated *κ* of an isolated SWCNT, as a function of *T* [60].

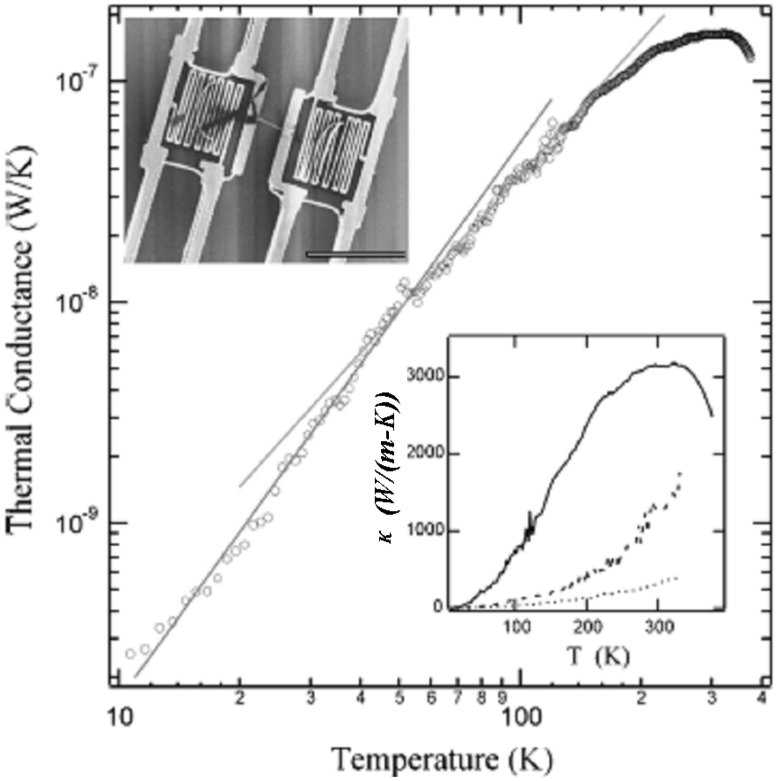

Figure 2.12 The thermal conductance of an individual MWCNT of a diameter 14 nm. The solid lines represent linear fits of the data in a logarithmic scale at different temperature ranges. The slopes of the line fits are 2.50 and 2.01, respectively. Lower inset: Solid line represents κ(T) of an individual MWCNT (d = 14 nm). Broken and dotted lines represent small (d = 80 nm) and large bundles (d = 200 nm) of MWCNTs, respectively. Upper inset: SEM image of the suspended islands with the individual MWCNT. The scale bar represents 10 mm [61].

2.4.3 Thermoelectric Power

The application of a temperature gradient to a metal leads to the diffusion of charge carriers from the warm to the cold end of the samples. The TEP (S) measures the charge build up across the sample. It is given by $S = lim_{\Delta T \to 0} \Delta V / \Delta T$, where ΔV and ΔT are the potential and temperature differences across the sample, respectively. S due to diffusion S_{diff} can be calculated from the standard set of transport coefficients. The transport coefficients can in turn be derived from the Boltzmann equation for the electron distribution function. A general argument leads to the Mott expression for S due to diffusion [67]

$$S_{diff} = \frac{-\pi^2}{3} \frac{k_B^2 T}{|e|} \left(\frac{\partial \ln \sigma}{\partial E} \right)_{E_F} \qquad 2.16$$

where E is the energy, σ the electrical conductivity, and E_F the Fermi energy. Because S is related to the energy derivative of the σ probed at E_F, it is sensitive to the curvature of the bands at the E_F level. *S* yields directly the sign of the charge carriers within a metallic conductor, at least for single band materials. For a semiconductor, *S* probes the sign of the dominant carriers as well as the energy gap magnitude. Besides the electronic band structure, *S* of a material also yields important information related to EPC parameters, and the relaxation rate of the system.

Because *S* is a zero current transport coefficient, it can probe the intrinsic conduction of individual nanotubes while being less influenced by randomly entangled morphologies and imperfections of the measured mats as compared to standard conductivity measurements [68]. For example, intrinsic metallic properties were well demonstrated with *S* of conducting polymer films exhibiting randomly entangled fibrillar morphologies. However, in these systems the electrical conductivity always showed a semiconducting temperature dependence due to interfibrillar junction resistance [69]. In order to further understand electrical transport properties of, to answer some of the questions raised by the dc resistivity measurements, and to attempt to provide experimental confirmation of band structure calculations for CNTs, *S* of CNTs were measured by several groups [61-62, 70-75]. A positive and roughly linear *S(T)* above ~ 100 K has been observed for a single SWCNT [62], single MWCNT [61], mats of SWCNTs [70] and mats of MWCNTs [75]. The fact that *S(T)* is linear suggests that conduction through metallic tubes dominates *S* at these temperatures. Due to the electron-hole symmetry [76], *S* of metallic tubes (such as (10,10) tubes) are predicted to near zero. But relatively large magnitude of *S* (above 60 μ V/K at room temperature) was observed in experiments [61-62, 70], and was attributed to the electron-hole symmetry breaking due to the tube-tube interaction or inter-wall coupling in MWCNTs. The symmetry breaking could cause a contribution to *S* from both drift and phonon-drag effects. The large positive value of TEP also suggests that electron transport was not ballistic in these CNT samples. The interaction between tubes or inter-wall coupling tends to break down the unconventional Luttinger liquid picture and draw the electrons back to the conventional Fermi liquid. The scattering processes of the electrons by defects (such as the intrinsic stacking faults between tubes or adjacent walls) should also influence the transport properties, leading to a diffusive rather than a ballistic electron motion.

For SWCNT mats and bundles, several experimental results showed nonlinear *S(T)* below ~100 K. The origin of this nonlinearity has been the subject of much debate. Several effects that could lead to such behavior have been discussed in literature. These include parallel transport through semiconducting tubes in the mats [70], one dimensional Kondo effect due to magnetic catalytic impurities in the mats [71], strongly localized states due to the dopants in CNTs [39], and the phonon drag effect [77-79]. The real origin of this nonlinear behavior should depend on the sample preparation.

S of CNTs is extremely sensitive to gas exposure history. K. Bradley et al. [72], have shown that when SWCNTs are exposed to air or oxygen they always have a positive *S*; however, at fixed *T*, *S* crossed zero and became progressively more negative as the SWCNTs were stripped of oxygen. The oxygen molecule breaks the symmetry of the tubes which causes the valence band to split and produce states at the E_F. This behavior has also been observed in MWCNTs [75, 80]. Figure 2.13 shows that as-prepared MWCNT mats exhibit *n*-type characteristics when vacuum annealed and upon exposure to room air and light, slowly loses its *n*-type characterisitcs and exhibits *p*-type characteristics.

In conclusion, TEP is an extremely sensitive and incisive transport coefficient. It is independent of the junctions between tubes and be a valuable tool to elucidate the intrinsic electrical transport properties of CNTs.

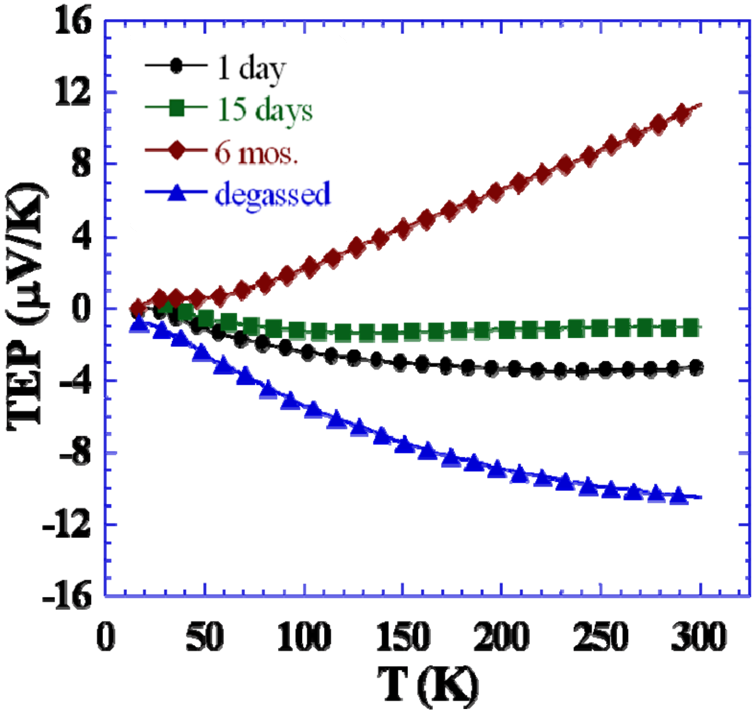

Figure 2.13: The temperature-dependent TEP data of as-prepared MWCNT mats. The samples were exposed to room air and *S* data was collected over a period of six months. [75]

2.5 Conclusion

In this section, we reviewed the electrical and thermal properties of CNTs from both theoretical and experimental stand points. A single SWCNT with no defects can be metallic or semiconducting, depending on its chirality. Single MWCNT with no defect, are metallic or semiconducting with extremely small band gaps. As a quasi 1-D conductor, the electron-electron interaction in CNTs makes the conventional Fermi liquid picture not suitable. For a single CNT, it is clear that the electrons are highly correlated to form a 1-D Luttingr liquid, and its transport is via a ballistic process. Quantum phenomena have been observed in this 1-D conductor. A single CNT also shows very high thermal conductivity.

However, as we discussed in the section 2.4.3, CNTs are very sensitive to the environment. Tube-tube interactions or interlayer interactions, gas molecules around the CNT, defects and dopants in the carbon network, all these factors will affect the electrical/thermal properties. So, one often finds different results reported by different groups. Some conclusions are still arguable. Finding an efficient way to control the tube-tube interaction, defects and a systematic study of the effect of tube-tube interaction and defects/dopants in the CNT on electrical/thermal properties of CNT is needed. In chapter 3-4, we discuss the use of SPS process to form coherent bonding between tubes. Electrical and thermal transport measurements were done to reveal how electrons/phonons are affected by strong tube-tube interaction. In Chapter 5, we dope CNT with boron during the SPS process, changing the electrical properties of the CNTs dramatically. In Chapter 6, we show that by periodically introducing PH pairs in carbon network, the shape of a CNT transforms from straight to the helical form.

CHAPTER THREE

ALIGNED MWCNT BULK SAMPLE FABRICATED BY SPS SINTERING

3.1 Introduction

Modifying the inter-tube bonding from the van der Waals in a SWCNT bundle or a MWCNT to a robust inter-tubular bonding is non-trivial, since the topologically complicated arrangement of sp^2 bonds in the inter-tube bonding is not energetically favored. High energy processes such as electron irradiation [25, 81], thermal treatment [33], high electrical current [82-83] and plasma etching [84] have been shown to promote inter-tubular bonding. Recently, the SPS technique has been shown to be effective in altering the sp^2 bonding in CNTs [85-86]. SPS is a high energy, low voltage, pulsed plasma discharge in a controlled environment that can generate highly localized Joule heating (up to a few thousand degrees Celsius) in few minutes. The current density in the SPS process (calculated by dividing the current by the cross-sectional area of the graphite die in Fig. 1(a)) is typically on the order of 10^2 A/cm^2 and is highly concentrated at the inter-granular contact or interface, and can lead to the transformation of sp^2 bonded MWCNTs to sp^3 bonded micro-diamonds [85] or graphitization and formation of crystalline-amorphous carbon hetero-junctions in amorphous carbon fibers [86]. In SPS-densified samples comprised of randomly oriented MWCNTs, Zhang et al. [64] have reported the formation of graphitic micro-phases, and the transport properties above room temperature were interpreted in terms of combined fluctuation-assisted tunneling and variable-range hopping mechanisms.

From the application perspective, the very high thermal conductivity, κ, along the long axis of CNT could be useful in macroscopic applications if a method of aggregating the tubes that preserved κ were available. The value of κ along the long axis of a single CNT can be as high as 3000 W/(m-K) at room temperature [61]. On the other hand, uncompressed bulk samples of nanotubes have a room temperature $\kappa \approx 15$ W/(m-K) along the tube direction [87], while the SPS-densified, randomly oriented CNT bulk samples have $\kappa \approx 3$ W/(m-K) [64]. Apparently, heat transport in an array of nanotubes is profoundly affected by both the alignment of CNTs and the inter-tube bonding. Here we introduce another method of aggregation, viz, SPS of aligned tubes. We find that this method enhances the connection between pre-aligned MWCNTs, leading to $\kappa \approx 31$ W/(m-K) along the length of the nanotubes in an anisotropic aligned MWCNT bulk sample.

3.2 Mechanism of SPS Process[1]

SPS is a high-speed powder consolidation/sintering technology capable of processing conductive and nonconductive materials. Figure 3.1a shows the basic configuration of the SPS system. The sample is loaded in a graphite die with two graphite punches, one on the top and another at the bottom. Pressure and pulsed electrical current are applied through these punches. A T. C. well is used to monitor the average temperature of the graphite die.

---

[1] All information in this section comes from SPS Syntex Inc.

Theories on the SPS process vary, but the most commonly accepted is the micro-spark/plasma concept, which is based on the electrical spark discharge phenomenon wherein a high-energy, low-voltage pulse current momentarily generates spark plasma at high temperatures (many thousands of °C) in fine local areas between particles. SPS utilizes uniaxial force and on–off d.c. pulse energizing. The on–off d.c. pulse voltage and current creates spark discharge and Joule heat points between material particles (high-energy pulses at the point of intergranular bonding). The high frequency transfers and disperses the spark/Joule heat phenomena throughout the specimen, resulting in a rapid and thorough heat distribution, high homogeneity and consistent densities. When spark discharges appear in the gap between the particles of a material, a local high temperature state of several to ten thousand ^{o}C momentarily occurs. This causes vaporization and the melting of the surfaces of the powder particles during the SPS process; constricted shapes or "necks" are formed around the contact area between the particles as depicted in Fig. 3.1b. The ongoing "radiant" Joule heat and pressure causes these necks to gradually develop and increase. The radiant heat also causes plastic deformation on the surface of the particles, which is necessary for preparing highly compacted bulk samples.

During the SPS process, heat is concentrated primarily on the surfaces of the particles. Particle growth is limited due to the speed of the process and the fact that only the surface temperature of the particles rises rapidly. The entire process—from powder to finished bulk sample—is completed quickly, with high uniformity and without changing the particles' characteristics.

SPS is effective for any powder sample, but interest is especially high for nanocrystalline structures which have more surface area per volume than the same material made with larger particles. In the following section, we will show how we weld the neighboring tubes together using the SPS process.

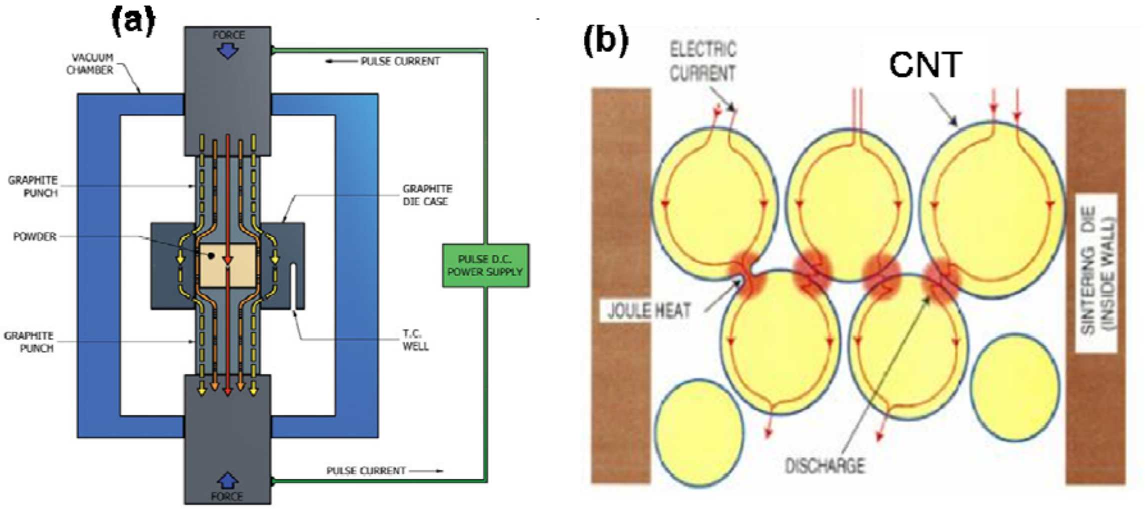

Figure 3.1 (a) Basic configuration of the SPS system with On/Off pulsed current path through the machine. (b) Schematic picture of SPS process. When pulsed electric current passes through the sample, Joule heat and discharge are generated between gaps between the particles. The “necks” are formed because of the vaporization/melting and sintering of the particle surface.

3.3 Experiments

The MWCNTs used in this study were prepared by the thermal chemical vapor deposition (CVD) method. A CVD system (as depicted in Fig. 3.2) consists of feed gases, an injection system, a preheater and a furnace with temperature controllers, and an exhaust system. The CVD system also includes a quartz tube, leak free endcaps, and the quartz substrates that are place in the furnace for the collection of well-aligned nanotubes. MWCNTs are grown on bare quartz substrates by injecting a mixture of ferrocene ($C_{10}H_{10}Fe$) and xylene (C_8H_{10}) with 0.16 at.% Fe into a two-stage thermal CVD reactor consisting of a low temperature (~300 ^{o}C) preheater followed by a higher temperature main reactor (~900 ^{o}C) [88]. The flow rates of the carrier gases are 100 SCCM for hydrogen and 500 SCCM for argon. During the nanotube synthesis, ferrocene and xylene are vaporized in the preheater zone and swept to the main reactor immediately with carrier gases. Ferrocene and xylene are decomposed in the main reactor zone. Carbon atoms are deposited on the exposed upper surface of the metal particles and diffuse through and over the metal to precipitate at the opposite face in the form of nanotubes. Once initial nanotube growth is established, growth will tend to continue in this same direction in a confined space because of the presence of surrounding tubes. Vertically aligned MWCNTs mats are produced in situ on quartz substrates.

To get aligned MWCNT bulk samples using the SPS process, the MWCNT arrays have to be pre-aligned before loading into the graphite die. Thus the MWCNT array must be long enough for handling purpose. The MWCNTs synthesized by a traditional CVD method have a length only up to a few hundreds of μm depending on the synthesis time.

G. Zhang et al, [89] have shown that the addition of oxygen scavenges H species and provides a powerful control over the C/H ratio to favor SWCNT growth. Following the same idea, a small mount of oxygen was added during the MWCNT synthesis. This increases the growth rate of MWCNTs dramatically. A 2 mm long MWCNT array can be grown in a 1.5 hour CVD run.

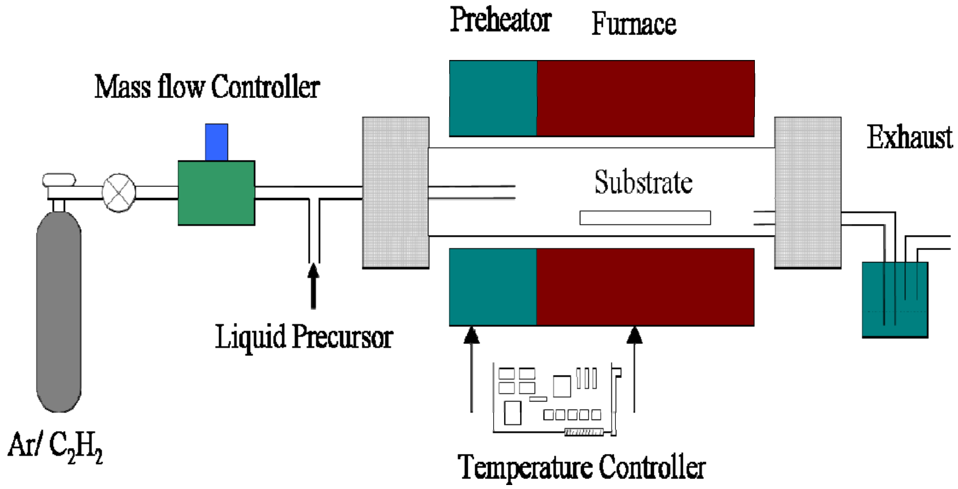

Fig. 3.2 A two stage thermal CVD reactor: The MWCNTs are grown on bare quartz substrates by injecting a liquid precursor into a two-stage thermal CVD reactor consisting of a low temperature (~300 ^oC) preheater followed by a higher temperature furnace (~900 ^oC) [90].

The as-grown 2-3 mm long MWCNT arrays were peeled from the substrates and stacked between two graphite electrodes as shown schematically in Fig. 3.3a. The stacked arrays were subjected to the SPS process (SPS, Dr. Sinter 1020, Sumitomo Coal Mining CO., Ltd., Japan) in vacuum at 1500 ^{o}C for 5 min under 7 MPa axial pressures. An SPS current (~600 A) in the transverse direction of the stacked MWCNT arrays resulted in the formation of a dense aligned MWCNT bulk sample pellet: density = 1.62 g/cm^3 as determined by Archimedes' method. The crystallinity and morphology, before and after the SPS process, were checked using X-ray diffraction (XRD, Rigaku® miniflex), Raman spectroscopy (ISATriax 550, JobinYvon, excitation wavelength = 514.5 nm), field emission scanning electron microscope (FESEM, Hitachi® S4800), and high-resolution transmission electron microscopy (HRTEM, Hitachi® TEM 9500).

Two bars (dimensions 5×2×1 mm^3) were cut from an aligned MWCNT bulk sample pellet, one along the longitudinal direction (i.e., along the long axis of the MWCNTs) and the other along the transverse direction (i.e., perpendicular to the long axis of the MWCNTs). Seebeck coefficient, S, the electrical resistivity, ρ, and κ of the bar shaped samples were measured in the temperature range from 10 to 320 K. The details of measurements can be found in reference [91-92]. For the ρ and κ measurements, a conventional 4-probe configuration was adopted. In addition, the Hall coefficient R_H was measured along both directions using a 5-probe configuration on a Quantum Design® PPMS with the magnetic field swept between +/- 0.5 T. In all transport measurements, silver paint was used to form ohmic contacts.

3.4 Microstructural characterization

The SEM images in Fig. 3.3b and c show that individual MWCNTs retain their original orientation, tube diameter (~30-50 nm) and tubular morphology after the SPS process. Comparison of Fig. 3.3b and c shows the effect of densification. While the MWCNTs are not perfectly straight nor perfectly aligned, a preferred direction is nonetheless clear in Fig. 3.3c.

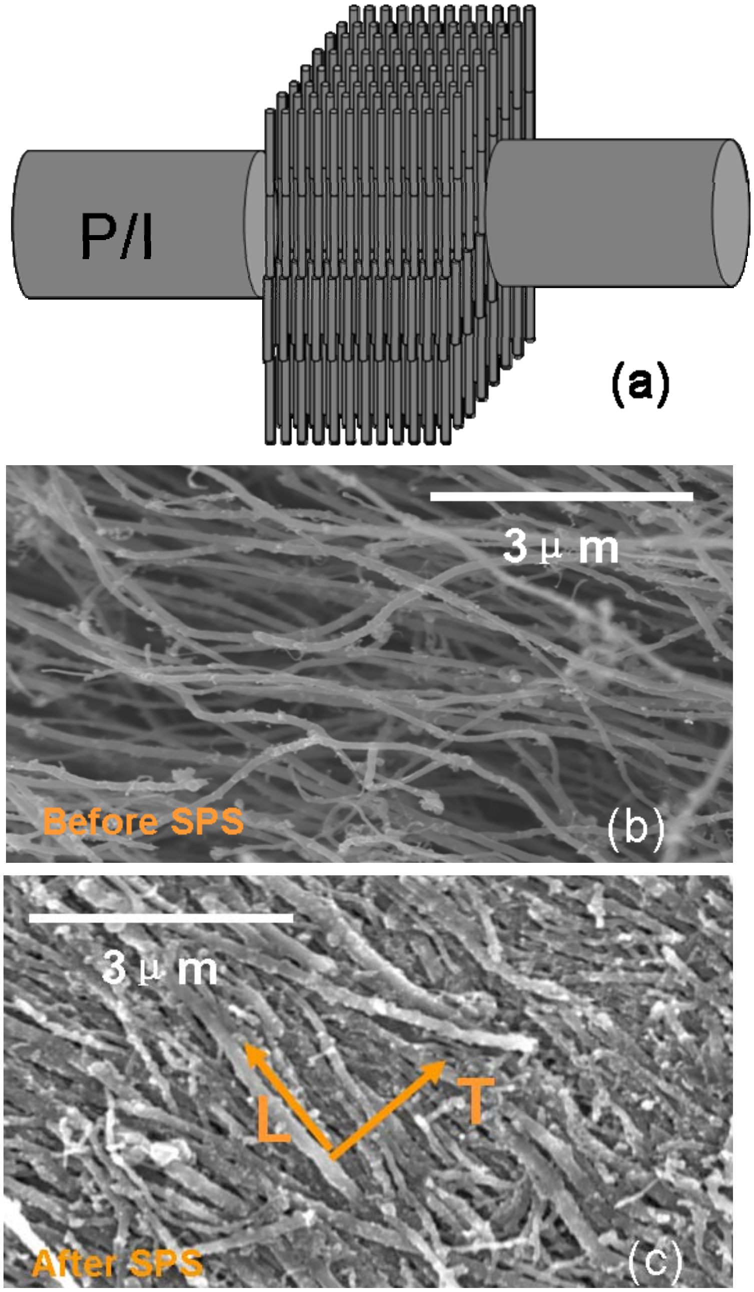

Figure 3.3 (a) Schematic of the SPS process: MWCNT arrays are stacked between two graphite electrodes, and pressure and electrical current (P/I) are applied along the transverse direction. (b) A typical SEM image of as grown MWCNTs. The MWCNTs are

loosely packed, and the tube-tube distance is in the hundreds of nanometers range. (c) SEM image of MWCNTs after SPS processing. MWCNTs retain their orientation, diameter, and tubular morphology after SPS processing, but the tube-tube distance is dramatically decreased after the SPS process. The images in (b) and (c) are not taken from the same area of the sample.

Figure 3.4 presents the XRD patterns of the as-grown MWCNTs and the aligned MWCNT bulk samples. Indices of (0 0 2) and (0 0 4) correspond to interplanar distance in graphite. While no new peaks are observed, a decrease in the full width at half maximum (FWHM) of the (0 0 2) peak suggests that the MWCNTs exhibit higher graphitization following the SPS process. This observation is consistent with the Raman data shown in Fig. 3.5 in which the integrated intensity ratio $R = I_D/I_G$ decreases from 1.55 to 1.32, where the subscripts D and G represent the disorder-induced and graphite-like peaks, respectively [93]. It is well known that a decrease in the ratio of I_D/I_G and the FWHM of these peaks imply an increase in the in-plane crystallite size, *La*, in carbon materials. The shoulder near the G-peak at ~1620 cm^{-1} is called the D' peak whose origin is identified with the activation of zone-edge and mid-zone phonons. Note that the characteristic 1333 cm^{-1} peak for sp^3 bonding is absent in Fig. 3.4. Interestingly, while the positions of the D band (~1355 cm^{-1}) and G band (~1583 cm^{-1}) remain the same after sintering, the G' band (~2700 cm^{-1}) is found to be up-shifted by ~5 cm^{-1} (Fig. 3 inset). We have found no literature reports about shifting of the G' band due to thermal treatment of

CNT [33, 94]. On the other hand, several groups also reported that the defects or dopants in carbon network can cause the shifting of G' band [34, 95]. We attribute this shifting of G' band to the formation of defects in the sidewall of the MWCNTs during the SPS process.

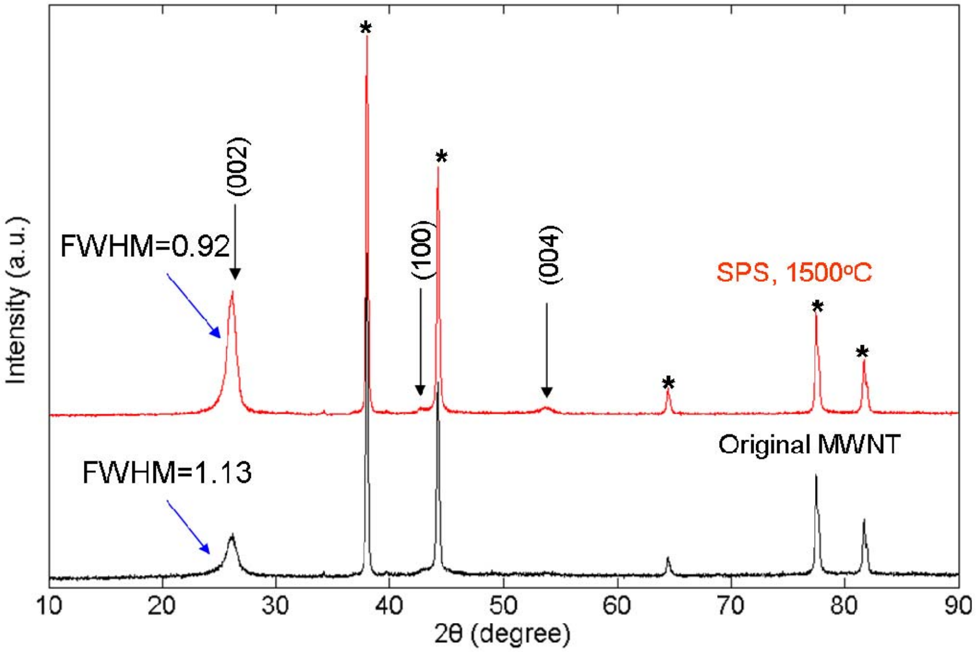

Fig. 3.4 XRD patterns for MWCNTs. No new peaks were detected after the SPS process. The XRD pattern shows that the SPS process improved the crystallinity of the MWCNTs. Peaks labeled with asterisks are due to the aluminum sample holder.

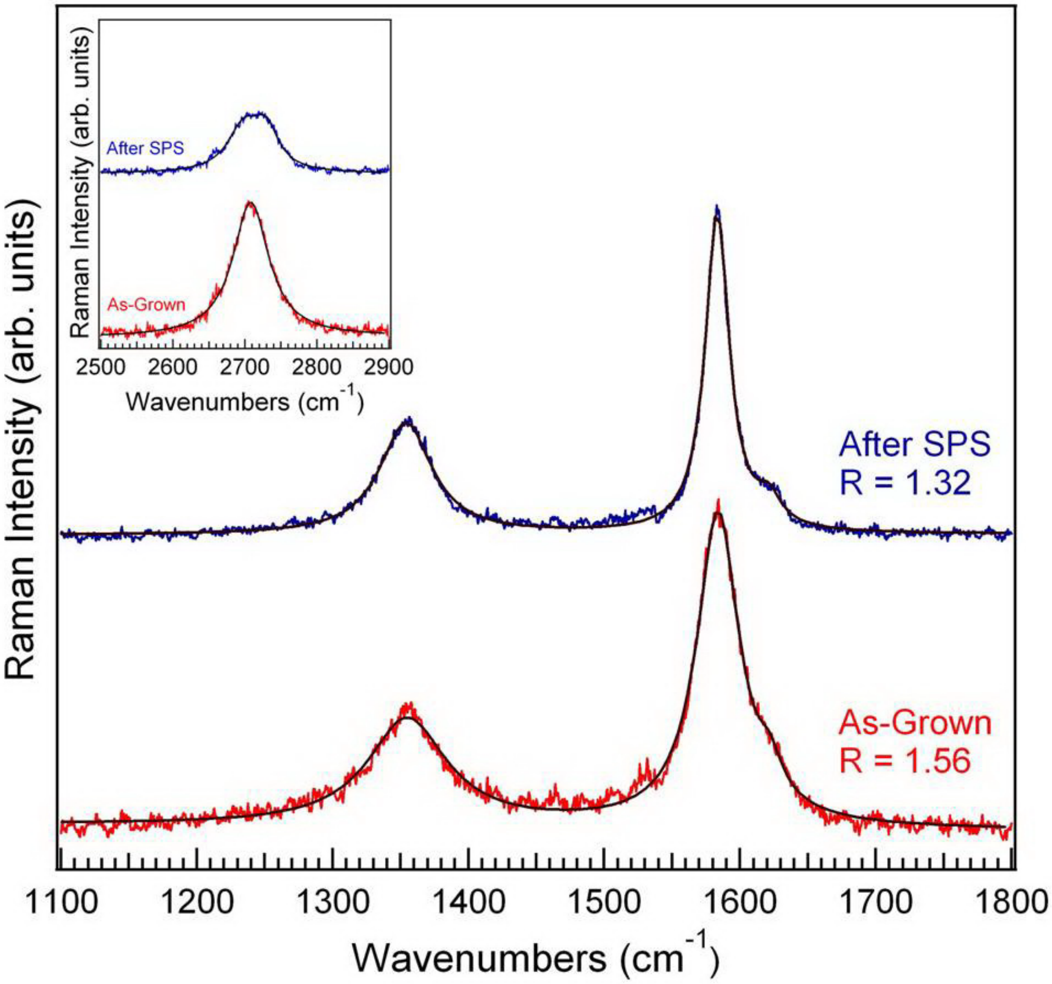

Fig. 3.5 Raman spectra of the MWCNTs before and after the SPS process. After SPS processing, the positions of the D band (1355 cm^{-1}) and the G band (1583 cm^{-1}) remain the same, but the integrated intensity ratio I_D/I_G decreases. The inset shows the G' band shifts upward about 5 cm^{-1} after SPS processing.

HRTEM studies provide evidence for the following structural changes induced by the SPS process: (i) as-grown MWCNTs with relatively straight sidewalls (Fig. 3.6a) are found to weld locally to neighboring MWCNTs (Fig. 3.6b). (ii) Formation of kinks, corrugation, or collapse of sidewalls in individual MWCNTs in the aligned MWCNT bulk samples (Figs. 3.6b and c). (iii) The presence of graphene comprising of 4-5 layers (Fig. 3.6d). Because of the geometry used in our SPS process (Fig. 3.3(a)), the large transverse current density (~10^2 A/cm^2) may results in knock-on collisions of electrons with carbon atoms, leading to the formation of vacancies and interstitials (cf. Banhart) [24-25]. The SPS-induced defects lead to the formation of local welds or graphene layers between MWCNTs (as shown schematically in Fig. 3.6e). Finally, it should be mentioned that the current density used in this study (~10^2 A/cm^2) is orders of magnitude lower than that used in the electron irradiation process (~10^4 A/cm^2) [25]. As a result, there is no evidence for the formation of spherical carbon onions.

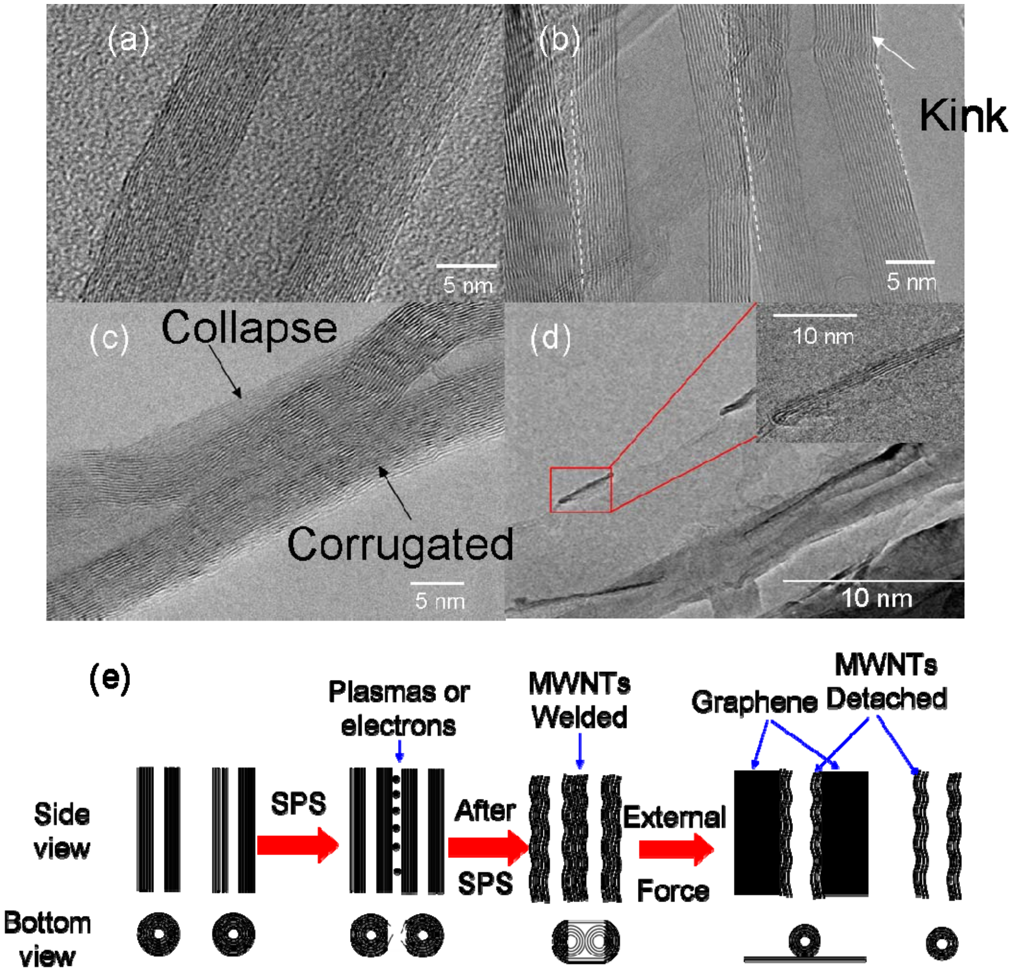

Fig. 3.6 (a) A typical HRTEM image of as-grown MWCNTs revealing clean sidewalls with relatively few defects. Panels (b), (c), (d) show typical HRTEM images of MWCNTs after the SPS process. In (b), at least three MWCNTs are found welded together with some corrugations present in the sidewalls. (c) A partially collapsed MWCNT. (d) Residual graphene layers which presumably result from bonded tubes being detached from each other. The inset shows the edge of the graphene layer. (e) Schematic representation of the SPS-induced process of morphological changes of

MWCNTs seen in the HRTEM. The external mechanical force represents either grinding and/or sonication, which have to be used during the sample preparation for HRTEM studies.

3.5 Transport properties

3.5.1 Electrical conductivity

The SPS-induced structural changes described above are expected to profoundly affect the transport properties of aligned MWCNT bulk samples. It is well known that ρ_T is much greater than ρ_L in films and bulk materials comprised of aligned CNTs [63, 96]. Figure 3.7 (a) shows ρ for aligned MWCNT bulk samples along both directions from 10 to 320 K. ρ was calculated using the resistance of the sample R, cross-sectional area A and the distance between the voltage leads L in a four probe configuration ($\rho = RA/L$). In both directions ρ shows a nonmetallic behavior, that is, $d\rho/dT < 0$. Interestingly, ρ_T is slightly lower than ρ_L. As discussed above, the SPS process generated new inter-tube bonding, in addition to formation of graphene, which presumably connects nanotubes in the transverse direction, and lowers ρ_T.[2] An additional reason for $\rho_T < \rho_L$ is that the effective cross-sectional area of the conducting matter as seen looking down the nanotubes is smaller than A because of the hollow core in each nanotube and the inter-tube spacing in the array. Furthermore, in the longitudinal direction, the presence of SPS-

---

[2] The low temperature (5 K) i-V response along the transverse direction confirmed ohmic behavior in aligned MWCNT bulk samples, irrespective of the frequency and current density

induced corrugated side walls, kinks and collapse of the MWCNT cores are expected to increase ρ_L. It is not obvious, however, that these effects will override the higher conductivity along the axes of the tubes. ρ_L and ρ_T are two orders of magnitude lower than ρ of highly orientated pyrolytic graphite along the perpendicular direction (~0.2 *Ω-cm*) at room temperature.[3] All these results further corroborate inter-tubular bonding in aligned MWCNT bulk samples.

In order to explain the temperature dependence of ρ in Fig. 3.7a, we have considered several models from the published literature, such as the Luttinger liquid model [43], variable-range hopping [64, 97] or weak localization theory [45]. However, none of these models could adequately describe our experimentally data over the entire temperature range as shown in Fig. 3.8. It is noteworthy that (i) ρ follows a nearly $T^{1/2}$ dependence (Fig. 3.7(b)), similar to the $\rho(T)$ data reported by Tsai *et al.* for an individual disordered MWCNT [98], and (ii) the $T^{1/2}$ dependence has been attributed to electron-electron scattering in the presence of random impurities in the 1D case [99]. In Fig. 3.7b, solid lines represent $\rho(T)$ according to the Altshuler-Aronov model [98-99]:

$$\rho = \rho_0 - \alpha \times \sqrt{T} \qquad 3.1$$

where ρ_0 is ρ extrapolated to 0 K, and α is related to the momentum relaxation time due to scattering by impurities, and depends on the chemical potential. The true conduction paths in the aligned MWCNT bulk samples must be quite tortuous. The nearly $T^{1/2}$ behavior of ρ_L and ρ_T is unlikely to be due to weak localization because of (a) the fit to

---

[3] http://www.tectra.de/hopg.htm.

the ρ_L and ρ_T *vs.* T curves is not good, and (b) the dimensionality of the samples is not one-dimensional, especially in the transverse direction. Nonetheless, along the longitudinal direction, there may be parts of the conduction paths that are nearly one-dimensional (Fig. 3.7f), and perhaps that accounts for the qualitative fit of even ρ_T to $T^{1/2}$ [99].

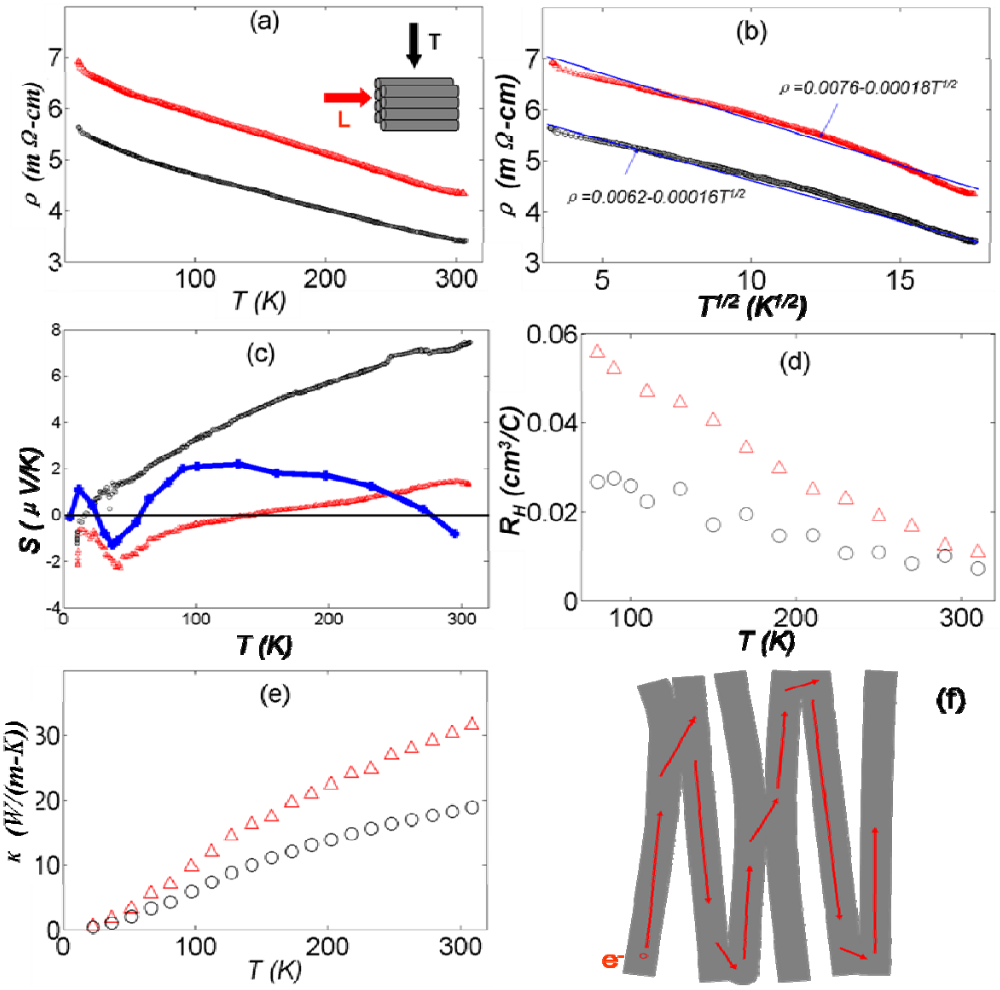

Fig. 3.7 The temperature dependence of resistivity is shown in (a) and (b); TEP in (c), the Hall coefficient in (d), and the thermal conductivity in (e). A schematic representation of the conduction path in the transverse direction is shown in (f). Red triangles (black circles) represent data along the longitudinal (transverse) directions. A qualitative linear relationship (blue solid lines) between resistivity and $T^{1/2}$ over the entire temperature range is evident in (b). The in-plane *S* of "kish" graphite (blue squares) [100] is also shown in (c) for comparison.

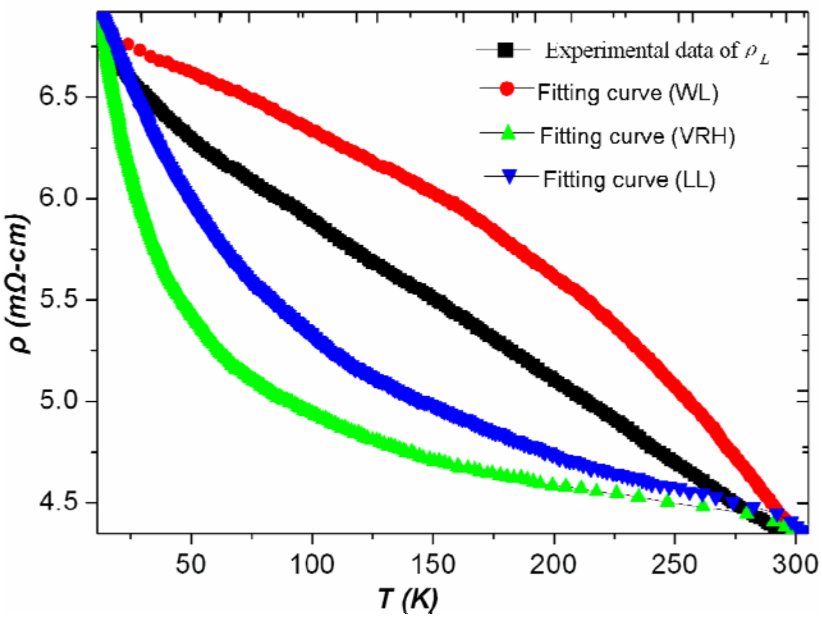

Figure 3.8 Experimental data with the fitting curves over whole temperature range based on different scattering mechanisms, such as weak localization (WL) theory [43], variable-range hopping (VRH) model [64, 97] and Luttinger liquid (LL) theory [43].

3.5.2 Thermoelectric power and Hall coefficient

In a system with a high density of boundaries, the temperature dependence of S is a more reliable parameter for probing the intrinsic conduction of MWCNTs. $S(T)$ measured along both directions is presented in Fig. 3.7c. It is well known that $S(T)$ in CNTs is sensitive to the type of environment in which the measurements are performed [72, 75]. In the present study, we annealed the aligned MWCNT bulk samples under vacuum at 120 ^{o}C for 24 h, and immediately measured $S(T)$. Both $\rho(T)$ and $S(T)$ were found to be identical to corresponding data in the un-annealed aligned MWCNT bulk samples.

The room temperature value for both S_T and S_L exhibit *p*-type characteristics suggesting that holes are the dominant carriers. This is consistent with the positive sign of R_H measured along both directions (Fig. 3.7d). Strong tube-tube interaction will introduce band gaps near E_F. The kinks and inter-tube bonding introduced by SPS are expected to change the electronic density of states near the Fermi surface (more details in Chapter 2). We speculate that some new localized acceptor states appear in the valence band, which makes the MWCNT bulk sample a *p*-type conductor [6].

S_L shows a prominent dip around 40 K (a hint of dip also appears in the S_T data) which matches the well known (both in temperature and shape of the dip) phonon drag peak observed in "kish" graphite samples (Fig. 3.7c). To the best of our knowledge, this is the first evidence for a strong phonon drag effect in $S(T)$ of CNT [78]. Since the 3rd law of thermodynamics requires S to approach zero as T approaches zero (TEP is a measure of entropy per charge carrier), we can reasonably guess there will be at least one more minimum below 10 K (10 K is the limit of our instrument). We compared our *S(T)* data with that of highly oriented pyrolytic graphite (HOPG) and kish graphite. They show similar behavior (superimposed in Fig. 3.7c) and thus we believe that the same mechanism is present in our results. K. Sugihara, et al. [100] attributed *S* anomaly in graphite to a two-state phonon drag effect. In the two-stage phonon drag model, a concept of an electronic phonon, which can interact with both carriers and short wave phonons, is introduced. They assumed the short wave phonons come to an equilibrium state through the active Umklap_process (U-process). At low temperature, the U-process is inactive and accordingly the short wave phonons deviated from the thermal equilibrium. Then, the short wave phonons drag carriers via electronic phonons. Within the framework of this interpretation, the observation of the low-temperature peaks in *S(T)* depends critically on the quality and purity of the graphite crystals in the experiments. On the other hand, J. Gerin et al. [101], tried to explain this TEP anomaly on the base of the enhanced coupling by anisotropy of the "Kohn phonons" with the majority carriers. While we are fully aware that people still argue about the origin of phonon drag in HOPG at low temperature, more and less a coherent and complete understanding of the phonon drag, in either case, is subject to having well defined band structure and phonon spectrum - both of which are lacking for MWCNTs at the present time. So we limit ourselves in discussing the origin of phonon drag in this chapter. These phonon drag features imply that the mean free paths of both electrons and phonons in our aligned MWCNT bulk samples are long enough, in other words, the aligned MWCNT bulk sample has good crystallinity, (similar to HOPG and kish graphite), at least in many parts of the sample.

TEP is generally comprised of two terms: one due to the Fermi surface topology and the other to energy-dependent scattering term. It can be seen in Fig. 3.7c that the temperature dependent parts of S_L and S_T are similar, suggesting that the band structure of an aligned MWCNT bulk sample is anisotropic. S_L (S_T) changes sign from positive to negative around 150 K (15 K). These sign changes point toward a complex multi-band band structure in aligned MWCNT bulk samples [73]. As a general rule, electron-phonon scattering will result in a negative phonon-drag S_g if the **q** vector of the absorbed phonon crosses an occupied region of the BZ; S_g will be positive if the **q** vector crosses an unoccupied region of the BZ [67]. The "S" shape of $S_L(T)$ suggests the existence of a complex Fermi surface in our aligned MWCNT bulk sample.

We also performed R_H measurements. The results are shown in Fig. 3.7d. Note that R_H along both directions is *p*-type between 70 and 300 K. Despite the complex multi-band structure of aligned MWCNT bulk samples, R_H provides an order-of-magnitude estimate of the carrier concentration. Our R_H data yields a carrier concentration of about 10^{20} cm^{-3}, compared with Baumgartner's results (10^{19} cm^{-3}) [102]. Still, as aligned MWCNT bulk samples may have several bands of holes/electrons, it is risky to interpret the temperature variations of R_H in this manner.

3.5.3 Thermal conductivity

Both theoretical and experimental results show that individual CNTs have an extremely high κ_L (theoretical number: 6600 W/(m-K) [60]; experimental number: 3000

W/(m-K) [61]). However, with increasing dimensionality the magnitude of κ decreases dramatically: for 2-D CNT film/bucky paper, the room temperature value of κ is in the range of 20-200 W/(m-K) [63]; for 3-D CNT bulk material, the room temperature κ is between 3-15 W/(m-K) [64-65]. Fig. 3.7e shows the measured κ of an aligned MWCNT bulk sample along both directions. κ increases monotonically with increasing temperature in both cases. We obtain $\kappa \sim 31$ W/(m-K) at 300 K in the longitudinal direction, which is one of the highest reported for 3-D CNT material. At room temperature κ shows considerable anisotropy: $\kappa_L / \kappa_T \sim 1.7$, which is expected from the alignment of the MWCNTs. In an anisotropic bulk crystalline material, the anisotropy of ρ is usually far larger than κ. However, the case here is notably different.

To a first order approximation, the phonon drag feature in Fig. 3.7c, is due to carriers being preferentially scattered by the phonons in the direction of heat flow. The magnitude of the phonon drag dip is inversely correlated to the carrier mobility and directly correlated to the sound velocity. In other words, the phonon drag effect should be more pronounced along the high κ direction. This is exactly what we observe in aligned MWCNT bulk sample.

The value of $\kappa/(\sigma T)$ is about 4.41×10^{-6} V^2K^{-2} and 2.08×10^{-6} V^2K^{-2} at 300 K, along the longitudinal and transverse directions respectively, two orders of magnitude greater than the value of the Lorentz number, confirming that κ is dominated by the lattice heat contribution. In the context of the kinetic model of heat conduction, we have $\kappa \sim Cvl$, where C is the specific heat, v the sound velocity and l the phonon mean free path (MFP). With $\kappa = 31$ W/(m-K), v around 10^4 m/s [103], and using $C \sim 10^3$ J/(kg-K) [104], we can estimate that l is around 3 nm. The value is considerably lower than other reports [105]. We believe this is due to point defect scattering and the corrugation on the side walls. The temperature dependence of the lattice thermal conductivity is amorphous-like, with a positive temperature coefficient. We speculate that l is limited by defects at low temperatures, so that the temperature dependence of the lattice thermal conductivity very nearly follows that of the heat capacity. On the other hand, the phonon drag peaks seen in S data indicate much better crystallinity than the thermal conductivity data. This discrepancy needs to be addressed in future studies.

3.6 Conclusion

The SPS process improves the crystallinity of aligned MWCNT bulk samples, but also introduces new defects, such as, kinks, corrugation, collapse of sidewalls in MWCNTs and inter-tubular bondings between neighboring MWCNTs. Interesting abnormal electrical and thermal transport properties have been observed in aligned MWCNT bulk samples. Inter-tubular bonding improves ρ_T and κ_T such that ρ is nearly isotropic, but κ is relatively more anisotropic. A strong phonon drag effect is observed in $S_L(T)$ around 40 K, suggesting that the band structure of an aligned MWCNT bulk sample is somewhat similar to "kish" graphite and also corroborates the observed crystalline nature of aligned MWCNT bulk samples. The combined results from the microscopy, spectroscopy and transport measurements shed light on the extent to which the transport properties are inherited from those of single CNTs in the dimensionality transformation from one-dimensional conductor to a three-dimensional anisotropic bulk material in a

SPS-densified aligned MWCNT bulk sample. A trend of transition from MWCNT-like behavior to graphitic behavior due to the inter-tubular bonding is clearly presented.

But there are several questions we did not answer in this chapter. How do different SPS temperatures affect the transport properties of CNTs? Can we use the SPS method to improve σ of CNT buckypaper (BP) or CNT composite? What is the origin of the phonon drag effect in our S data? Most of these questions will be answered in next chapter. But instead of vertical aligned MWCNTs, we will focus on disordered, commercially available, MWCNT BP.

CHAPTER FOUR

MWCNT BUCKYPAER SINTERED AT DIFFERENT SPS TEMPERATURES

4.1 Introduction

Because of their unique electrical properties, macroscopic forms of CNTs such as arrays, yarns, fibers and films, have been reported and have made the macroscopic manipulation of CNTs feasible for broad applications. Carbon nanotube paper, which is a paper-like CNT film, also called buckypaper (BP), is expected to inherit many of the properties of CNTs. BPs have been proposed as a good electrically and thermally conductive film because single nanotubes have very high electrical and thermal conductivity. But due to the huge junction resistance [106], the electrical conductivity of CNT BP is far lower than that of a single CNT. P. N. Nirmalraj, et al., [106] showed that the transport in SWCNT networks is dominated by resistance at network junctions. In their works, conductance atomic force microscopy (C-AFM) was used to map the resistance of a nanotube bundle. Resistance along a single tube is almost linear, but a big jump shows up at the junction between tubes. Their work showed that the resistance of nanotube networks is mainly from the junction resistance as shown in Fig. 4.1.

To minimize the tube junction resistance, several ways have been proposed by different groups. J. Hone et al., [96] produced aligned SWCNT films by filtration/deposition from suspension in strong magnetic fields. The films show very low ρ (~ 0.125 mΩ-cm) and high κ (greater than 200 W/(m-K)) along the longitudinal direction (parallel to the axes of the tubes). D. Wang et al. [63] showed that high-quality BPs with aligned MWCNTs can be made by rolling a cylinder over the MWCNT array.

The alignment of the MWCNTs improved σ by a factor of 1.3 and κ by a factor of 2.5. Acid treatment is also known to enhance the conductivity of CNT material. P. N. Nirmalraj, et al., [106] showed that the resistance of tube junction was reduced by 3-fold after acid treatment. But all these methods either need multi steps or need special morphology of the nanotubes.

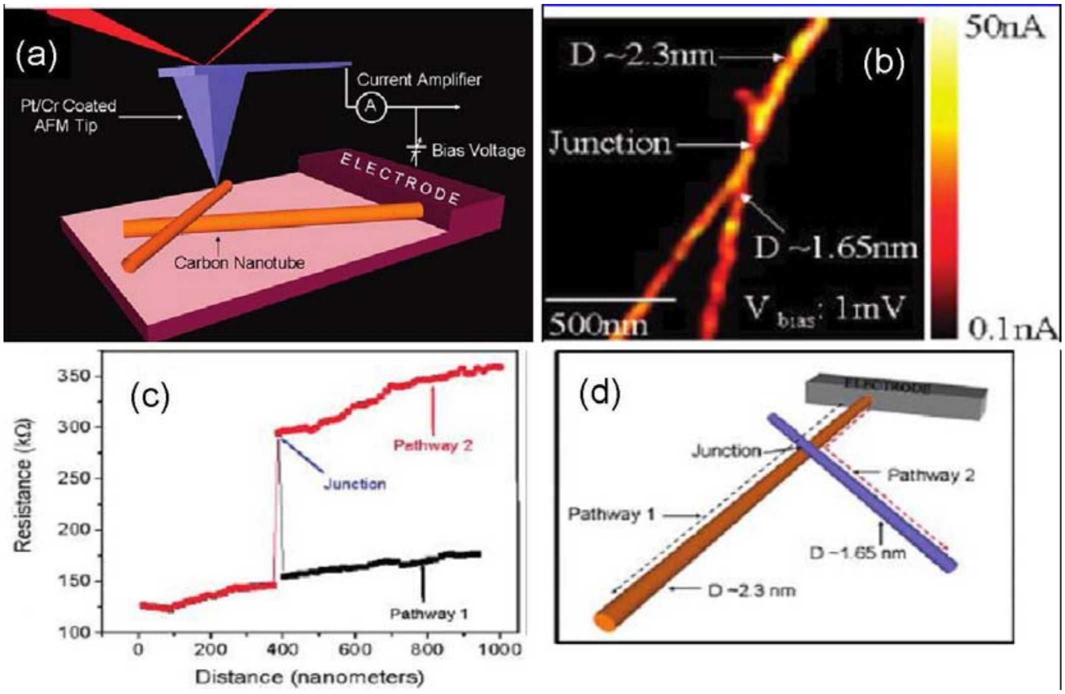

Figure 4.1 (a) Schematic of conductive atomic force microscope technique. (b) Current map of a nanotube bundle ($D \sim 2.3$ nm), which is intersected by an individual tube (($D \sim 1.65$ nm). The electrode is positioned on the tope of the image (not shown). (c) Local resistance analysis through the bundle and individual tube depicted as pathway 1 and 2 as shown in the schematic (d) [106].

In chapter 3 we have shown that the carbon atoms of MWCNT are rearranged by the SPS processing (at least in localized areas on the sidewall of MWCNTs, as shown, in Fig. 3.6) and inter-tube bondings are formed between tubes. These bonds enhance σ along the transverse direction without significantly lowering σ along the longitudinal direction. We also showed that the ρ_T is lower than ρ_L. In topology, the tube junctions are maximum along the transverse direction, but minimum along the longitudinal direction. SPS would be a fast, simple way to improve the electrical conductivity of MWCNT BPs.

In this chapter, we will show that the electrical conductivity of MWCNT BP is enhanced by one order of magnitude after SPS processing. The effects of SPS temperature are also explored. ρ of MWCNT-BP decreases with increasing SPS temperature (T_S), but is almost saturated at 1200 ^{o}C. The magnitude of $S(T)$ also decreases with the increasing T_S. A prominent anomaly in $S(T)$ appears around 50 K after BP is sintered at 1500 ^{o}C, which is attributed to the phonon drag effect. κ, on the contrary, increases with increasing T_S.

4.2 Experiment

The MWCNT-BPs used in this study are provided by NanoTechLabs, Inc. The MWCNT are synthesized using Fe as the catalyst and hydrocarbon compounds as carbon source. The MWCNTs are purified using mild nitric acid before fabricating BP. Over the 90% of the BP is MWCNTs based on SEM studies. All BPs used in this study come from the same piece of BP. The thickness of the BP is around 0.3 mm. For transport measurement, we stack six round pieces of BP with diameter of half inch together and placed them into a half inch graphite die in each of the SPS experiment discussed in this chapter. The pressure is kept at 7 MPa in all the SPS experiments, but the current is changed according to achieve different T_S. We sintered the BP at 500, 800, 900, 1000, 1200 and 1500 ^{o}C, and these samples are labeled as S500 S800, S900, S1000, S1200 and S1500, respectively. The density of the sample was estimated using $\rho = m/V$ (m is mass and V is volume). SEM was used to examine the morphology changes after SPS processing. ρ, S and κ are measured in the temperature range 10 K to 300 K, using methods similar to these described in Chapter 3.

4.3 Density and microstructure

Fig. 4.2 shows the relationship between the density of as-SPSed MWCNT BP and T_S. The density of MWCNT BP roughly increases linearly with T_S. For the S1500 sample, the density is about 3 times that of the as prepared sample (labeled as AP).

SEM studies show that SPS process doesn't change the morphology of single nanotubes, except to make the BP more condensed, which is consistent with what we observed for aligned MWCNT bulk samples (Chapter 3). Fig. 4.3 shows some typical SEM images of BP before and after sintering at different temperatures. The BP is composed of MWCNTs with diameter ~ 30 nm which do not have a preferred orientation. Impurities can be found some times. Figure 4.3a and b show that MWCNTs are loosely packed and there is no discernable difference between the AP sample (Fig. 4.3a) and S500 sample (Fig. 4.3b). Figure 4.3c and e are representative SEM images of S1000 and S1500 samples, respectively. Clearly MWCNTs become denser when T_s is higher. Some nanotubes are found welded together (Fig. 4.3d, and white circled areas in Fig. 4.3f) at certain areas, which are direct proofs for the strong inter-tube bonding formed during SPS process. This phenomenon can only be found in sample with T_s above 500 ^{o}C. Some localized alignment of MWCNTs can be found at some areas in both the AP sample and the as-SPSed samples. So we hesitate to attribute the alignment (shown in Fig. 4.3c and d) to the SPS process since all the images of Fig. 4.3 are taken from different areas.

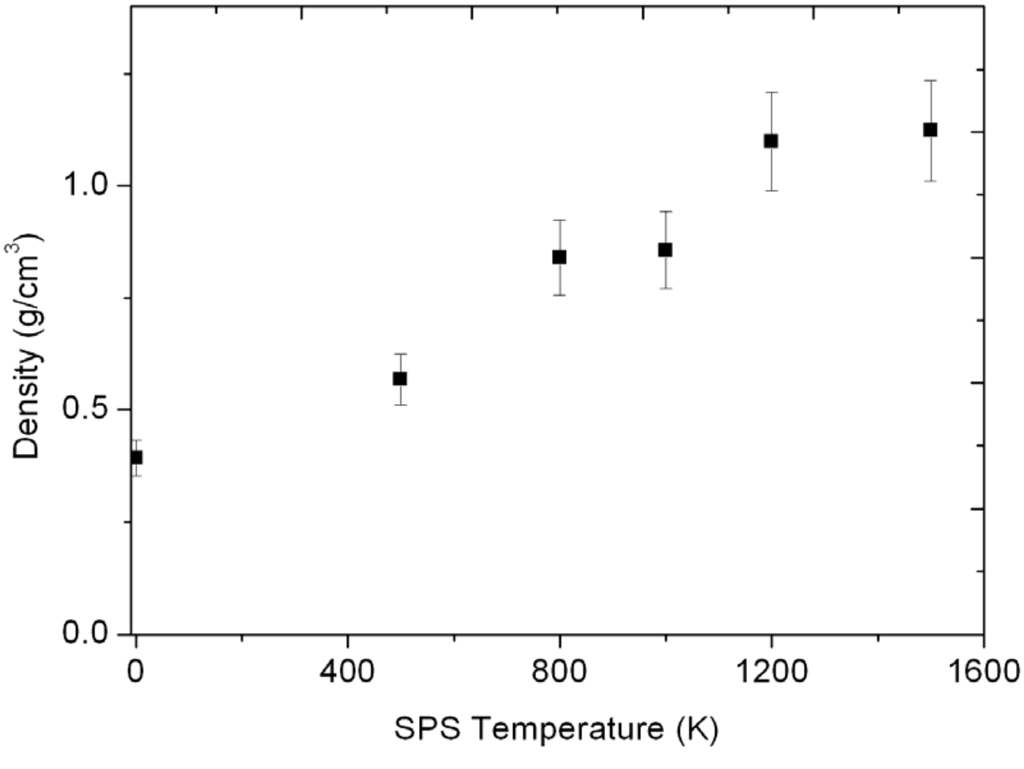

Figure 4.2 Density of MWCNT BP vs T_S with +/- 10% error bar.

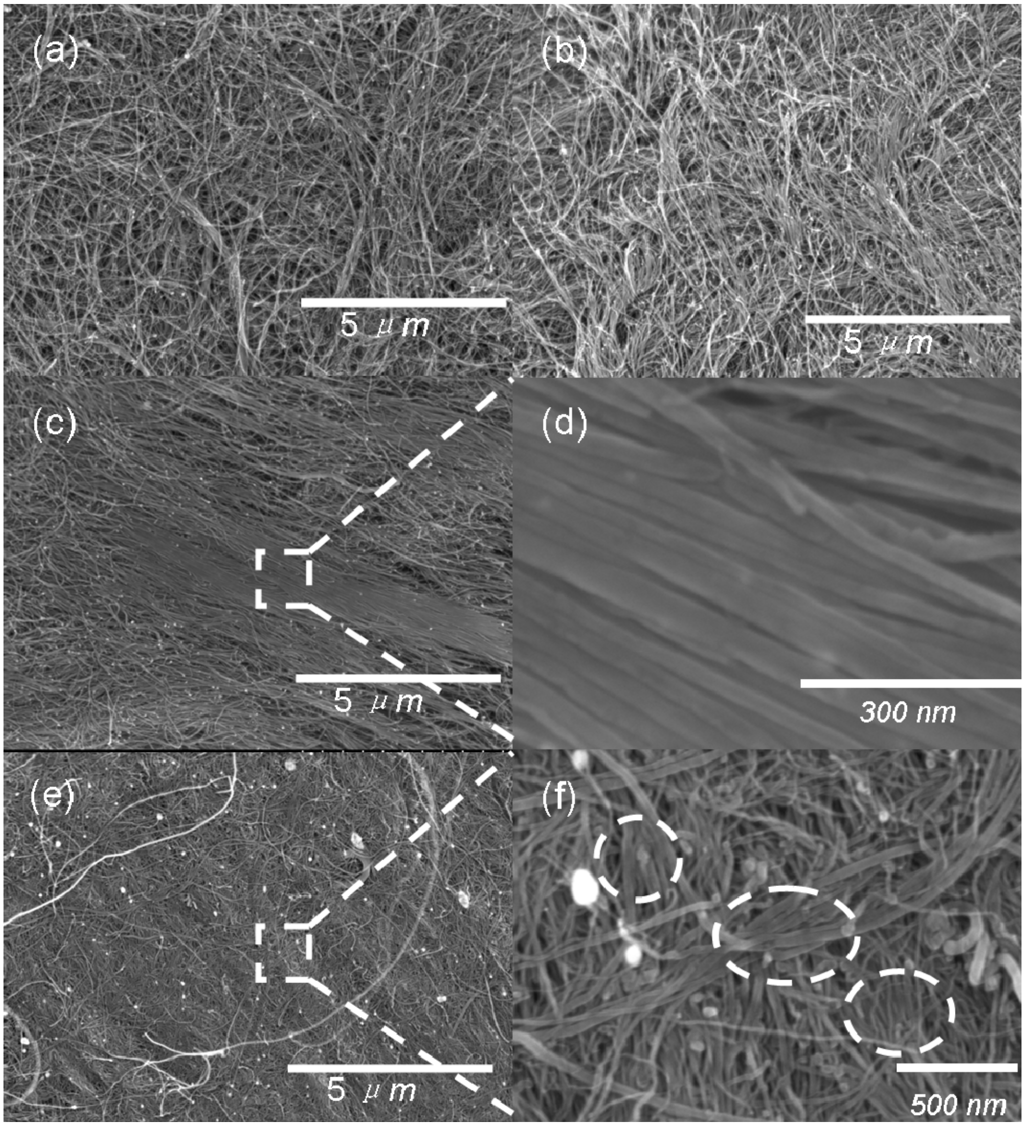

Figure 4.3 SEM image of (a) AP, (b) S500 (c), S1000 (e), and S1500. (d) and (f) are high magnification images of (c) and (e), respectively.

4.4 Transport Properties

4.4.1 Electrical resistivity

Figure 4.4a shows the temperature dependence of the resistivity of MCNT BP sintered at different temperature (we suppose that the SPS temperature of the AP sample is 25 ^{o}C). $\rho(T)$ decreases with increasing T_S over the whole temperature range and is saturated at $T_S \sim 1200$ ^{o}C. Since the dominate resistance comes from the tube-tube junctions in a CNT network [106], two possible reasons may account for the observed decrease in ρ. One possibility is that ρ of the tube-tube junction decreases with increasing T_S. In another words, at higher T_S, the energy barrier (E_B) between tubes becomes lower. E_B should be proportional to the tube-tube distance which account for the density dependence of BP on T_S. Another possibility is that the number of lowest E_B in CNT network increases with increasing T_S. T_S here is just an average temperature and the local temperature should be higher. The SPS temperature is proportional to the current passing through the CNT network. When higher current passes through the CNT network, more electrical pathways are building and more welding points between tubes are made (Fig. 4.3) during SPS process. These welding points presumably correspond to the tube-tube junctions with the lowest ρ or E_B. In this situation, when a complete percolation path is built in the CNT network, adding more welding points will hardly improve the conductance of the network [107-108].

During the SPS process, both situations may happen. E_B decreases and more welding points are formed with increasing T_S. Figure 4.4b depicts the relation between T_S and ρ at room temperature. This behavior falls under the marquee of percolation theory, which deals with the effects of varying the richness of interconnections present in a random system. Standard percolation theory predicts that the T_S dependence of the ρ is given by [109]

$$\rho \propto \left(T_S - T_{Th}\right)^{-\alpha} \tag{4.1}$$

Here, T_{Th} is the threshold T_S. Equation 4-1 holds in the vicinity of the transition; while well above the critical density, one expects to enter a linear or saturated region. The critical exponent, α, depends only on the dimensionality of the space; for a film in 2-D, theory predicts $\alpha = 1.33$, while in 3-D $\alpha = 1.94$ [110]. The inset of Fig. 4.4b shows a fit of Eqn. 4-1 to our data in the percolation region, using $T_{Th} = 500$ °C.[4] The best fit to our data yields an value of $\alpha = 1.3$[5], which is very close to what the theory predicts and literature reports for a 2-D case [111-112].

The lowest ρ is around 8 mΩ-cm at room temperature for the S1500 sample. This value is comparable to a single disordered MWCNT [98]. All samples show non-metallic behavior over the whole temperature range ($d\rho/dT < 0$) with ρ increasing monotonically with decreasing temperature. Normalized ρ (obtained by divided by the room temperature resistivity) for each sample is plotted in Fig. 4.5a. In the high-T range (above 100 K), $\rho(T)$ for all samples is linear with negative slope. In the low-T range (below 100 K), $\rho(T)$ shows a different temperature dependence for different samples. For AP and S500 samples, $\rho(T)$ is linear over almost the whole temperature range and tends to a constant

---

[4] The 500 °C is the lowest T_s we tested at which ρ begins to decrease. That is why we choose 500 °C as the thresh hold temperature. But 500 °C is reasonable since MWCNT is a chemical/energetically stable material and we do not expect low SPS temperature will change the properties of MWCNT too much.

[5] α depends on the choice of T_{Th}. But the influence of T_{Th} on α is very small, for example, if we chose $T_{Th} = 200$ °C, α is around 1.28.

below ~20 K (Fig. 4.5b), which may be due to the cut off of the EPC. On the other hand, an up-turn appears in the low-T range (below 100 K) for the as-SPSed samples above 500 ^{o}C. We can see that the SPS process predominantly changes the temperature dependence of resistivity at low-T. These results seem to suggest the EPC for MWCNTs can be tuned by T_s. To examine the $\rho(T)$ behavior more closely, we plot $\rho(T)$ for different samples separately in Fig. 4.5b, c and d.

Figure 4.5c and d show the $\rho(T)$ curve of as-SPSed samples with a logarithmic temperature scale. For the as-SPSed sample ($T_S > 800$ ^{o}C), over the whole temperature range investigated, $\rho(T)$ can be expressed by:

$$\rho(T) = AT + C(1 - B\ln(T)) \tag{4.2}$$

where A, B and C are constant for each sample. A is roughly same for all the samples, B scales with the resistivity of the sample, and C is in the range of 0.04-0.05. To explain this logarithmic temperature dependence of resistivity at low temperature, several possible mechanisms have been considered.

One possibility is the Kondo effect. For a dilute magnetic alloy, an interaction between the magnetic moments of the impurity atoms and the conduction electron spins of the host can cause a pronounced peak in $S(T)$ and an associated resistivity minimum [67, 113]. The resistivity due to the spin-spin interaction can roughly be expressed as $\rho_{spin} = c\ (1\ -b\ln T)$ at low temperature, where c and b are parameters related to the material itself. L. Grigorian et al. [71] showed that the catalyst particles in SWCNTs could affect the electrical transport properties dramatically. In their work, $S(T)$ of SWCNTs using Fe, Ni, or Co as a catalyst shows a giant and broad peak around 80 K, also the strong low-T

upturn is evident in $\rho(T)$ curves. In our case, besides the logarithmic temperature dependence of $\rho(T)$ at low T, a positive hump can also be found in our $S(T)$ for S 1500 samples (Fig. 4.6). But the hump is absent in similar data for for other samples which were sintered at other temperature. Furthermore, there is a little dip around ~15 K (in the data for S1500 sample) which cannot be explained within the Kondo effect framework. Thus, it is highly unlikely that the Kondo mechanism is responsible for the observed $\rho(T)$ behavior in S1500 sample.

Other possible mechanisms could be due to E_B caused by inter-tube junctions or defects present in the BP. When $kT > E_B$, conduction electrons diffuse across the energy barrier; when $kT < E_B$, conduction electrons can hop or tunnel through these energy barriers. But in this model, ρ due to the hopping or tunneling depends exponentially on the temperature ($\rho \sim exp\ (1/T)$) [114]. Strong logarithmic temperature dependence of ρ is found in all our as-SPSed samples (except S500). So this energy barrier model does not fit our data. Also, this logarithmic behavior is absent in the AP and S500 sample, which is contradict to what we expected based on energy barrier model.

Equation 4.2 resemble $\rho(T)$ of graphite-sulfur composites reported by R. Ricardo da Silva et al. [115]. In their studies, the C-S composite was prepared by hot press graphite and sulfur power at 650 K. Magnetization measurements support a superconducting behavior below T_C = 35 K. Zero-field $\rho(T)$ shows a transition from linear temperature dependence to logarithmic divergence near T_C point (Fig. 4.6), which was attributed to the resistivity behavior in two-dimensional superconductors in the regime of weakly localized Cooper pairs [116]. Considering that both CNT and graphite are carbon material but with different morphology, there is probability that as-SPSed BP samples have transport mechanisms similar to that of the C-S composites. If this is true, we should observe the Meissner effect in our S800 sample around 100 K. Perhaps due to the large amount of Fe catalyst particles in our samples, we haven’t observed the Meissner effect in our samples. Making non catalyst or non-magnetic catalyst containing MWCNT buckypaper and treating them by the SPS process, will be our future work.

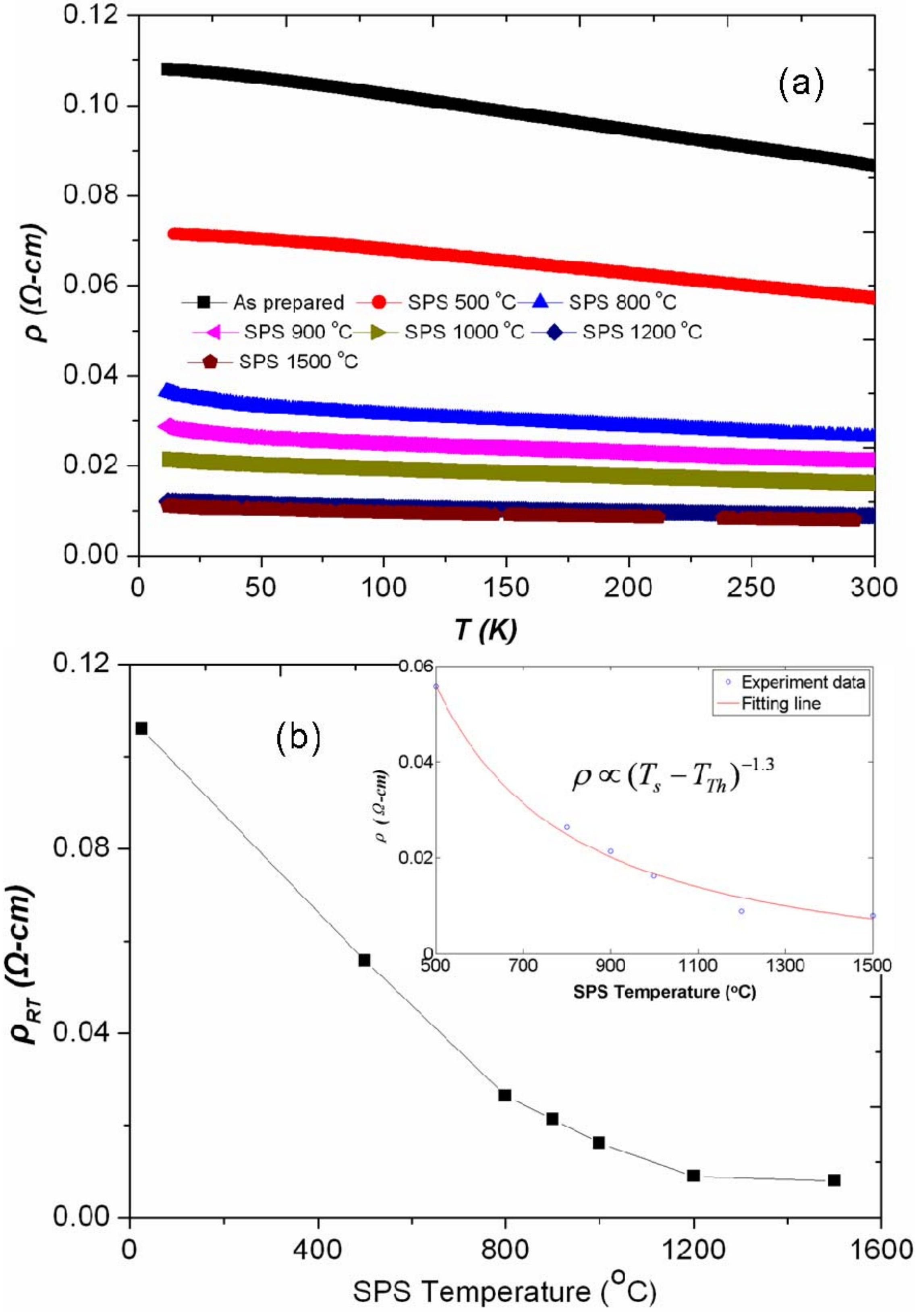(a)
ρ (Ω-cm)
T (K)
0.00
0.02
0.04
0.06
0.08
0.10
0.12
0
50
100
150
200
250
300
As prepared
SPS 500 °C
SPS 800 °C
SPS 900 °C
SPS 1000 °C
SPS 1200 °C
SPS 1500 °C
(b)
ρ_{RT} (Ω-cm)
SPS Temperature (°C)
0.00
0.04
0.08
0.12
0
400
800
1200
1600
Experiment data
Fitting line
$\rho \propto (T_s - T_{Th})^{-1.3}$
ρ (Ω-cm)
SPS Temperature (°C)
0
0.02
0.04
0.06
500
700
900
1100
1300
1500

Figure 4.4 (a) *ρ(T)* of MWCNT buckypaper sintered at different T_S. (b) *ρ vs* T_S at room temperature. Assume 500 °C is the critical T_S corresponding to the percolation threshold. The inset shows the power fit in the percolation region, where the critical exponent α = 1.3. Outside of the percolation region one starts to enter a saturate regime.

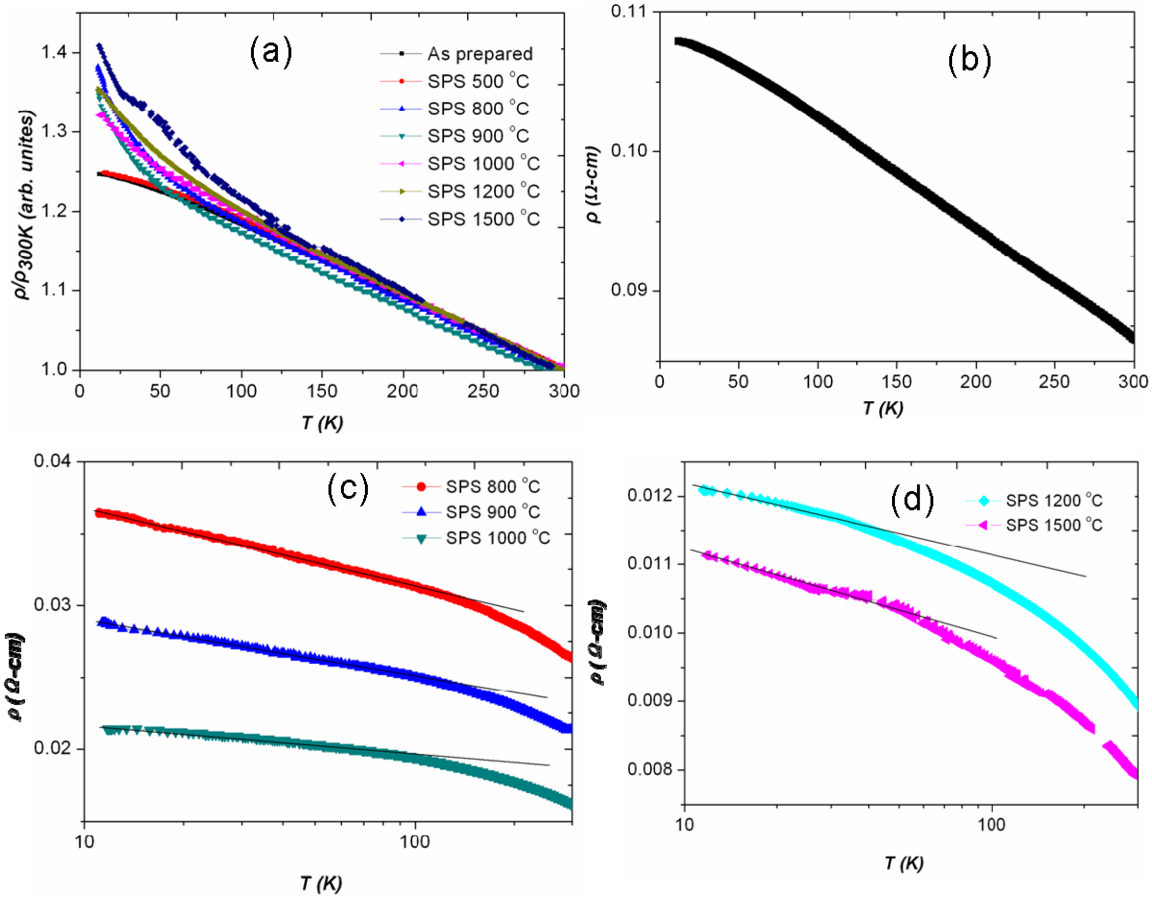

Figure 4.5 (a) Temperature dependence after normalizing *ρ* with ρ_{300} for every sample respectively. (b) *ρ(T)* of AP sample. (c), (d) Semilogarithmic plot of *ρ(T)* for samples S800, S900, S1000, S1200, and S1500. The solid line in (c) and (d) are guides for the eye.

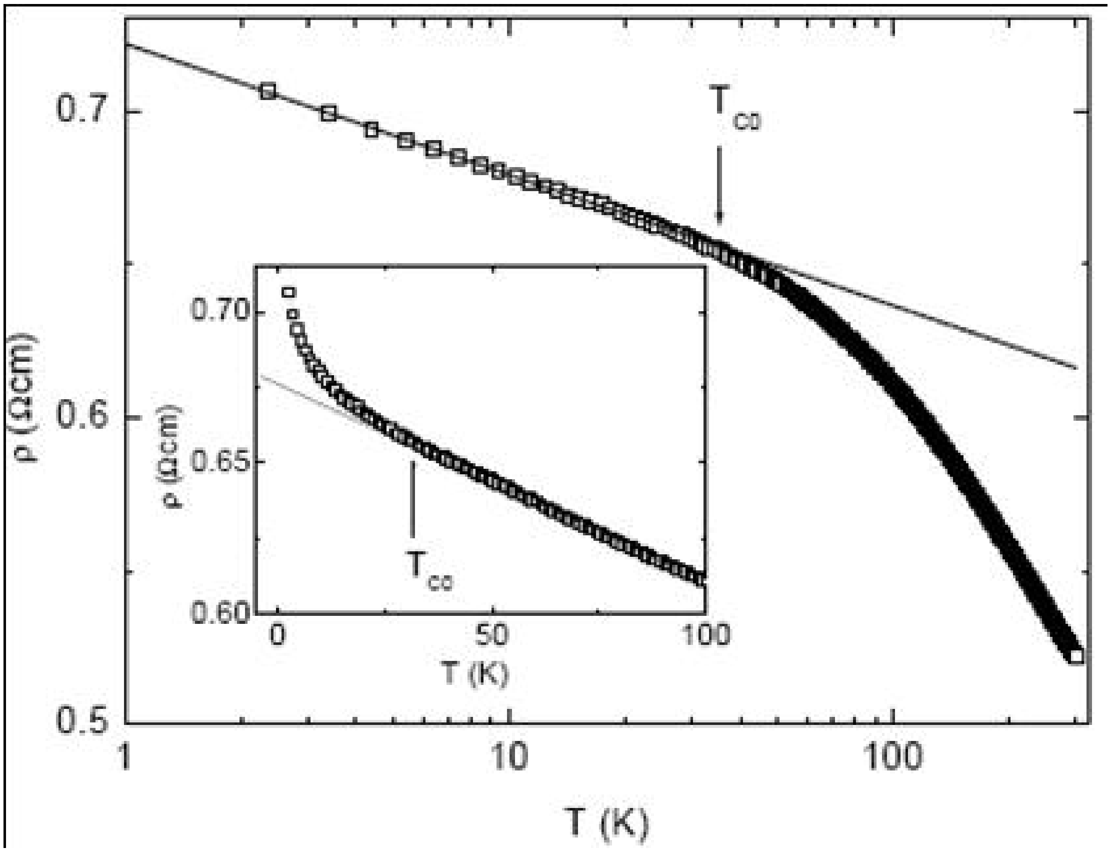

Figure 4.6 Semilogarithmic plot of zero-field resistivity $\rho(T)$ measured in graphite-sulfur composite; solid line is obtained from the equation $\rho(T)=0.6922+0.01855 \times \ln(5/T)$. Inset shows linear plot of the same data in a vicinity of $T_C = 35\ K$; solid line is only a guide [115].

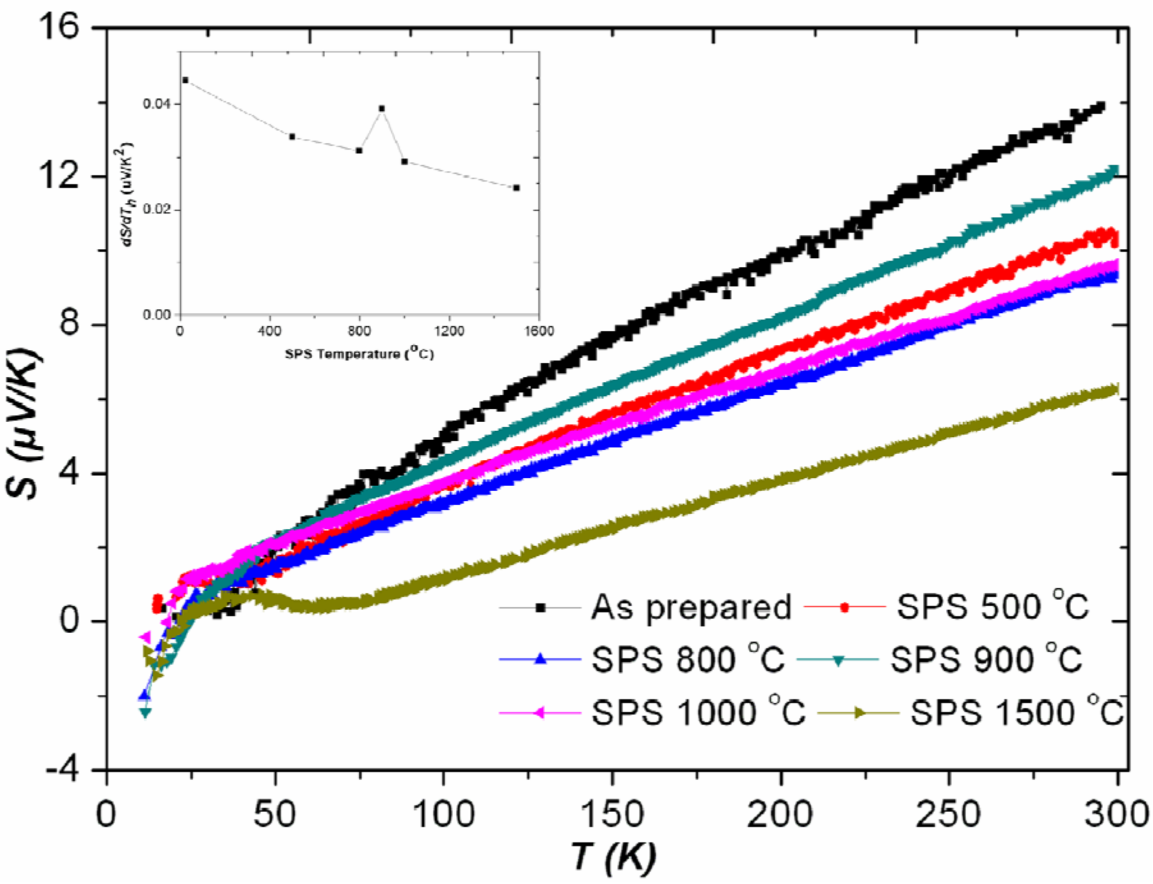

Figure 4.7 *S(T)* for AP, S500, S800, S900, S1000 and S1500 samples. The inset shows the slope of *S(T)* above 100 K for samples sintered at different temperature.

4.4.2 Thermoelectric power

Figure 4.7 depicts *S(T)* for several different samples. There are three important features in these *S(T)* curves: (i) *S(T)* shows a positive sloped linear temperature dependence in most temperature ranges, which reveals the intrinsic metallic properties of MWCNTs; (ii) the magnitude of *S(T)* does not change monotonically with increasing of

T_S, but the slope of $S(T)$ does (except S900), (iii) a small hump appears around 40 K in sample S1500, which is absent in other samples with lower T_S and also a transition from positive to negative S at 20 K is evident for some samples. The following section will focus on these TEP anomalies.

Based on the Mott expression for S due to diffusion (Eqn. 2-19), TEP is related to the energy derivative of σ probed at E_F and is sensitive to the curvature of the bands at E_F. When there is more than one band present, S due to all bands have to be added. We consider the following standard form for the diffusive contribution to S in metal:

$$S_d = DT \tag{4.4}$$

where the constant D is a fitting parameter which depends on the E_F. Our $S(T)$ data exactly follows this expression in high T range (above 100 K). The slope, dS/dT above 100 K, is fitted for MWCNT BPs with different T_S, as shown in inset of Fig. 4.7. dS/dT is increased with SPS temperature (except the S900 sample) which may be related to a change in E_F due to the SPS process.

We attribute the non-linear behavior of $S(T)$ of the S1500 sample to phonon drag effect. Another important feature in S(T) of the S1500 sample is a small negative valley showing up around 15 K. This “S” shape anomaly resembles the one found in kish graphite reported by [100] (also see Chapter 3), except the direction of “S” (the sequence of dip/peak) is different. Interestingly, a plateau appears in $\rho(T)$ of the S1500 sample in the same temperature range where phonon drag appears. It is tempting to explain this plateau as the result of phonon drag effect or the EPC. But we need get more evidence to support this speculation. As the origin of the phonon drag in as-SPSed CNTs, we will discuss this issue further after we present more data in Chapter 5.

For all samples, *S* in high *T* range is positive. The positive sign of *S* for the AP sample is due to the oxygen [72, 78] or the acidic function groups attaching on the wall of the MWCNTs during the purify step [72, 78]. During the SPS process, the oxygen will be degassed, and acidic function groups are vaporized. In as-SPSed samples, new localized acceptor states, due to the defects formed during the SPS process, appear in the valence band, which makes the MWCNT bulk sample a *p*-type conductor. (Chapter 3) The transition of *S(T)* from positive to negative may be due to multi-bands structure in as-SPSed samples as we discussed in Chapter 3.

4.4.3 Thermal conductivity

Fig. 4.8 depicts *κ(T)* of the samples sintered at different T_S. For AP and S900 sample, *κ(T)* is linear at low *T* (~200 K) and then increases quadratically with temperature. This linear behavior of *κ(T)* at low *T* represents the 1-D character of CNTs [117]. On the other hand, *κ(T)* of the S1200 and S1500 samples shows a quadratically temperature dependence at low *T* (~200 K), then roughly linear above 200 K. Generally, because of the large diameter of MWCNTs, the temperature scale for quantum effects should be quite small, and their thermal conductivity of MWCNTs should be that of a 2-D system with linear acoustic phonons. The *κ(T)* of such a 2-D sheet should follow a T^2 temperature dependence [118]. Graphite shows a temperature dependence closer to $T^{2.3}$, because of the effect of quadratically dispersing out-of-plane mode [119]. In our case, when tube-tube interaction is weak (low T_S), $\kappa(T)$ still keeps its 1-D character; when tube-tube interaction is strong (high T_S), $\kappa(T)$ gradually loses its 1-D character and exhibits more 2-D character.

The measured $\kappa(T)$ is mainly from the phonon contribution. Using Wiedemann-Franz law, $\kappa_e \approx \sigma T L_0$, (where L_0 is Lorentz number, ~2.45×10^{-8} $(V/K)^2$), we can calculate the electron contribution for thermal conductivity, which is less than 1% for all the samples over whole temperature range. Fig. 4.8 also show the $\kappa(T)$ from phonon contribution, which is almost overlap with total $\kappa(T)$. Over whole temperature range, $\kappa(T)$ increase monotonically with temperature, and there is no sign of Umklapp scattering (saturate of κ).

Normalized κ with room temperature value of AP sample (κ/κ_{AP}) increases with increasing T_S as shown in Fig. 4.9, in which a linear dependence on T_S of κ/κ_{AP} at room temperature is more or less clear. There is no sign of saturate for κ with increasing T_S which is different from ρ. The maximum of κ at room temperature is around 12 W/(m-K), far below individual nanotube [61]. κ is likely limited by tube-tube junctions.

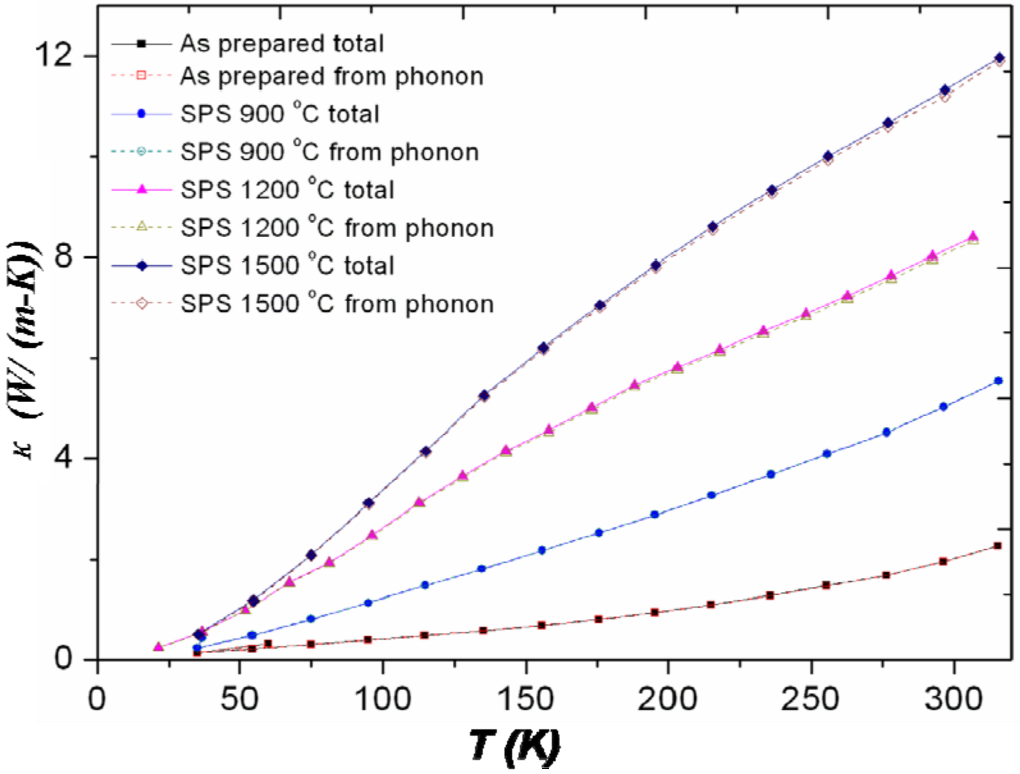

Figure 4.8 *κ(T)* of the BP samples sintered at different T_S. The phonon contribution is deduced using the Wiedemann-Franz law.

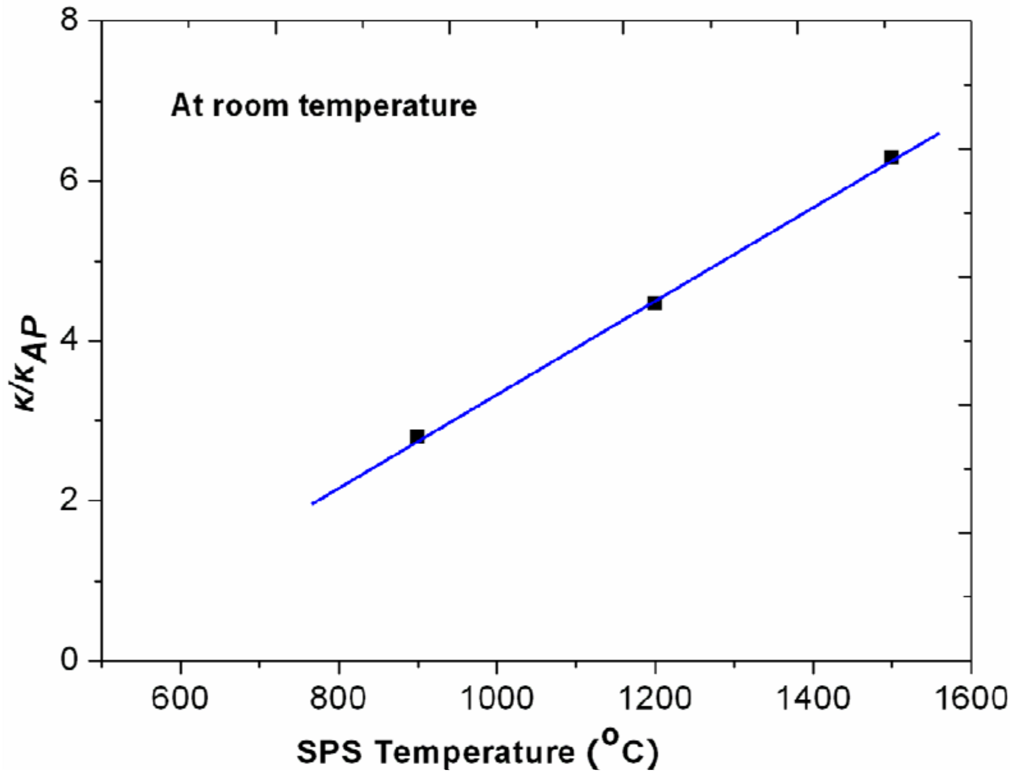

Figure 4.9 Normalized κ with room temperature value of AP sample (κ/κ_{AP}) vs T_S. Solid line is only a guide.

4.5 Conclusion

ρ of CNT networks discussed in this chapter appears to be dominated by the tube-tube junction properties. The SPS process is efficient in lowering ρ by forming inter-tube bonding. T_S dependence of ρ is well described within the framework of percolation theory. At low T, new scattering mechanisms both for electrons and phonon arise due to these inter-tube bindings, for example, an unusual logarithmic temperature dependence of ρ at low *T*, EPC at high SPS temperature, and a transition from 1-D to 2-D in thermal conductivity. Further investigation is needed to clarify these issues. Some of these issues will be addressed in the next chapter. In chapter 5, we will show how dopants affect the transport properties of CNTs. The phonon drag effect in *S(T)* will be further studied in boron doped CNTs.

CHAPTER FIVE
SPARK PLASMA SINTERED BORON DOPED CARBON NANOTUBES

5.1 Introduction

As discussed in chapters 3 and 4, the atomic configuration of the outermost and innermost shells MWCNTs can be dramatically altered in the SPS process: new inter-tube and intra-tube bonding, as well as peeled graphene layers are formed. The salient merit of SPS is the highly localized Joule heating generated in a short time and the very high electrical field. This is because: based on Ohm's law $j = \sigma E$, and when I is large as in the case in SPS j is large, and since σ is low at the junction, it implies that E has to be large. In the as-SPSed MWCNT samples, we observed a strong signature for phonon drag in S (a hump at temperatures between 10 K and 40 K) which is indicative of a strong EPC. Note that EPC is a prerequisite for the formation of Cooper pairs in systems with a low density of carriers [120]. On the other hand, recent work from our group has shown evidence of Meissner effect in B-doped SWCNT film around 12 K [37]. The B-doped SWCNT film was prepared using a pulsed laser deposition (PLD) technique. An immediate question arises as to whether we can dope CNTs with boron, sulfur, nitrogen in a SPS process, and, make it superconducting. In the following, we report some preliminary results along this line.

5.2 Experiments

Two kinds of samples were prepared: One kind is MWCNTs doped with B (B-MWCNTs) while the other one is SWCNTs doped with boron (B-SWCNTs). We adopted slightly different SPS conditions, where a 500 A (400 A) current is used for B-MWCNTs (B-SWCNTs), and the highest temperature recorded was 1400 ^{o}C (1200 ^{o}C).

For B-MWCNTs we used the same MWCNTs as the ones used in Chapter 3. MWNT powder and B_2O_3 powder (atomic ratio, B:C = 3:197)[6] are simply mixed using mechanical grinding before put into graphite die as depicted in Fig. 3.3a. No purification steps were employed. About 7 MPa pressure was applied to keep good contact between electrodes and the B_2O_3/MWNT admixture, and a maximum 500 A current was applied (on a 0.5” graphite die) to attain a temperature of 1400 ^{o}C. The mixture was held at that temperature for 5 minutes. Then the system was allowed to cool down to room temperature.

For B-SWCNTs, to get more uniform mixture of boron compound and CNTs, we used H_3BO_3 instead of B_2O_3 because H_3BO_3 can be dissolved in ethanol. H_3BO_3 and SWCNTs in various atomic ratios of boron/carbon were dissolved in ethanol and sonicated for 2 h. (for example, for the sample of SWNT doped with 5 at% B [7] about 83.1 mg H_3BO_3 and 300 mg SWNT were suspended in ethanol (about 20 ml). Then the solution was heated at 70 ^{o}C overnight and the ethanol was evaporated. We prepared 5 B-SWCNT samples with different boron atomic ratio from 5% to 15% with a step of 2.5%. The as-prepared SWNTs (purity ~ 70%) used here were synthesized by the electric arc method using the standard Ni/Y formulation. No purification steps were employed.

Raman spectroscopy (with excitation wavelength = 514.5 nm) was used to characterize the structural changes of B doped CNTs. Electrical transport measurements,

---

[6] We just test one sample for B-MWCNTs, which is just a test sample, we are more concerned on B-SWCNTs.

[7] In this Chapter, doping ratio of B is just nominal ratio. So far we have no efficient way to figure out how many B atoms get into the carbon hexagonal network of CNTs.

similar to those given in Chapters 3&4, were done to examine the changes of electric transport property due to the dopants in CNTs network.

5.3 Results and discussion

5.31 Raman spectrum

In layered sp^2 carbon nano-systems, it is possible to tailor the electronic, vibrational, chemical and mechanical properties by introducing either non-carbon atoms or molecules and compounds in different manners at small concentrations. We define this phenomenon as doping. There are three main doping categories: a) exohedral doping or intercalation, b) endohedral doping or encapsulation and c) in-plane or substitutional doping [121]. Raman characterization is an important technique for characterizing both undoped and doped CNTs. The dopant-induced interactions with the sidewall of a nanotube will perturb the Fermi level of the nanotube through charge transfer interactions. Since electrons and phonons are strongly coupled to each other in resonance Raman spectroscopy, these perturbations will influence the various Raman modes present in CNTs. Different doping categories will influence Raman modes in different ways [121].

For the B-MWCNT sample, there is no discernable change in Raman modes (reference Fig. 3.5) between the pristine and B doped as-SPSed MWCNT samples. This probably is due to the mild B concentration. For B-SWCNT samples, There is a barely discernable change for the radial breathing mode (RBM, 165 cm^{-1}), D-band (1355 cm^{-1}) and G-band (1593 cm^{-1}) in intensity and frequency (Fig. 5.1a). But a non-linear variation in the G'-band (or D* band) frequency and FWHM is nonetheless clearly evident (Fig 5.1b). This probably means that SWCNTs are exohedrally or endohedrally doped by B atoms or some functional chemical group such as, the $H_2B_2O_3^-$ group or so on. There is, if anything, a very tiny amount of substitutional doping in our B-SWCNTs.[8] The non-linear variation in the G'-band resembles the results reported by P. M. Rafailov, et al. [122]. In their work, the electrochemical doping method was used to control the doping level in SWCNT mats, which were used as working electrodes. They found the frequency of the G'-band is sensitive to the doping level and laser excitation. They attributed this phenomenon to a second Kohn anomaly (KA) in metallic SWCNTs, located in the K-point-derived region of the BZ, which stems from the KA at the K-point of graphene. We have not examined the relation between frequency of G'-band and laser excitation. But we hope to get more information about the KA from electrical transport measurements.

---

[8] Large amount of substitutional doping will cause the giant increase in intensity of the D-band upon boron doping.

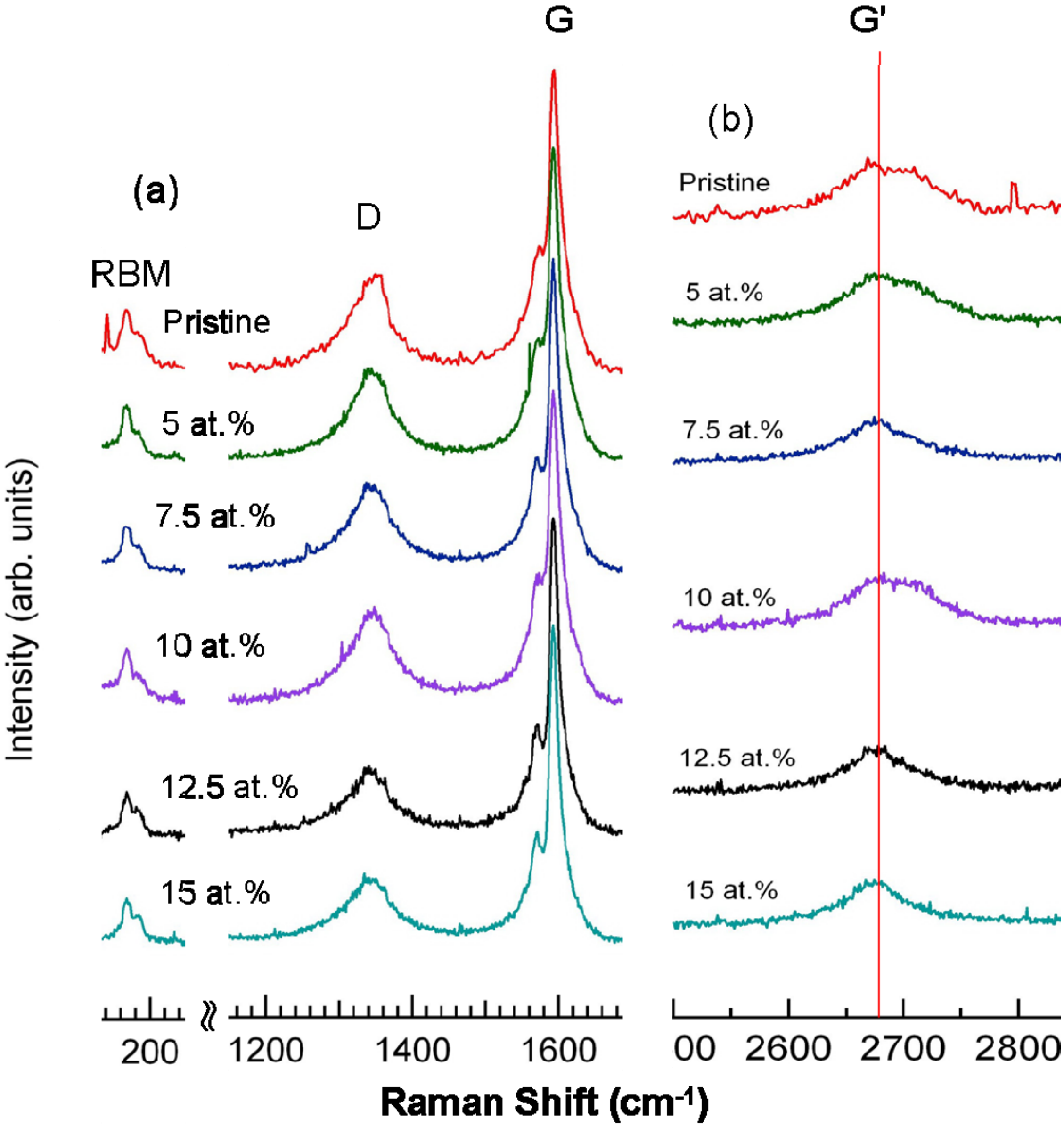

Figure 5.1 Preliminary Raman spectra of (a) the RBM, D-band, G-band and (b) the G' band for as-SPSed B-SWCNTs. The red line in (b) is guide to the eye.

5.3.2 Electrical conduction

(i) B-MWCNTs:

Figure 5.2 shows the temperature dependence of both TEP and resistivity. TEP is a good gauge of the Fermi surface topology, so the temperature dependence of *S(T)* is an indicator of band structure change (e.g., due to doping). *S(T)* decreases monotonically with decreasing temperature. At high temperature (above 100 K), the *S(T)* curve basically shows a linear relationship with *T*, which implies that the sample exhibits metallic character. But at low *T* (below 100 K), a nonlinear behavior sets in. An almost "S" shape curve can be clearly seen in the temperature range 10-100 K. In the inset of Fig. 5.2, the first order derivative of *S(T)* is plotted after smoothing the data to show the "S" feature more prominently. To explain this "S" shaped feature, we compared our results to those reported by J. Vavro, et al. [78]. In their work, a slope change at a characteristic temperature (T_0) was observed in the p-doped SWCNT films with acid. J. Vavro et al. attributed this unusual behavior to 1-D phonon drag, in which the depression of the Fermi energy by dopants cuts off electron-phonon scattering at temperatures below the T_0. Essentially we get similar results as they got, except that we observed another dip around 50 K. We also attribute our "S" shaped feature to the phonon drag effect. Upon subjecting as-prepared CNTs to the SPS process, the CNTs are "welded" together at junction points, in which case whether the as-SPSed samples can be treated as 1-D materials is questionable (Chapter 4). Also a 1-D phonon drag mechanism cannot explain the dip appearing at 50 K. The "S" shape anomalies are usually found in high crystallinity graphite [100-101], which suggests that as-SPSed MWCNTs may have same scattering mechanism as graphite's. Another important feature of our *S(T)* data is that *S* is positive in the entire temperature range. These results provide further evidence that our MWCNT samples are doped with Boron since the pristine MWCNT is n-type [72, 75]. Furthermore, it must be noted from Fig. 3.7 (c) that in pristine MWCNTs, *S* changes from positive to negative values at low temperatures, which is absent in our boron doped MWCNT sample.

The *ρ(T)* data for the SPS-ed Boron-doped MWCNT sample shows a nonmetallic behavior in the entire temperature range (Fig. 5.2) and it increases monotonically with decreasing temperature. However, one noteworthy feature in the data is the plateau which appears in the region 25-50 K, which coincides with where we find the phonon drag effect in S(T) curve. This resembles *ρ(T)* of as-SPSed MWCNT BP (Chapter3). So, we have reasons to believe this plateau is caused by EPC (the phonon drag effect). In any case except for the superconductivity, the EPC does not lower the resistivity, i.e., any electron-phonon scattering mechanism only increases the resistivity. The plateau in *ρ(T)* maybe be the sign of the onset of superconductivity that is mediated by the same EPCs as ones seen in the phonon drag (of the normal state electrons). Let us suppose boron doped MWCNTs have two domains, one superconductor, and the other one normal as shown in Fig. 5.3. The major contribution to *ρ(T)* comes from the normal state or that of the pristine as-SPSed MWCNTs. Note that for a pristine as-SPSed MWCNT, *ρ* increases dramatically around 10 K. We believe that SC domains are the minority phase in the sample and *ρ* of the sample is dominated by *ρ* of the host (similar to SPS-ed pristine MWCNTs), and there *ρ* in SPS-ed Boron-doped MWCNTs does not drop to zero at low T.

This is also the reason why the slope change of *ρ*(*T*) for B-MWCNT increases again ~15 K. M. Matsudaira et al. found Meissner effect in boron doped SWCNTs. When they deposited several contact pads on the sample and tried to measure *ρ(T)*, superconductivity was only measured across some contact pads since the sample contained a non-uniform distribution of SC domains (Fig. 5.4). Their results further support what we proposed. There is another possible explanation for the plateau in *ρ(T)* in Fig.5.2. The phonon drag has a characteristic temperature, where the coupling between electrons and phonons are maximized, the effects gets weaker when it is away from that range and EPC lowers the resistivity. But this explanation meets difficulty when multi phonon drags appear in *S(T*), which is evident in B-SWCNT.

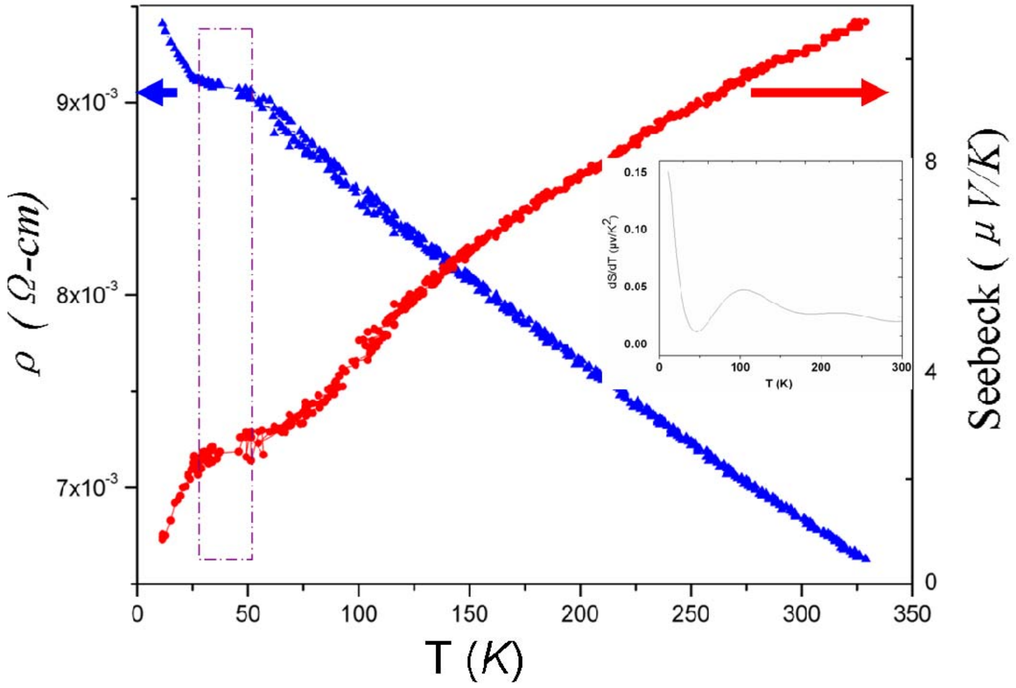

Figure 5.2 *ρ(T)* (left) and *S(T)* (right) for B-MWCNT. The violet dashed line outlines the temperature region where the possible signature of superconducting and phonon drag are evident. The inset is the dS/dT curve which show a peak at around 100 K and a dip around 50 K.

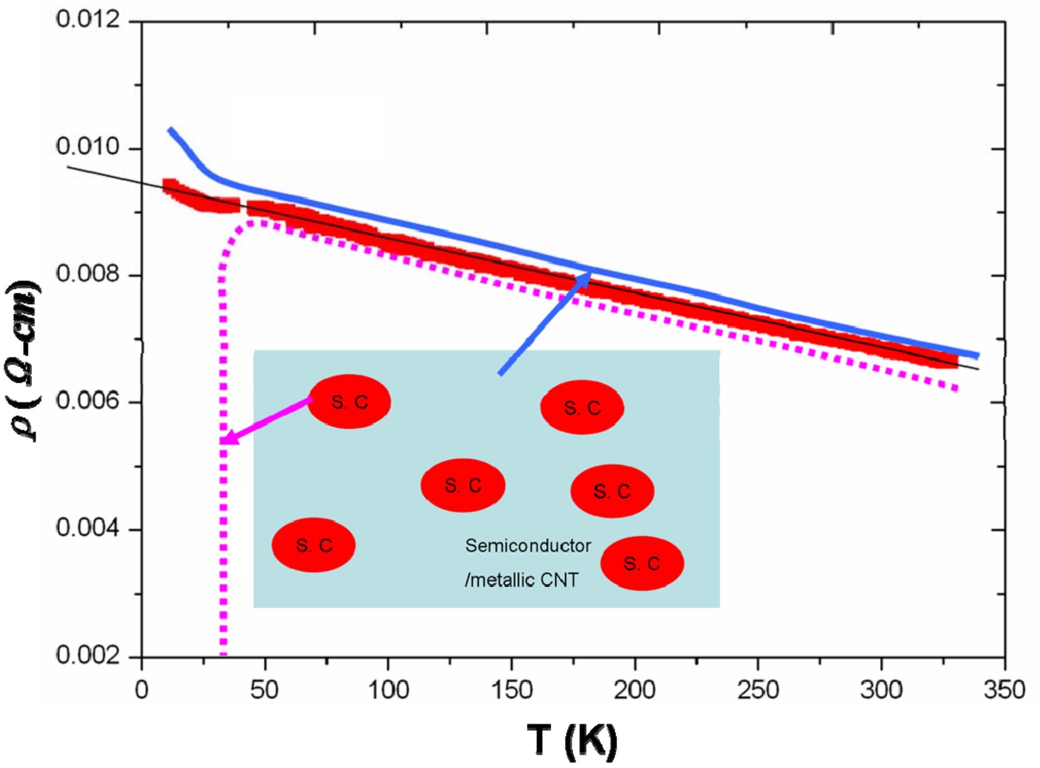

Figure 5.3 Deconvolution of *ρ(T)* as (a) normal $\rho_N(T)$ curve which is typical for SPS-ed pristine MWCNTs (Fig. 4a), and (b) $\rho_{SC}(T)$ curve. The black solid line is a guide for the eye. The inset is schematic illustration of the composition of B-MWCNT. We believe that superconducting domains (Circles with S.C) are non-uniformly embedded in a

semiconducting/metallic matrix of MWCNTs. There is no complete percolation path between the S.C domains.

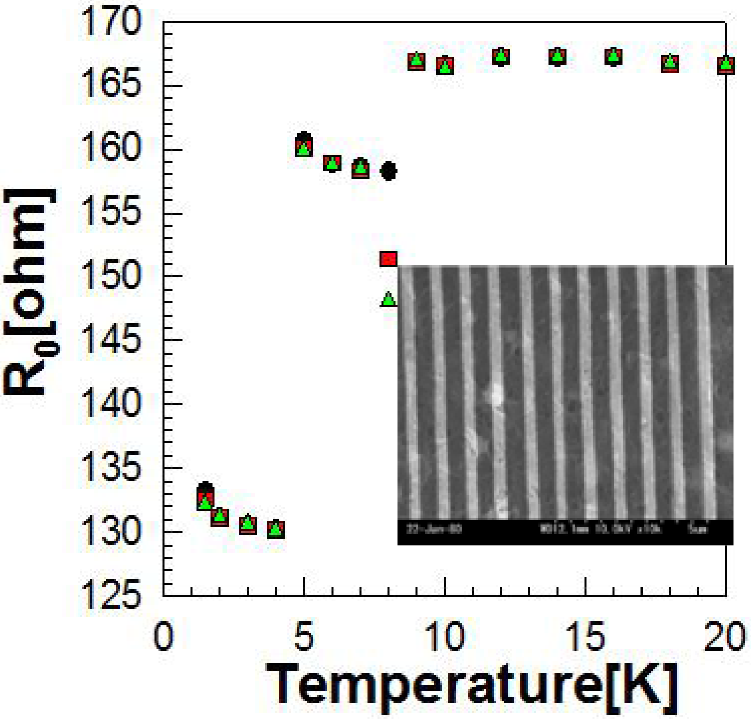

Fig. 5.4 Resistance was measured on boron doped SWCNT thin film three times at each temperature and noted by different symbols. Inset is SEM top view of Au/Ti electrode pattern fabricated on the film. In order to detect a very small superconducting area, many source and drain electrode fingers were patterned within 300 nm spacing [123].

(ii) B-SWCNT:

The following discussions are mainly on the sample of 7.5 at.% B doped SWCNTs (B-SWCNTs). Fig. 5.5 depicts the temperature dependence of normalized $\rho(T)$ ($\rho_0=\rho/\rho_{150K}$). $\rho_0(T)$ show a temperature dependence similar to B-MWCNTs. A plateau is evident around 50 K which is at same temperature range as B-MWCNTs. We also measured the resistivity with different currents from 2 mA to 100 mA. Above 50 K, $\rho_0(T)$ shows a similar temperature dependence. But at low temperature, $\rho_0(T)$ shows the current dependence behavior, which is depicted in the inset of Fig. 5.5 at 11 K[9]. For a 1-D superconductor, due to the strong electron-electron interaction, T_C depends on the current such that T_C increases when a small current is applied. But in our case, we don't observe any change in the position of the plateau in Fig 5.5.

In general, the atomic vibrations are partially screened by electrons. In a metal this screening can change rapidly for vibrations associated with certain **q** points of the BZ, determined by the shape of the Fermi surface [124]. Kohn anomalies (KA) may occur only for **q** such that there are two electronic states $\mathbf{k_1}$ and $\mathbf{k_2} = \mathbf{k_1} + \mathbf{q}$ both on the Fermi surface, line or points [124]. This implies that **q** spans the Fermi line in a 2-D material or the Fermi points in a 1-D material. The coupling strength of this phonon to the electronic system is usually governed by the position of the Fermi level E_F. Especially, for the half-filled linear bands of graphene and metallic SWNTs, the EPC strength is at maximum when the Fermi level is located at the band crossing point. Shifting the Fermi level away from this crossing point strongly decreases the energy due to the lattice distortion. Both

---

[9] During the resistivity measurement, the data became a little bit noisy when the current is small. So there are large uncertainty for the data took with current smaller than 10 mA.

theoretical and experimental work has shown the existence of a KA in graphite and SWCNTs [122, 124-125]. The current dependence of $\rho_0(T)$ implies the dependence of the EPC strength on current at low temperature (Fig.5.5). This resembles the KA. In our case, Fermi level of the sample is tuning by current density, which in turn changes the strength of EPC. Similar experiment is also done in B-MWCNTs, but there is barely discernable difference in $\rho(T)$ comparing 100 mA run with 25 mA run (Fig. 5.6a). This probably means that KA in MWCNTs is not as strong as SWCNTs. The *S* data for both samples support this argument: phonon drag in B-MWCNTs just causes small slope change, but for B-SWCNTs, a peak in $S(T)$ is nonetheless clear at T ~50 K (Fig.5.2 and 5.7).

As we discussed above, large current density can shift the Fermi level from its original position, which suppresses the strength of the EPC. In another words, EPC is the strongest when no current or little current passes through the sample, where the Fermi level is at band crossing point. If that is true, then we should expect to see an exceptionally small magnitude of *S* due to the electron-hole symmetry in SWCNTs [76]. Figure 5.7 supports this argument.[10]. *S* is smaller than 1 μV/K above 60 K. In the literature, *S* of SWCNTs usually is around 50 μV/K at room temperature no matter if the nanotubes are isolated tubes or in bundles [62, 70, 72, 74].A phonon drag peak is evident around ~50 K. TEP of B-SWCNTs is positive above 20 K, which means holes are dominant carrier in this temperature range. A transition from positive to negative appears at 20 K. It is reasonable to assume there is at least another dip below 10 K based on the 3rd law of thermodynamics. This "S" shape phonon drag can be well explained by the

---

[10] We measure TEP in open circuit. So there is no current dependence of TEP.

theory proposed by J. P. Jay-Gerin [101]. We also observed the KA effect at exact same temperature range where phonon drag is presented, which strongly supports that theory.

We show that the KA can be used to explain what we observed in our as-SPSed samples very well. But there are also some other scattering mechanism which we have to consider, such as electron backward scatting, energetic barriers at tube junctions, the Kondo effect (there is Ni catalyst in the samples) and charge density wave. R. Klesse [126] showed that for typically doped CNTs backward scattering at dopants is the dominating effect. If it is true in our sample, then we should observe *ρ(T)* decrease with increasing of electrical current over the whole temperature range, because charge density oscillations present near defects are tunable by varying the applied bias potential. In B-SWCNTs, *ρ(T)* is independent of the current above 50 K as shown in Fig. 5.6b, which implies the electron scattering is not the dominating scattering mechanism in our B-SWCNTs. Also our *ρ(T)* is strongly correlated with *S(T)*. It is possible that the electric field helps electrons overcome the energetic barriers at junctions. Again, we observe the resistivity difference only below 50 K no matter what current passes through. If the energetic barriers are dominating scattering mechanism, 50 K must be a critical temperature point. And also, there should be energetic barriers in B-MWCNTs too, which barely show current dependence. There it is difficult to explain our *S(T)* data using the Kondo effect. We have to admit that we have no way to rule out the possibility of charge density wave in B-SWCNTs in present stage. Other experimental tools have to be employed to clarify this issue.

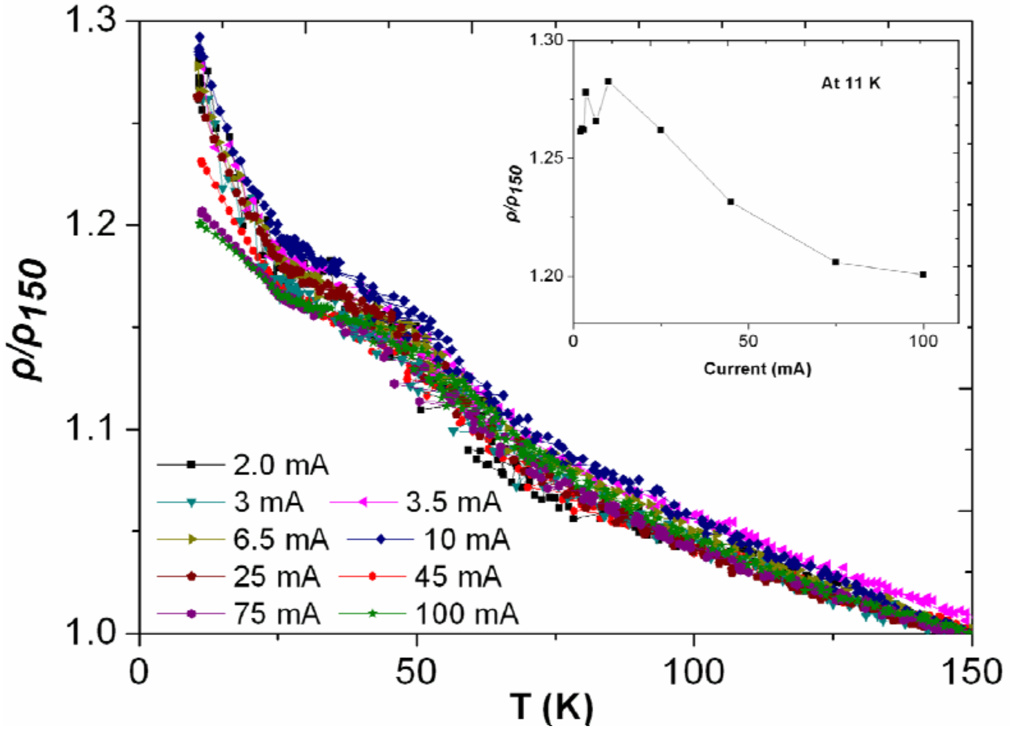

Figure 5.5 Temperature dependence of $\rho_0 = \rho/\rho_{150}$ of B-SWCNTs under different electrical currents. The inset shows a current dependence of normalized ρ_0 at 11 K.

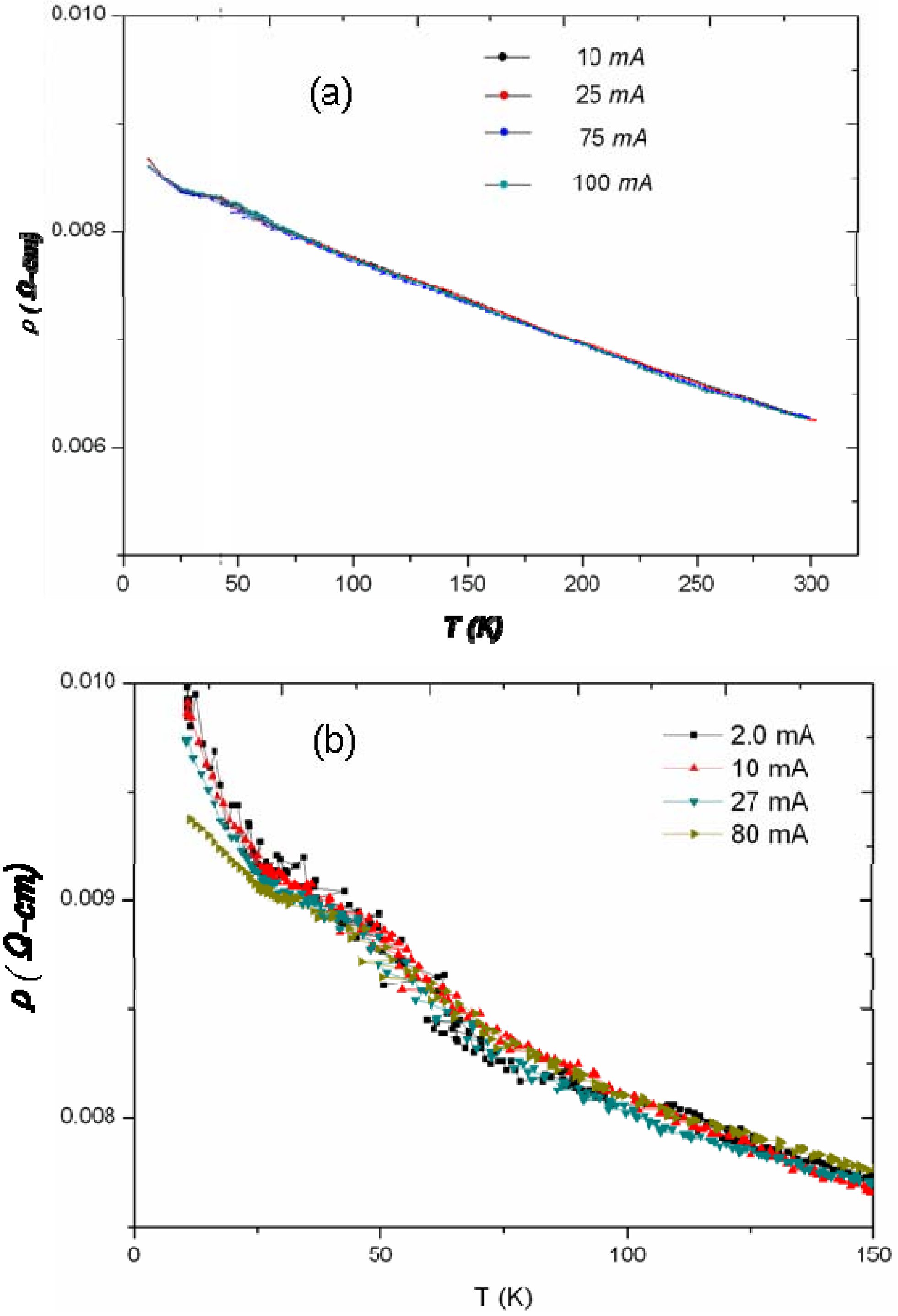

Figure 5.6 *ρ(T)* of (a) B-MWCNT and (b) B- SWCNT under different currents.

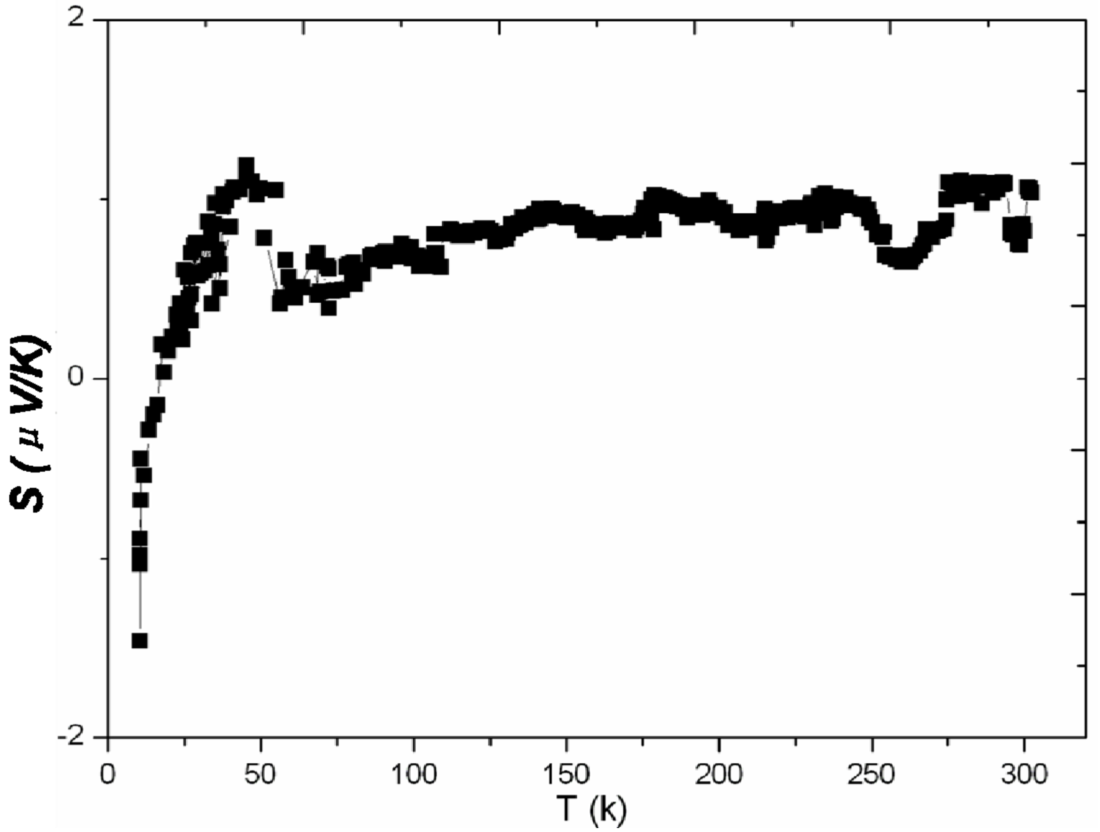

Figure 5.7 *S(T)* of B-SWCNT.

5.3.3 Possible Meissner effect

For a superconductor, not only the resistance is zero, the system also becomes a perfect diamagnetic below the superconducting transition temperature, T_C. Magnetization measurements of both B-MWCNTs and B-SWCNTs were performed using a superconducting quantum interference device (SQUID). This work was done at University of Texas at Dallas. Figure 5.8a shows magnetic susceptibility of B-SWCNTs as a function of the magnetic field. The material is ferromagnetic both at 5 K and 295 K which implies a large amount of ferromagnetic catalyst is present in the sample. The temperature dependence of the magnetic susceptibility is also shown in Fig. 5.8b. An abrupt drop of magnetic susceptibility is evident at ~ 20 K as well as an anomaly at ~50 K. With the increasing of magnetic field, the drop disappears eventually at 2000 Oe. This probably is due to superconductivity. But we can not rule out the contribution from the ferromagnetic catalyst. It is hard to discern a weak signal from a minor superconducting phase in the presence of a FM background from the catalysts. Doping CNTs without a magnetic catalyst using the SPS process is our next mission. We also obtained similar results in B-MWCNTs, as shown in Fig. 5.8 (c) and (d).

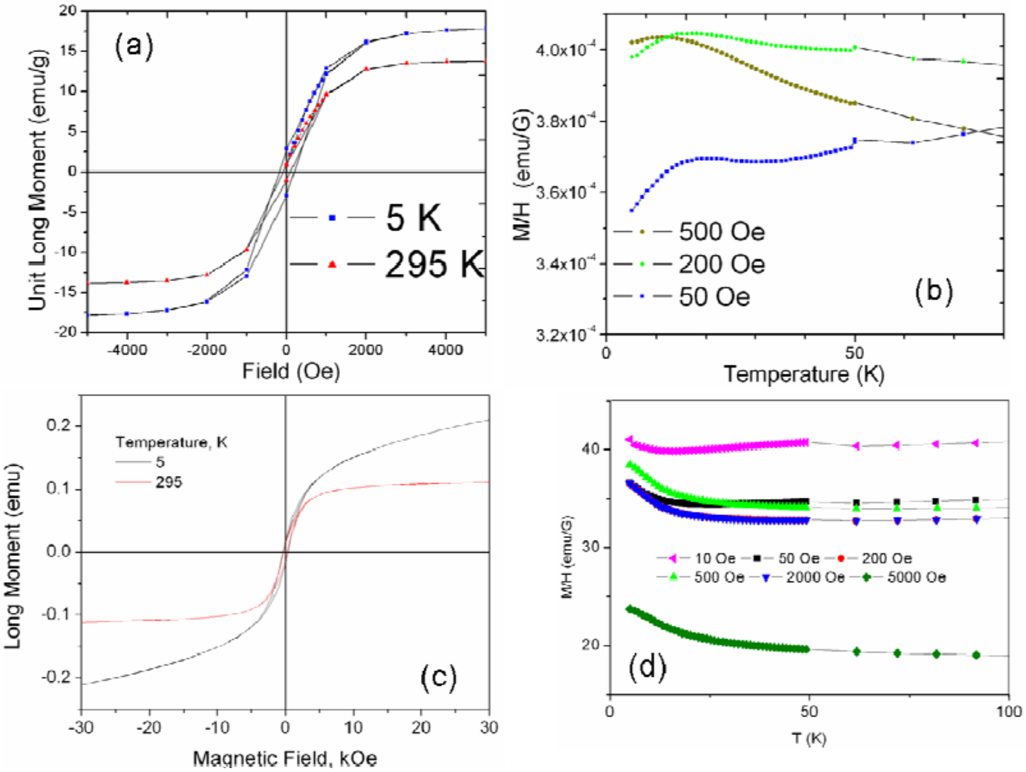

Figure 5.8 Magnetization measurements on B-MWCNTs and B-SWCNTs. (a) and (c), magnetic susceptibility as a function of magnetic field for B-SWCNTs and B-MWCNTs respectively; (b) and (d), magnetic susceptibility as a function of temperature for B-SWCNTs and B-MWCNTs respectively (All the measurements are done under zero field cool).

5.4 Conclusion

In this chapter, we mainly examined the electrical transport properties of B doped CNTs. We tested two ways to mix B compounds with CNTs powder: grind mixing and solution soaking. Raman spectrum shows that CNTs are doped with B during the SPS process, which dramatically changes the electrical properties of the CNTs. In both samples, B-MWCNTs and B-SWCNTs, a plateau appears at around 50 K in $\rho(T)$. This plateau maybe is due to parts of B-CNTs becoming superconducting at that temperature. For B-SWCNTs, we find that the resistivity is current dependence at low T, which we attribute to the KA. The phonon drag effect is evident in both samples in the same temperature range where the plateau presents in $\rho(T)$. We believe the coupling between electrons and Kohn phonons causes the phonon drag in as-SPSed CNTs. We also observed an abrupt drop in magnetic susceptibility at around 25 K during magnetization measurements. But due to the strong background from the magnetic catalyst, we don't have a clear evidence for the Meissner effect in our as-SPSed samples.

So far we have shown that how we strengthen the tube-tube interaction and potentially introduce defects into the carbon network. In the following chapter, we will examine the role of intra-tube defects which lead to different morphology of CNTs, for example, helically coiled CNTs, which may is posited to contain periodically inserted pentagon/heptagon defects.

CHAPTER SIX

HELICALLY COILED CARBON MATERIAL

6.1 Introduction

Helically coiled carbon nanotubes (HCNTs) and nanowires (HCNWs) represent novel nanostructural morphology and have technological and scientific significance (We distinguish HCNTs from HCNWs in that the former comprise parallel walls with a clearly distinguishable core while the latter are solid structures without a core. We use nanocoils to represent both HCNTs and HCNWs). Their potential applications [127] span high frequency electronics [128], tactile and magnetic sensors [129], and structural foams for cushioning and energy dissipation [130-131]. It is also interesting to make a connection between chemical vapor deposition (CVD) synthesized helical carbon nanostructures to organic forms found in nature such as DNA and proteins, and indeed, these structures can be used for templates in collagen growth [132]. It was also suggested that a HCNT could correspond [118] to a sequence of alternating metallic/semiconducting junctions, which is very interesting from the point of view of application to nanoelectronic systems[133-134].

The HCNTs were first predicted to exist in the early 1990s by Ihara et al. and Dunlap [7, 135]. These CNTs are created when paired pentagon-heptagon (PH) atomic rings arrange themselves periodically within the hexagonal carbon network. Theoretical calculations also predicted that various forms of helically coiled structures are possible and those structures are energetically and thermodynamically stable. The first experimentally observation of a HCNT was in 1994 by Zhang et al. [136]. Since then, several groups reported on the synthesis of coiled nanostructures using the CVD method. Table 6-1 lists all kinds of catalysts, methods, substrates, and carbon sources which have been used to synthesize HCNTs and HCNWs. All of these listed methods can be put into three categories based on what substrates they used: supported CVD growth, substrate CVD growth, and template CVD growth [137]. The drawbacks of the supported CVD synthesis of coiled CNT are: (1) the obtained coils have only been by-products of MWCNTs; (2) the manufacturing of coiled nanotubes has not realized large-scale production for industrial and device applications, as has that of straight CNTs; (3) coil growth is difficult to control precisely via CVD process conditions and catalyst features. For template CVD growth, it is typically found that such methods, in addition to limiting the amount of material due to the catalyst distribution, is often accompanied by the formation of straight MWCNTs. Most substrate CVD growth methods have to use catalyst patterned substrates, which also restricts the application in industry. It would be desirable to develop a process that is independent of the underlying substrate, utilizing gas-phase synthesis alone [138].

For applications, it would be desirable to have control over the coil morphology and geometry. This has not been achieved, possibly due to an incomplete understanding of their growth mechanisms. Several models have been proposed to understand their synthesis. But none of these models make any predictions, nor give specific reasons for helical growth, maintaining that “rather special conditions”[139] would be needed for coiling. A comprehensive and fundamental explanation for HCNT/HCNW synthesis in terms of a unified model is desirable.

Table 1 Literature reports in synthesis of HCNT/HCNW

Catalyst	Carbon Source	Substrate	Method	Reference
Co	Acetylene	Silica (supported)	CVD	[136], [87], [58], [1]
Co	Benzene	SiO_2 (supported)	CVD	[140]
Lanthanide oxide	Acetylene	$AlPO_4$-5	CVD	[141]
Iron phthalocyanine	Insufficient of Carbon source	Various substrate	CVD	[142]
Fe	Kerosene, Methane	---	CVD	[143]
Co	Methane	Al_2O_3 (supported)	CVD	[144]
Fe, Ni,	Acetylene	Magnesium Carbonate/ Silica/ zeolite (supported)	Micro-wave CVD	[145]
Ni	Acetylene/ PCl_3	Graphite plate	CVD	[146]
Co, Ni	Melamine	Patterned catalytic silica	CVD	[147]
Fe, Sn, In	Acetylene	ITO glass	CVD	[148], [149]
$Fe(CO)_5$	Pyridine or Toluene	Silicon, quartz	CVD	[150], [151]
Ni,[11]	Acetylene/ Ammonia	Ni/Silicon	dc plasma enhanced CVD	[152]
Cu	Ethylene	Silicon	Hot filament CVD	[153]
Co/Ge	Acetylene	Ge wafer	CVD	[154]
Fe, CO, Ni sulfate	Acetylene	Porous aluminum oxide template	CVD	[155]
Fe	----	Straight CNT as template	Microwave plasma enhanced CVD	[156]
Fe, Sn, In	Acetylene	Bare quartz substrate	CVD	[90]

---

[11] Zigzag shaped CNT with small radii of curvature. Electric filed was applied to manipulate the direction of CNT.

In this section, a liquid-precursor-based synthesis method is introduced. With this method, either HCNTs or HCNWs, with differing electrical and mechanical properties, [131, 134, 148, 157] can be fabricated. We provide a rational explanation for the distinct growth modes based on an analysis of the binary equilibrium phase diagrams, where the mutural affinity of secondary catalysts (In/Sn), with the primary catalyst (Fe) in the ferrocene-xylene mixture, promotes nanotube/-wire formation. We also introduce a thermodynamic model, base on exclusion volume principles, common in chemical and biological systems, [158] that could potentially explain coiling in nanostructures. We make specific predictions for the optimal growth of HCNT/HCNW with the hope that these could be used as a guide for rational synthesis. Finally, our own experimental results conform the above model on the role of In/Sn catalyst particles in influencing the coil pitch in HCNT/HCNW.

6.2 Rational synthesis of HCNT/HCNW and Electron microscopy characterization

High purity HCNTs in bulk are synthesized using a CVD system similar to that depicted in Chapter 3. Ferrocene and Indium isopropoxide (from Alfa-Aesar) are used as catalysts. Briefly, indium isoporpoxide is individually dissolved in a xylene-ferrocene mixture as a liquid precursor, and the ratio of C:Fe:In was maintained at 99:0.25:0.75. The mixture is injected into the CVD reaction tube at ~1.5 ml/hour while maintain the preheator and main furnace at 200 and 700 ^{o}C, respectively. Simultaneously, acetylene along with Argon carrier gas is passed through the chamber, at atmospheric pressure. Parameters such as the reactor temperature, gas flow rate, relative concentrations of In or

Sn with respect to Fe were investigated and adjusted for optimal synthesis (Ref. Fig. 3.2). Subsequently, after ~1 h of reaction time, the quartz substrates and the inner walls of the quartz tube inside the furnace were densely coated with soot-containing HCNT arrays.

The synthesis conditions for the HCNWs are similar to those described for the HCNTs except that Sn, in the form of tin isopropoxdie, is used, the ratio of C:Fe:Sn is maintained at 99:0.8:0.2, and a slower injection rate (1.0 ml/hour) is used. Approximately 100 mg of these coiled nanostructures could be prepared in a 1 h run. The as-prepared HCNTs and HCNWs were pure with very little presence of amorphous nanoparticles.

SEM and TEM are performed for structural and morphological characterization. HCNTs are formed in self-aligned arrays on quartz substrates. We can peel off the HCNTs from the substrates (Fig. 6.1a), which can then be assembled onto a substrate of choice. A closer examination reveals the uniformity of the coiling and pitch (Fig. 6.1b) through the length of the HCNT. TEM imaging reveals that the array is comprised of HCNTs of smaller diameter (Fig. 6.1c). The constituent tube diameters are quite uniform in the 15-25 nm range, with a pitch ~1 μm. HRTEM images show that HCNTs have good crystalininty.

Unlike the HCNTs, the HCNWs are found to be randomly oriented on the substrates. Figure 6.2a illustrates the general appearance of as-prepared HCNWs. A broader diameter distribution, in the 10-300 nm range, is observed. In several HCNWs, catalyst nanoparticles are discerned at the tips (Fig. 6.2b, c).

To exploit the role of catalysts in synthesis of nano coils (both HCNT and HCNW), Energy Dispersive Spectroscopy (EDS) has been used to identify the elements and their location in the nanocoils. Even though large quantity indium is used during synthesis, we find no trace of indium along HCNTs. Instead, iron nano particles are randomly distributed along HCNTs (Fig. 6.3). Using a similar procedure, we characterize the tip particle of the HCNW, where elemental mapping reveals the tip is mainly composed of C, Fe, and Sn (Fig. 6.4). Preliminary Cliff-Lorimer analysis reveals an Fe and Sn ratio of 4:1, consistent with the atomic ratios of the elements in the chemical precursors (Fe: Sn:: 0.78: 0.22)..

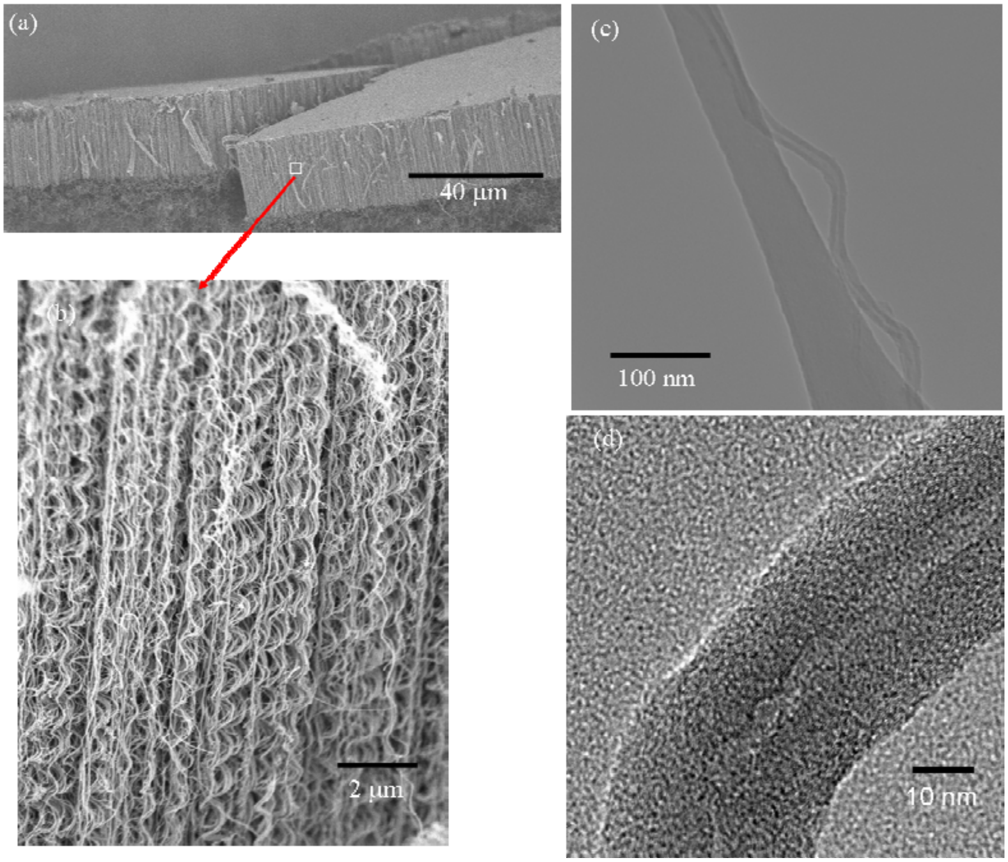

Fig. 6.1 Electron microscopy images of HCNTs. a) A typical SEM image of an as-grown HCNT array, prepared through the use of In catalyst, subsequent to peeling off from the quartz substrate. b) Highly aligned HCNTs with nearly identical diameter and pitch. c) Low magnification TEM images. d) HRTEM images of a HCNT.

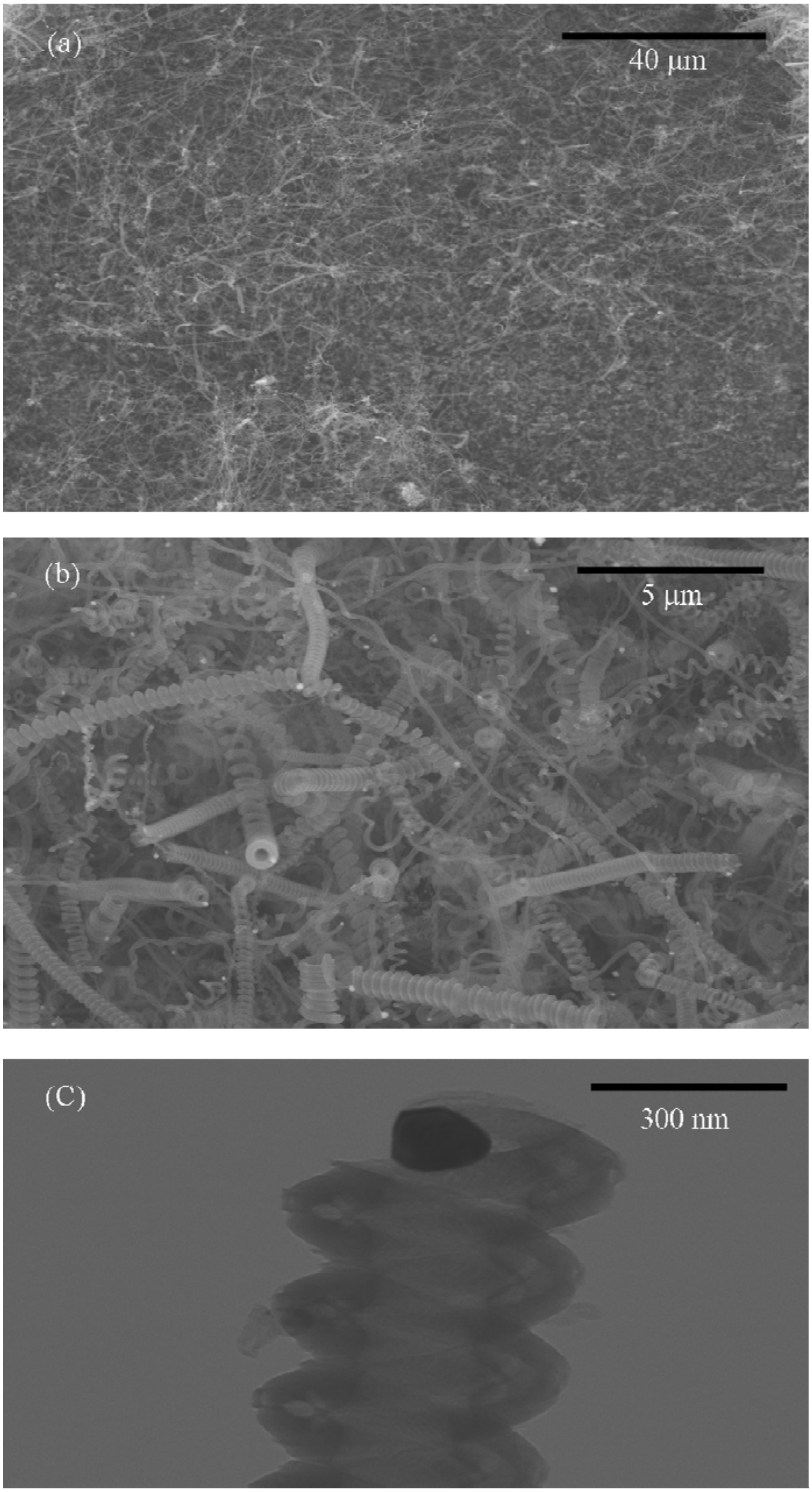
(a)
40 μm
(b)
5 μm
(C)
300 nm

Fig. 6.2 Electron microscopy images of HCNWs. a) SEM image for as prepared HCNWs through Sn catalyst mediated synthesis. b) A representative SEM image illustrating HCNWs of differing diameter and pitch. c) TEM image of an individual HCNW, illustrating the position of Fe-Sn nanoparticle, at tip.

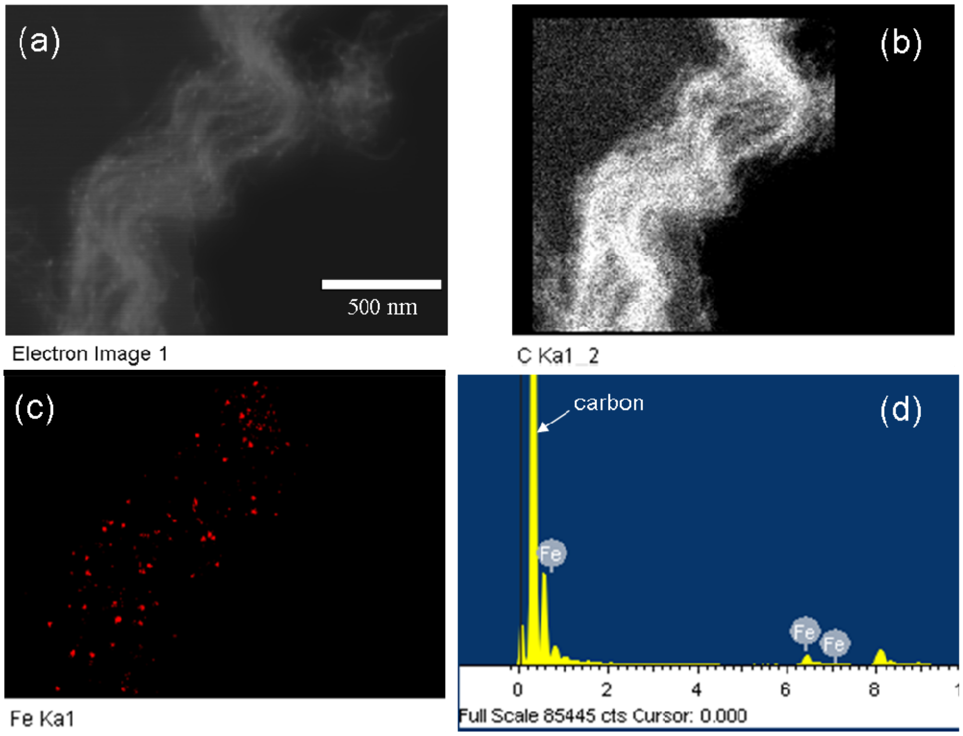

Fig.6.3 EDS mapping of the a) HCNT bundle in dark field microscope, shows the elemental distribution of Carbon (b) and Iron (c). d) EDS spectrum of the HCNT bundle. The unidentified peaks are from background.

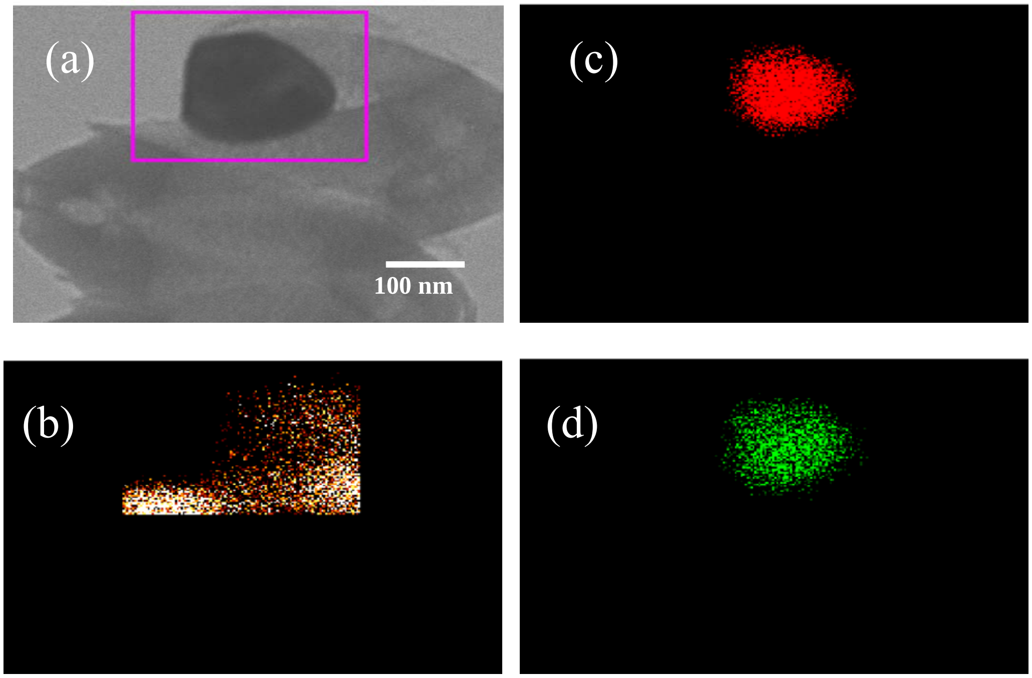

Fig. 6.4 EDS mapping of the (a) HCNW and the tip nanoparticle, show the elemental distribution of (b) Carbon (c) Iron (d) Tin .

6.3 Growth mechanism for HCNT and HCNW

6.3.1 Existing Growth mechanism for HCNT and HCNW

Theoretical work has been done to show that when a pentagon or heptagon pair join a graphitic sheet, the strain associated with this defect will be localized, and positive curvature (caused by the pentagon ring) and the negative curvature (caused by the heptagon ring, (shown in Fig. 6.5 [1]) will be generated. Thus in principle, HCNTs can be constructed by periodically inserting pentagon and heptagon pairs in to hexagon background (Fig. 6.5), which also happens to be energetically and thermodynamically stable [7]. Lu et al. proposed a growth mechanism for HCNTs based on this concept of incorporating pentagons and heptagons in the hexagonal tubular lattice. They believed that during the synthesis, pentagonal/heptagonal carbon rings are created in the graphite lattice, which change the direction of growth and introduce curvature. The growth of HCNT is determined by the creation rate of the periodic production of pentagon-heptagon-pair (P-H pairs) dislocations in diametrically opposite parts of the tube. It has been found that it is necessary, based on theory and geometric considerations, to introduce P-H pairs at the bends to account for the curvature for SWCNTs.

The most widely accepted models for HCNTs are then related to (a) the anisotropic rates of carbon deposition and/or (b) nature and geometry of the catalyst particle. Motojima et al.[159] [160] proposed a anisotropy of carbon deposition theory. In that theory, carbon atoms are obtained through the acetylene decomposition reaction, immediately dissolved into the catalyst grain, and eventually condensed from different crystal planes of the catalyst during the growth of carbon fiber. The capability of carbon deposition and condensation, however, is not the same for all the crystal planes. Assume a fiber grows out of three contiguous crystal planes, (1,0,0), (0,1,0), and (0,0,1) with increasing carbon condensation rates, R(0,0,1)>R(0,1,0)>R(1,0,0), then the fiber will end up with a coil-shape. A 3-D model of this growth mechanism was plotted by Wen, et al. (Fig. 6.6) [146]. The three adjacent crystal planes are labeled in different shades, with the darker one having a higher fiber growth rate. Essentially, what happens is the resultant fibers will be growing towards the crystal planes having the lower fiber growth rates, and that is how the coiled shape forms. A qualitative model, based on an anisotropic deposition rate of carbon on catalyst surface was also posited by Amelinckx et al. [139].

But neither of these models make any predictions nor gives specific reasons for helical growth, maintaining that "rather special conditions" [139] would be needed for coiling. However, the faceting of catalyst particles has never been explicitly shown, and coiled tubules have also been obtained where catalyst particles are either not present anywhere in the nanostructure or have been found, through HRTEM, to be embedded [161] in the CNT. The above models also can not explain the synthesis of amorphous carbon nanocoils [162].

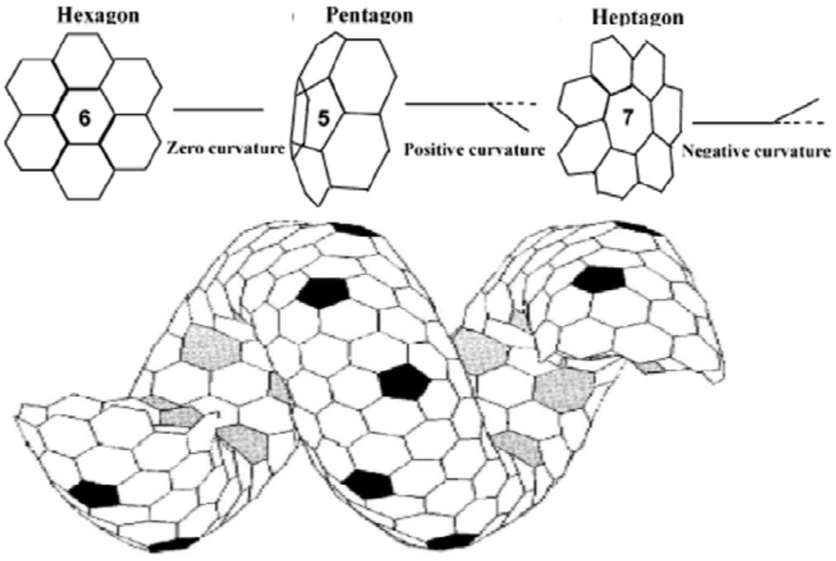

Fig. 6.5 Top: hexagonal, pentagonal, and heptagonal carbon ring structures in graphitic sheets [1].Bottom: Molecular model of a coiled SWCNT that has the lowest cohesive

energy per atom. The pentagon and heptagon (shaded) appear in the outer and inner ridge lines, respectively, amid a background of the hexagon rings [7].

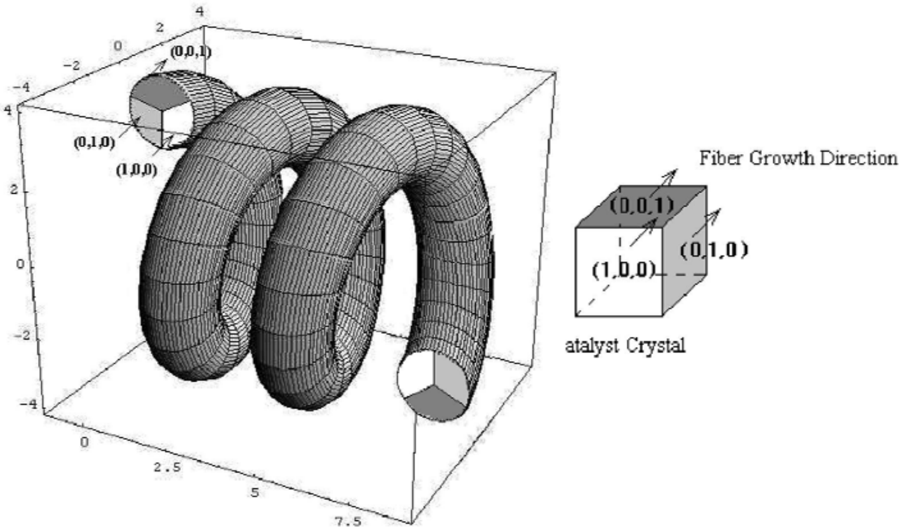

Fig. 6.6 3-D model for growth mechanism of coiled carbon nanofibers [146].

6.3.2 Thermodynamic model for coil/helix growth

The formation of helical patterns is postulated to arise from basic thermodynamic principles incorporating a minimization of the configurationally entropy. Computational studies [163-164] have also found that the *optimal* configuration for strings and nanowires is helical and spontaneous chirality due to entropic interactions [165] can be energetically preferred. Two scenarios would have to be considered in terms of nanocoil evolution and growth: (1) regular nanotube growth [166] convoluted with a subsequent helix inducing mechanism, or (2) nucleation and growth of a helical structure. It is generally seen in experiments that [160] (2) is favored, where the initial turn itself is a helix. This would imply a reduction in the entropy in the initial growth, which would have to be offset by some other mechanism. We hypothesize that an excluded volume interaction, due to the influence of the catalyst particles or the synthesis conditions in the CVD chamber, is responsible.

The following components are considered for the total Gibbs free energy, ΔG, of the growing nanostructure: (a) Elastic energy per unit length (E_e) of the HCNT/HCNW ($=Y\Pi/2R_c$) [Y is the Young modulus, Π, the moment of inertia, is proportional to $(r_0^4-r_i^4)$, where r_0 and r_i are the outer and inner radius of the tube (r_0-r_i, for a nanowire), and R_c the radius of curvature], (b) the enthalpy of interaction (ΔH) between the nanocoil and the ambient atmosphere, (c) the entropy of the system $(\Delta S = \Delta S_c + \Delta S_a)$, which includes the contributions from the coiling (ΔS_c) and the ambient (ΔS_a). In this simple model, coiling or non-linear growth is favored if the increased elastic energy and the decreased entropy due to the coiling is compensated by a decreased energy of interaction of the coil with the ambient and increased ΔS_a , i.e., if $\Delta G\ [= E_e + \Delta H - T(\Delta S_a + \Delta S_c)] < 0$. We suggest that such conditions can be favored by the use of specific catalyst particles and ambient agitation.

The enthalpy (ΔH) is modeled through the interaction between the ambient, (with catalyst particles of concentration, X_C) and the growing nanotube (X_T) as, $\Delta H = \Omega X_C X_T$, where Ω can be parametrized in terms of the interaction energies [167], as proportional to $E_{C\text{-}T} - ½\,(E_{C\text{-}C} - E_{T\text{-}T})$. $E_{C\text{-}T}$ is related to the adhesive energy of the catalyst (C) particles *vis-à-vis* the nanotube (T), and $E_{C\text{-}C}$ and $E_{T\text{-}T}$ are the respective cohesive energies. Consequently, Ω (ΔH) can be negative if the ambient conditions promote a non-wettability behavior, i.e., through catalyst particles that have a greater tendency for cohesion than adhesion onto the growing HCNT/HCNW. Increased entropy of the ambient, say through agitation, as has been observed through ultrasonic [168] microwave CVD [169], or use of sublimating compounds [138], has a similar effect. One can confirm specific cases where the above situations are plausible from comparison with experiment.

It has been shown that the use of certain catalysts (In [170], Sn or both [148]) or substrates (ITO [148, 171], powdered Ni [159] or Cu [153], Ge [154] Al_2O_3 [144]) enhances the nanocoil yield. One could explain this observation by positing the degree of wettability of the HCNT/HCNW surface by the catalysts/substrates as a criterion for coiling. It is seen that the wetting angle $\theta=\cos^{-1}[(\gamma_{sv}-\gamma_{sl})/\gamma_{lv}]$ of liquid metals with graphite surfaces [172] [γ represents the relative surface energies of the surface (*s*), liquid (*l*) metal, and the ambient vapor (*v*) phases] is large for the interaction of In (159 ^{o}), Sn (156 ^{o}), Cu (156 ^{o}), Ge (164 ^{o}), Al (159 ^{o}) while Fe, Co, and Ni, used for the growth of straight nano-tubes/wires all have smaller wetting angles (< 75 ^{o}). Consequently, the latter elements have a net attractive interaction with the growing nanostructure (exemplified through the Baker model [166]) surface while the former elements, by inducing a repulsive interaction, promote non-linear growth. Note that this model implies that the specific catalyst particles, say In, are only indirectly, and externally, responsible for the coiling and hence are not/need not be found in/on the nanostructure itself – as is often seen through EDS. The above model is summarized for the case of In particles, In Fig.6.7a schematically illustrates ambient conditions in the CVD chamber while Fig. 6.7b shows that the nonwetting In catalyst particles induce coiling/helix formation. A larger pitch is obtained when the In concentration in the CVD feedstock is reduced (Fig. 6.7b).

To justify the above theoretical analysis more rigorously, we formulate an empirical model for the synthesis of HCNT/HCNW forms. The overall growth and density of packing, in a nonlinear structure, is decomposed into the following: (a) a linear growth mode, (b) a bending mode, and (c) a twist mode. In a Cartesian coordinate system, the **X** and **Y** directions relate to the in-plane nanostructure growth, while the **Z** axis is the vertical/out-of-plane growth direction. The degree of growth (parametrized by *A*) is dictated by the supply of the growth catalyst (typically Fe, Co, and Ni) and is given by:

$$\nabla \cdot \mathbf{n} = A \tag{6.1}$$

where **n** denotes the directorial vector of growth and

$$\nabla = \mathbf{i}\frac{\partial}{\partial x} + \mathbf{j}\frac{\partial}{\partial y} + \mathbf{k}\frac{\partial}{\partial z} \tag{6.2}$$

In an *a priori* assumption, the bending is

$$\mathbf{n} \times (\nabla \times \mathbf{n}) = -A\mathbf{n} \tag{6.3}$$

which seems to be born out from experimental considerations (i.e., the bending increases with the length of the tube/wire). Finally the overall twist, $\mathbf{n} \cdot (\nabla \times \mathbf{n})$, is related to the differential rates of deposition in the plane (i.e., to $\nabla \cdot (\mathbf{n}_{\mathbf{x}} + \mathbf{n}_{\mathbf{y}})$), i.e.,

$$\mathbf{n} \cdot (\nabla \times \mathbf{n}) = \mathrm{A}[\nabla \cdot (\mathbf{n}_{\mathbf{x}} + \mathbf{n}_{y})] \tag{6.4}$$

Equation 6.4 follows from the observation that in a non-linear growth mode the rates of carbon deposition are very likely to be different in orthogonal directions. It should be noted that this relation makes a connection to a previous growth model [139], where compressive and tensile stresses caused by the uneven deposition of carbon were thought to be responsible for coiled growth. The bending and twist modes are induced by non-wetting catalyst particles, as outlined earlier.

We note that the above terms, viz., $\nabla\cdot\mathbf{n}$, $\mathbf{n}\times(\nabla\times\mathbf{n})$, and $\mathbf{n}\cdot(\nabla\times\mathbf{n})$ would contribute to the net elastic free energy [173] ($F_{elastic}$), where $F_{elastic}$ is related to

$$\int dV\left\{K_1(\nabla\cdot\mathbf{n})^2+K_2[\mathbf{n}\times(\nabla\times\mathbf{n})]^2+K_3[\mathbf{n}\cdot(\nabla\times\mathbf{n})]^2\right\}, \tag{6.5}$$

and K_1, K_2 and K_3 are the elastic constants corresponding to the different modes of growth.

As we have previously postulated that the avoidance of specific catalyst particles during the growing HCNT/HCNW is responsible for the promotion of non-linear growth, a chemical potential term, F_{chem} proportional to

$$\Gamma\int dV\,\mathbf{n}\cdot(\nabla\times\mathbf{n})+\mathbf{n}\times(\nabla\times\mathbf{n})\mathbf{n} \tag{6.6}$$

is also added to determine the overall free energy (ΔG) of an open system, where Γ is related to the HCNT/HCNW interactions with the ambient atmosphere.

After solving the above equations self consistently, we arrive at the following solutions for the components of the direction vector $\mathbf{n}(n_x, n_y, n_z)$ as,

$$n_x = A\cos^2(xt),\quad n_y = A\sin^2(xt),\quad n_z = A\,z, \tag{6.7}$$

where t is a parameter proportional to $\Gamma/(K_2+K_3)$ and dictates the magnitude of twist. Interestingly, and in accord with experiment, the growth mode as described through Eqn. 6.7 corresponds to helical growth.

We gain insight from the proposed model in that we learn that a variety of factors including the surface energy and the elastic constants, which are manifested through enthalpy and entropy considerations, influence non-linear nanostructure growth. Generally, coiled growth will be obtained when surface energy considerations are important while linear nanostructures are formed when elastic energy effects dominate. We can also predict that nanocoil growth can be favored by the use of non-wetting catalysts.

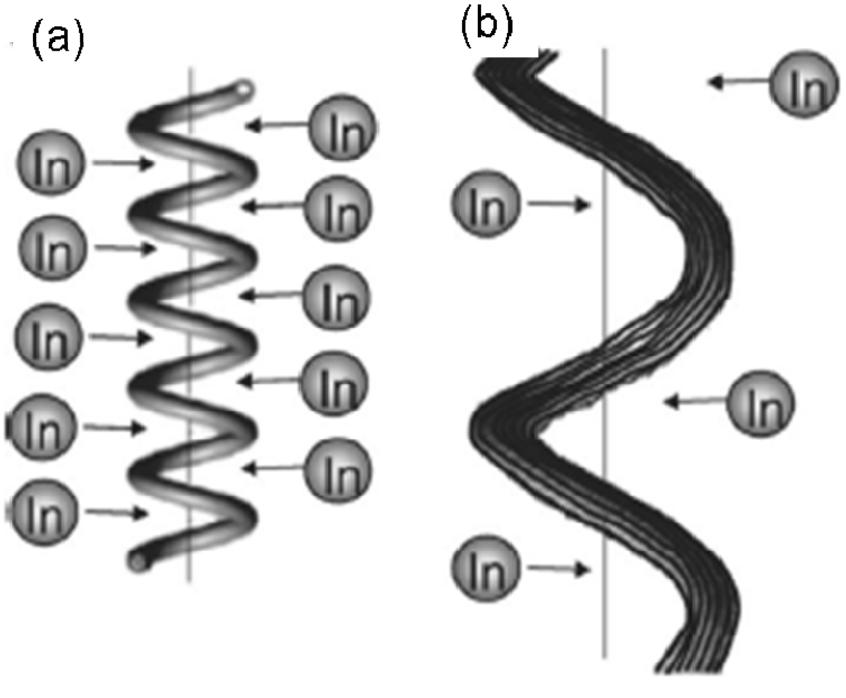

Fig. 6.7 The nowetting characteristic of the local indium catalyst particles on the nanotube/nanofiber surface is proposed as an underlying mechanism for the evolution of nanocoils/-helices (NC/NH). The concentration of In influences the coil pitch, where (i) a more tightly coiled helix is obtained at larger indium concentrations, and (ii) a helix with larger pitch is seen at smaller ambient Indium.

6.3.3 Growth mechanism for tubes and wires

We have, in general, found that In catalysts promote the growth of HCNT (Fig. 6.1) while Sn based catalysts catalyze the growth of HCNW (Fig. 6.2). The above observations can be related to the relative affinity of Sn or In with the primary transition metal catalyst: Fe. It is seen through an elementary analysis of the empirical Hume-Rothery rules [174] that Fe and Sn form substitutional solid solutions, i.e., due to similar values of the atomic radius (Fe: 0.172 nm, Sn: 0.172 nm) and the higher valence difference. On the other hand there is less tendency for mutual dissolution in a Fe-In mixture, i.e., due to a 16% atomic radius disparity (Fe: 0.172 nm, In: 0.200 nm). We also analyze these results in the context of the Fe-Sn and Fe-In binary equilibrium phase diagram [175]. In Fig. 6.8, we can see that around 973 K, there is negligible solubility in the Fe-In case (Fig. 6.8a) no matter the concentration ratio between Fe and In. On the other hand, for the Fe-Sn case, multiple Fe/Sn compounds may be formed during the CVD process, such as Fe_5Sn_3, Fe_3Sn_2, FeSn, and so on, if we consider the temperature gradient and the concentration distribution of catalysts during CVD process (Fig. 6.8b). This argument is further supported by the HRTEM studies, which reveal that the catalysts at the tip of HCNWs always have multiple crystal planes. Figure 6.9 shows an HRTEM image for a single HCNW. The left inset is an HRTEM image of sidewall with high magnification, which shows an amorphous structure. The right inset is an HRTEM image of the catalyst with high magnification, which shows multiple crystal planes. HCNTs are not as energetic stable as straight CNTs and their crystal structure changes very fast under a high energy electron beam (Figure 6.1), probably because of defects. Also, we fail to find any catalysts on the tip of HCNTs. So we cannot conduct similar HRTEM studies on HCNTs as we do on HCNWs. But we can use straight CNTs as a reference since HCNTs and CNTs have similar structure but different morphology. It is well know that CNTs have very good crystallinity (Fig.3.6 and 6.1), and catalysts at the tip of CNTs have a single crystal plane [176]. So, we propose the periodicity of the carbon atoms arrangement is affected by the lattice of the catalyst particle. In the case of HCNT, γ iron is the main catalyst [176], so we get CNT with good crystallinity. In the case of HCNW, a mixture of Fe/Sn compounds shows no periodic crystal structure, at least in long range, so amorphous HCNWs are synthesized.

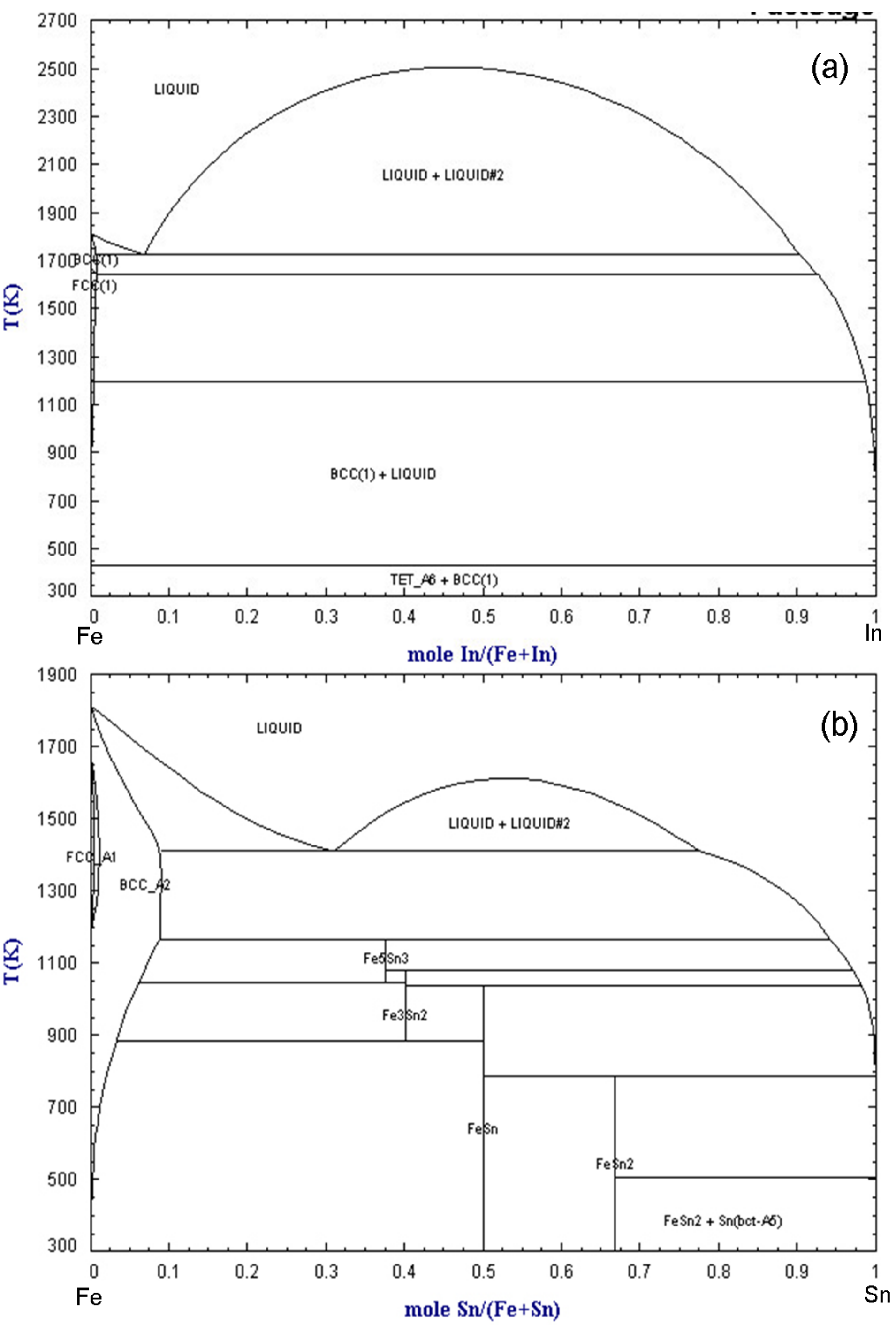

Fig. 6.8 Binary equilibrium phase diagram of Fe/In (a), and Fe/Sn (b) [175].

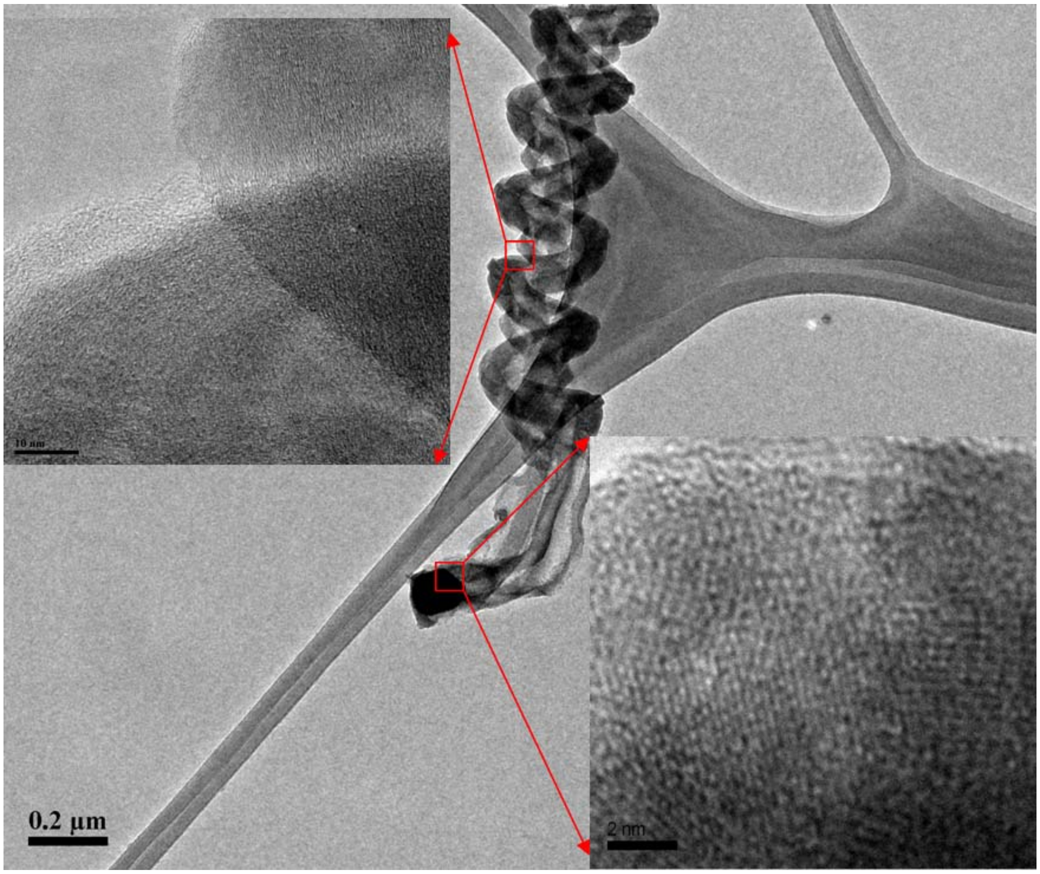

Figure 6.9 HRTEM images of single HCNW, wall (left inset) and catalyst (right inset).

6.3.4 Comparison with experiment results

We have verified some of the above hypotheses through our own CVD experiments. To further investigated the role of In in HCNT synthesis, we fix the atomic percentage of C, but change the atomic ratio between In/Fe. We found that decreasing of the In/Fe ratio decreases the coil pitch and coil diameter. Fig. 6.10 shows two typical SEM images of HCNT synthesized under same conditions except the concentration of indium. When the ratio of In/Fe is around 3 (Fig. 6.10a)), HCNTs show uniform pitch (~500 nm) and coil diameter (~300 nm,). But when the ratio of In/Fe is around 1.5, the pitch of HCNT is around 1000 nm and also some straight tubes can be found in the synthesized material. The coil diameters range from 0 (straight tube) to hundreds of nanometer (Fig. 6.10a). This is consistent with our model, and just as we predict in Fig. 6.7. We also examine the products of using Fe, In, and Sn as catalysts. We find that when a small amount of Sn added to the precursor, the synthesis rate of HCNTs increases dramatically (from less than 1 μm/min to 2 μm/min). Furthermore, with increasing atomic percent of Sn, the pitch of HCNTs decreases, in other words, CNTs become more "coiled". Finally, when the atomic percent of Sn exceeds 0.2 % (Sn/Fe+In+Sn), some HCNWs are also formed in our CVD system (Fig.6.11). Our models are qualitatively well supported by the experimental data.

(a) Low indium concentration

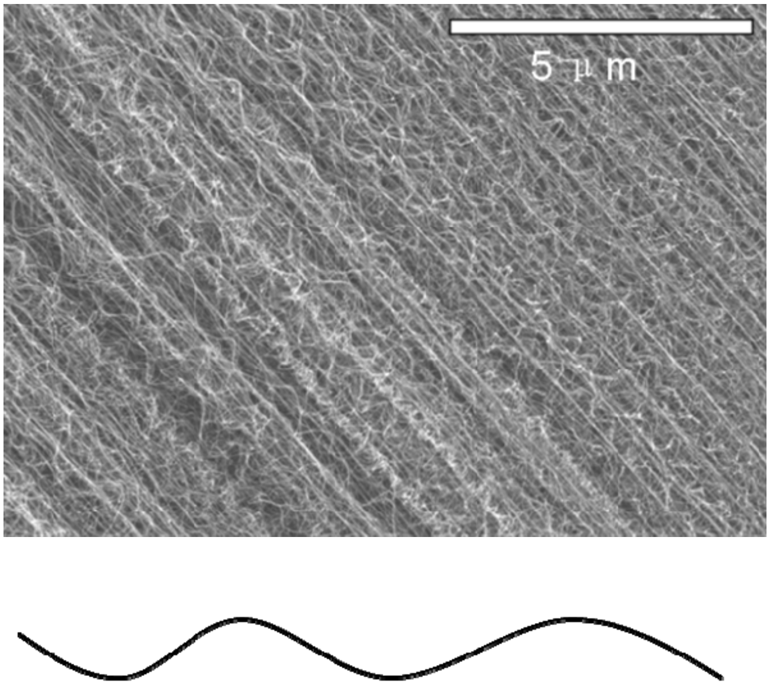

(b) High indium concentration

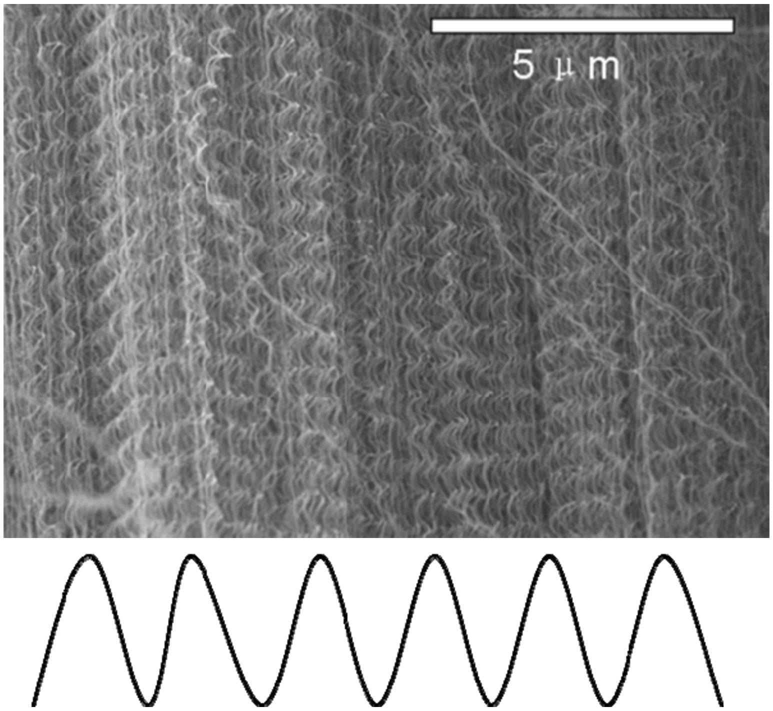

Fig. 6.10 Typical SEM images of HCNTs using different atomic concentration of Indium catalyst. (a) atomic ratio of In:Fe ~ 1.5. (b) atomic ratio of In:Fe ~ 3. Representative curves are drawled underneath the SEM images.

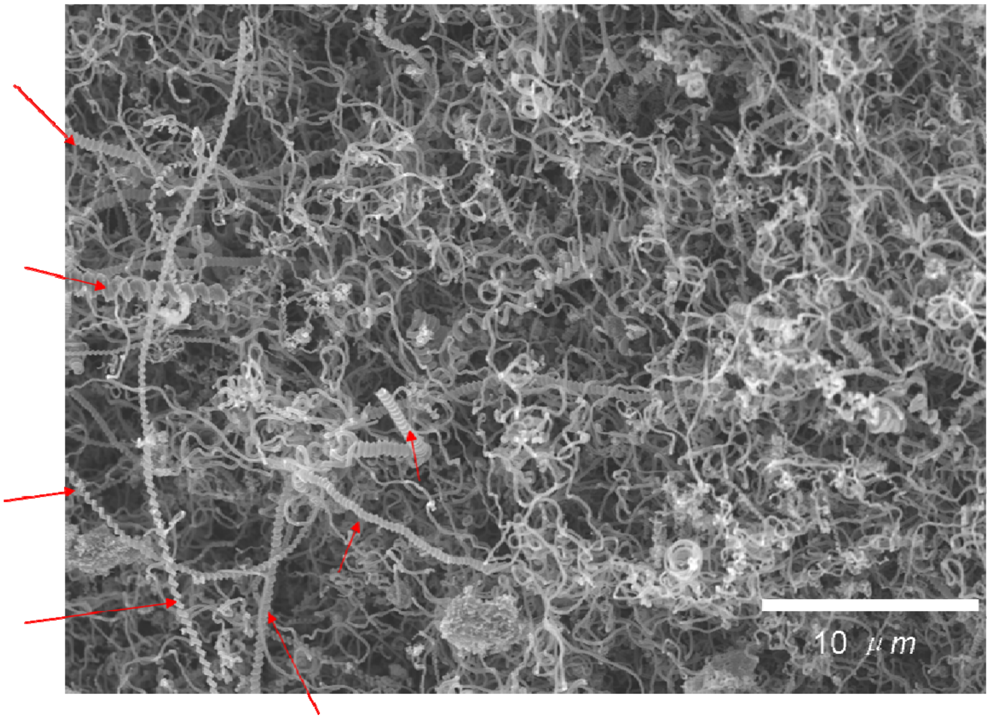

Fig. 6.11 A representative SEM image of HCNT/HCNW mixture by using Fe, In, and Sn as catalysts with atomic ratios: Fe/In/Sn=6:18:1.The carbon fibers with large diameter are HCNWs (labeled with red arrows) and the carbon fibers with small diameter are HCNTs.

6.4 Conclusion

We have demonstrated the rational synthesis of HCNTs and HCNWs through the use of In and Sn catalysts, respectively, in a floating-catalyst-based CVD process, using unpatterned quartz substrates. HCNTs exhibit uniform diameters and pitch, and could be readily peeled off for transfer onto other substrates. On the other hand, HCNWs are randomly aligned and widely distributed in geometry. We also proposed a plausible model for coiling in nanostructure growth motivated by both energy and entropic principles, that for a given volume of materials, the helical form occupies the least amount of space. To compensate for the close packing of the helices, the entropy of ambient atmosphere should increase which in turn is facilitated by nonwetting catalyst particles or induced by catalyst/ambient atomosphere agitation in CVD growth. The mutual solubility of Fe with Sn is also used to explain the synthesis mechanism of HCNW. Experiment results fit these models qualitatively very well.

CHAPTER SEVEN
CONCLUSION AND FUTURE OUTLOOK

SUMMARY

The work demonstrated in this dissertation focus on the inter-tube bonding and defects in the CNT network. The SPS system has been used to modify the morphology/ energy band structure of CNTs and therefore alter their transport properties. Aligned MWCNT bulk sample were prepared from pre-aligned MWCNT arrays and the SPS process. New defects, such as, kinks, corrugation, collapse of sidewalls in MWCNTs and inter-tube bonding between neighboring tubes were introduced as a result of the SPS treatment. The isotropic electrical transport properties and anisotropic thermal properties have been observed in aligned MWCNT bulk sample due to the inter-tube boding. The effect of SPS temperature on the transport properties of MWNCT BP was also explored. The resistivity of BP decreases with increasing SPS temperature in a way which can be well described in the framework of the percolation theory. The inter-tube bonding formed during the SPS process strengthen the EPC at low temperature and also introduces new scattering mechanisms for both electrons and phonon such as an unusual logarithmic behavior of $\rho(T)$ at low-T and the phonon drag effect around ~40 K in TEP. The transition from 1-D to 2-D character in thermal conductivity is nonetheless clear. Mixtures of boron compound and CNTs powder were also sintered using the SPS system. Raman spectra and the electrical measurements provide supporting evidence that the CNTs are doped with boron during the SPS process, which dramatically influence the electrical properties of CNTs. The plateau around 50 K in *ρ(T)*is tentatively attributed to portions of the boron doped CNTs exhibiting superconductivity at that temperature. For boron doped SWCNTs, we observe current dependence of normalized resistivity. These phenomena strongly suggest the present of the KA in our as-SPS samples. In this picture, multiple phonon drag effects, which are present in the samples sintered at high temperature, can be explained as the coupling between major/minor carriers and “Kohn” phonon. Phase transition at around 25 K in the preliminary magnetization measurements is also indicative of superconductivity in the boron doped CNTs. Due to the strong interfering background from the Fe catalysts, further magnetization studies are needed to confirm the presence of superconductivity in the boron doped CNTs.

As discussed in this dissertation, the SPS process is a post-synthesis process which promotes inter-tube bonding in CNTs. In another system, we study the defects which may be periodically inserted into carbon network during the nanotube synthesis. HCNTs and HCNWs were synthesized through the use of In and Sn catalysts, respectively, in a floating-catalyst-based CVD process. Bare quartz substrates were used during the synthesis which takes us a step closer to the commercial realization for production of carbon nanocoils. HCNTs with uniform diameters and pitch self-assemble into a film which can be readily peeled off for transfer onto other substrates. On the other hand, HCNWs, are randomly aligned and exhibit a broader distribution in their diameters and pitch. We also propose a plausible thermodynamic model for these coiled nanostructures. Nonwetting character of the catalysts is shown to play an important role in the coiling mechanism.

Future Work

Theoretically, KA is expected to be present in the graphite/CNT system. However, there are few reports which provide experimental evidences. In this dissertation, we show evidence for the KA in our as-SPSed CNTs using electrical transport data. Additional evidence must be sought through elucidation of phonon characteristics (for example, a change in the frequency of phonon due to strengthened or weakened electron-phonon coupling). Raman spectroscopy is a good tool for exploring this evidence; therefore investigating the relation between G′ band frequency and its FWHM as a function of the excitation wavelength will be pursued.

Using the SPS process to dope CNTs with boron, nitrogen, phosphorous or sulfur, and investigating their superconducting properties will also be pursued. At the present time, the presence of a large amount of Fe catalyst particles in boron doped CNTs is impeding magnetization studies to confirm the presence or absence of superconductivity in our samples. Synthesizing CNTs using the non-magnetic catalysts, or developing an efficient purification process is crucial.

Finally, it should be mentioned that this dissertation focused solely on the synthesis of HCNTs and HCNWs. Further studies on the mechanical and electrical properties of these coiled nanostructures are desired. An in-depth understanding of the fundamental properties will lead to several applications of coiled nanostructures in electromagnetic shielding, structural foams for cushioning, energy dissipation and smart polymer composites.

REFFERENCES

1. M. Lu, H.L. Li, and K.T. Lau, *J. Phys. Chem. B* **108**, 6186 (2004).

2. S. Iijima *Nature* **354**, 56 (1991).

3. R. Saito, G. Dresselhaus, M. S. Dresselhaus, , *Physical Properties of Carbon Nanotubes* Imperial College Press, London, 1998.

4. P. Delaney, H. J. Choi, J. Ihm, *et al.*, *Nature* **391**, 466 (1998).

5. M. Ouyang, J. L. Huang, C. L. Cheung, *et al.*, *Science* **292**, 702 (2001).

6. Charlier, J. C. *Acc. Chem. Res.* **35**, 1063 (2002).

7. S. Ihara, S. Itoh and J. Kitakami *Phys. Rev. B* **48**, 5643 (1993).

8. L. V. Radushkevich, V. M. Lukyanovich *Zum. Fisic. Chim.* **26**, 88 (1952).

9. H. W. Kroto, J. R. Heath, S. C. O' Brien, et al. *Nature* **318**, 162 (1985).

10. Thomas W. Ebbesen *Physics Today* **49**, 26 (1996).

11. S. Iijima, T. Ichihashi *Nature* **363**, 603 (1993).

12. D. S. Bethune, C. H. Kiang, M. S. de Vries, *et al.*, *Nature* **363**, 605 (1993).

13. M. S. Dresselhaus, G. Dresselhaus, and R. Saito, *Carbon* **33**, 883 (1995).

14. J-C. Charlier, X. Blase, S. Roche, *Rev. Mod. Phys.* **79**, 677 (2007).

15. H. Dai *Acc. Chem. Res.* **35**, 1035 (2002).

16. Endo, M., S. Iijima, and M. S. Dresselhaus, *Carbon Nanotubes* Elsevier, 1996.

17. P. R. Wallace *Phys. Rev.* **71**, 622 (1947).

18. R. Saito, G. Dresselhaus, M. S. Dresselhaus, *Appl. Phys. Lett.* **60**, 2204 (1992).

19. J. C. Charlier, X. Gonze, J. P. Michenaud, *Euro- Phys. Lett.* **29**, 43 (1995).

20. S. Reich, C. Thomsen, and P. Ordejon, *Phys. Rev. B* **65**, 155411 (2002).

21. Y. K. Kwon, D. Tomanek *Phys. Rev. B* **58**, R16001 (1998).

22. Y-K. Kwon, D. Tomanek *Phys. Rev. B* **58**, R16001 (1998).

23. M. Endo, H. Muramatsu, T. Hayashi, *et al.*, *Nano Lett.* **5**, 1099 (2005).

24. F. Banhart *Rep. Prog. Phys.* **62**, 1181 (1999).

25. J. Li, F. Banhart *Nano Lett.* **4**, 1143 (2004).

26. J. A. Rodriguez-Manzo, F. Banhart *Nano Lett.* **9**, 2285 (2009).

27. G. Lee, C. Z. Wang, E. Yoon, *et al.*, *Appl. Phys. Lett.* **92**, 043104 (2008).

28. P. Lambin, A. Fonseca, J. P. Vigneron, *et al.*, *Chem. Phys. Lett.* **245**, 85 (1995).

29. R. Saito, M. S. Dresselhaus, G. Dresselhaus, *Phys. Rev. B* **53**, 2044 (1996).

30. J. C. Charlier, T. W. Ebbesen, Ph. Lambin, *Phys. Rev. B* **53**, 11108 (1996).

31. L. Chico, V. H. Crespi, L. X. Benedict, *et al.*, *Phys. Rev. Lett.* **76**, 971 (1996).

32. M. Terrones, H. Terrones, F. Banhart, et al., *Science* **288**, 1226 (2000).

33. H. R. Gutirrez, U. J. Kim, J. P. Kim. *et al.*, *Nano Lett.* **5**, 2195 (2005).

34. K. McGuire, N. Gothard, P. L. Gai, *et al.*, *Carbon* **43**, 219 (2005).

35. W. Han, Y. Bando, K. Kurashima, *et al.*, *Chem. Phys. Lett.* **299**, 368 (1999).

36. R. Czerw, M. Terrones, J.-C. Charlier, *et al.*, *Nano Lett.* **1**, 457 (2001).

37. N. Murata, J. Haruyama, J. Reppert, *et al.*, *Phys. Rev. Lett.* **101**, 027002 (2008).

38. D. L. Carroll, Ph. Redlich, X. Blase, *et al.*, *Phys. Rev. Lett.* **81**, 2332 (1998).

39. Y. -M. Choi, D. -S. Lee, R. Czerw, *et al.*, *Nano Lett.* **3**, 839 (2003).

40. J. W. G. Wildoer, L. C. Venema, A. G. Rinzler, *et al.*, *Nature* **391**, 59 (1998).

41. T. W. Odom, J. Huang, P. Kim, *et al.*, *Nature* **391**, 62 (1998).

42. S. J. Tans, M. H. Devoret, H. Dai, *et al.*, *Nature* **386**, 474 (1997).

43. M. Bockrath, D. H. Cobden, J. Lu, *et al.*, *Nature* **397**, 599 (1999).

44. T. W. Ebbesen, H. J. Lezec, H. Hiura, *et al.*, *Nature* **381**, 678 (1996).

45. L. Langer, V. Bayot, E. Grivei, *et al.*, *Phys. Rev. Lett.* **76**, 479 (1996).

46. A. Bachtold, C. Strunk, J-P. Salvetat, *et al.*, *Nature* **397**, 673 (1999).

47. C. T. White, T. N. Todorov *Nature* **393**, 240 (1998).

48. S. Frank, P. Poncharal, Z. L. wang, *et al.*, *Science* **280**, 1744 (1998).

49. J. Kong, E. Yenilmez, T. W. Tombler, *et al.*, *Phys. Rev. Lett.* **87**, 106801 (2001).

50. P. G. Collins, M. Hersam, M. Arnold, *et al.*, *Phys. Rev. Lett.* **86**, 3128 (2000).

51. A. Y. Kasumov, R. Deblock, M. Kociak, *et al.*, *Science* **284**, 1508 (1999).

52. M. Kociak, A. Y. Kasumov, S. Gueron, *et al.*, *Phys. Rev. Lett.* **86**, 2416 (2001).

53. Z. K. Tang, L.Zhang, N. Wang, *et al.*, *Science* **292**, 2462 (2001).

54. R. Lortz, Q. Zhang, W. Shi, *et al.*, *PNAS* **106**, 7299 (2009).

55. I. Takesue, J. Haruyama, N. Kobayashi, *et al.*, *Phys. Rev. Lett.* **96**, 057001 (2006).

56. N. Murata, J. Haruyama, Y. Ueda, et al., *Phys. Rev. B* **76**, 245424 (2007).

57. N. W. Ashcroft, N. D. Mermin, *Solid State Physics* Harocurt Brace, New York, 1976.

58. D. Bernaerts, X. B. Zhang, X. F. Zhang, *et al.*, *Philos. Mag.* **71**, 602 (1995).

59. L. X. Bendict, S. G. Louie, M. L. Cohen, *Solid State Commun.* **100**, 177 (1996).

60. S. Berber, Y. K. Kwon, D. Tomanek, *Phys. Rev. Lett.* **84**, 4613 (2000).

61. P. Kim, L. Shi, A. Majumdar, *et al.*, *Phys. Rev. Lett.* **87**, 215502 (2001).

62. C. Yu, L. Shi, Z. Yao, *et al.*, *Nano Lett.* **5**, 1842 (2005).

63. D. Wang, P. Song, C. Liu, *et al.*, *Nanotechnology* **19**, 075609 (2008).

64. H. Zhang, J. Li, B. Zhang, *et al.*, *Phys. Rev. B* **75**, 205407 (2007).

65. I. Ivanov, A. Puretzky, G. Eres, *et al.*, *Appl. Phys. Lett.* **89**, 223110 (2006).

66. R. S. Prasher, X. J. Hu, Y. Chalopin, *et al.*, *Phys. Rev. Lett.* **102**, 105901 (2009).

67. F. J. Blatt, P. A. Schroeder, C. L. Foiles, *et al.*, *Thermoelectric power of metals* Plenum Press, New York, 1976.

68. A. B. Kaiser *Adv. Mater.* **13**, 927 (2001).

69. Y. W. Park, A. J. Heeger, M. A. Druy, *et al.*, *J. Chem. Phys.* **73**, 946 (1980).

70. J. Hone, I. Ellwood, M. Muno, *et al.*, *Phys. Rev. Lett.* **80**, 1042 (1998).

71. L. Grigorian, G. U. Sumanasekera, A. L. Loper, *et al.*, *Phys. Rev. B* **60**, R11309 (1999).

72. K. Bradley, S. Jhi, P. G. Collins, *et al.*, *Phys. Rev. Lett.* **85**, 4361 (2000).

73. N. Kang, L. Lu, W. J. Kong, *et al.*, *Phys. Rev. B* **67**, 033404 (2003).

74. W. J. Kong, L. Lu, H. W. Zhu, *et al.*, *J. Phys.: Condens. Mat.* **17**, 1923 (2005).

75. B. Sadanadan, T. Savage, S. Bhattacharya, *et al.*, *J. Nanosci. Nanotech.* **3**, 99 (2003).

76. N. Hamada, S.-I. Sawada, A. Oshiyama, *Phys. Rev. Lett.* **68**, 1579 (1992).

77. H. E. Romero, G. U. Sumanasekera, G. D. Mahan, *et al.*, *Phys. Rev. B* **65**, 205410 (2002).

78. J. Vavro, M. C. Llaguno, J. E. Fischer, *et al.*, *Phys. Rev. Lett.* **90**, 065503 (2003).

79. V. W. Sarola, G. D. Mahan *Phys. Rev. B* **66**, 205405 (2002).

80. P. Bandaru, C. Daraio, K. Yang *et al.*, *J. Appl. Phys.* **101**, 094307

81. M. Terrones, F. Banhart, N. Grobert, *et al.*, *Phys. Rev. Lett.* **89**, 075505 (2002).

82. C. Jin, K. Suenaga, S. iijima, *Nat. Nanotechnology* **3**, 17 (2008).

83. T. Gong, Y. Zhang, W. Liu, *et al.*, *Diamond Relat. Mater.* **17**, 158 (2008).

84. L. Jiao, L. Zhang, X. Wang, *et al.*, *Nature* **458**, 877 (2009).

85. F. Zhang, J. Shen, J. Sun, *et al.*, *Carbon* **43**, 1254 (2005).

86. X. Qi, Q. Bao, C. M. Li, *et al.*, *Appl. Phys. Lett.* **92**, 113113 (2008).

87. V. Ivanov, J. B. Nagy, Ph. Lambin *et al.*, *Chem. Phys. Lett.* **223**, 329 (1994).

88. R. Andrews, D. Jacques, A. M. Rao, *et al.*, *Chem. Phys. Letters,* **303**, 467 (1999).

89. G. Zhang, D. Mann, L. Zhang, *et al.*, *PNAS* **102**, 16141 (2005).

90. W. Wang, K. Yang, J. Gaillard, *et al.*, *Adv. Mater.* **20**, 179 (2008).

91. A. L. Pope, B. Zawilski, and T. M. Tritt, *Cryogenics* **2001**, 725 (2001).

92. A. L. Pope, R. T. Littleton IV, and T. M. Tritt, *Rev. Sci. Instrum.* **72**, 3129 (2001).

93. K. Sato, R. Saito, Y. Oyama, *et al.*, *Chem. Phys. Lett.* **427**, 117 (2006).

94. M. Endo, Y. A. Kim. T. Hayashi, et al., *Small* **2**, 1031 (2006).

95. I. Maciel, N. Anderson, M. A. Pimenta, *et al.*, *Nat. Mater.* **7**, 878 (2008).

96. J. Hone, M. C. Liaguno, N. M. Nemes, *et al.*, *Appl. Phys. Lett.* **77**, 666 (2000).

97. W. Y. Jang, N. N. Kulkarni, C. K. Shih, *et al.*, *Appl. Phys. Lett.* **84**, 1177 (2004).

98. M. Tsai, C. Yu, C. Yang, *et al.*, *Appl. Phys. Lett.* **89**, 192115 (2006).

99. B. L. Altshuler, A. G. Aronov *Pis'ma Zh Eksp Teor Fiz* **27**, 700 (1978).

100. K. Sugihara, H. Ohshima, K. Kawamura, *et al.*, *J. Phys. Soc. Jpn.* **43**, 1664 (1977).

101. C. Ayache, Ade Combarieu, J. P. Jay-Gerin, *Phys. Rev. B* **21**, 2462 (1980).

102. G. Baumgartner, M. Carrard, L. Zuppiroli, *et al.*, *Phys. Rev. B* **55**, 6704 (1997).

103. A. Mizel, L. X. Benedict, M. L. Cohen, *et al.*, *Phys. Rev. B* **60**, 3264 (1999).

104. D. J. Yang, Q. Zhang, G. Chen, *et al.*, *Phys. Rev. B* **66**, 165440 (2002).

105. A. Javey, J. Guo, M. Paulsson, et al., *Phys. Rev. Lett.* **92**, 106804 (2004).

106. P. N. Nirmalraj, P. E. Lyons, S. De *et al.*, *Nano Lett.* (Published online) (2009).

107. R. Zallen, *The physics of amorphous solids* John Wiley & Sons, Inc, New York, 1983.

108. U. Dettlaff-Weglikowska, V. Skakalova, R. Graupner, *et al.*, *Mat. Res. Symp. Proc.* **772**, M3.1.1 (2003).

109. L. Hu, D. S. Hecht, G. Gruner, *Nano Lett.* **4**, 2513 (2004).

110. G. Stauffer, *Introduction to Percolation Theory* Taylor & Francis, London, 1985.

111. J. Sandler, J. Kirk, I. Kinloch, *et al.*, *Polymer* **44**, 5893 (2003).

112. B. Kim, J. Lee, I. Yu, *J. Appl. Phys.* **94**, 6724 (2003).

113. J. Kondo *Prog. Theor. Phys.* **32**, 37 (1964).

114. A. B. Kaiser, G. Dusberg, S. Roth, *Phys. Rev. B* **57**, 1418 (1998).

115. R. Ricardo da Silva, H. H. S. Torres, Y. Kopelevich, *Phys. Rev. Lett.* **87**, 147001 (2001).

116. D. Das and S. Doniach *Phys. Rev. B* **57**, 14440 (1998).

117. J. Hone, M. C. Llaguno, M. J. Biercuk, et al., *Appl. Phys. A* **74**, 339 (2002).

118. P. Castrucci, M. Scarselli, M. De Crescenzi, *et al.*, *Appl. Phys. Lett.* **85**, 3857 (2004).

119. B. T. Kelly, *Physics of Graphite* Applied Science, London, 1981.

120. D. K. C. MacDonald, *Thermoelectricity* Wiley, New York, 1962.

121. M. S. Dresselhaus, G. Dresselhaus and A. Jorio, *Carbon Nanotubes: New Topics in the Synthesis, Structure, Properties and Applications* Springer, New York, 2008.

122. P. M. Rafailov, J. Maultzsch, C. Thomsen, et al., *Nano Lett.* **9**, 3343 (2009).

123. M. Matsudaira, J. Nakamura, T. Shimizu, *et al.*, *J. Phys.: Conf. Ser.* **153**, 012070 (2009).

124. H. Farhat, H. Son, Ge. G. Samsonidze, *et al.*, *Phys. Rev. Lett.* **99**, 145506 (2007).

125. S. Piscanec, M. Lazzeri, F. Mauri, *et al.*, *Phys. Rev. Lett.* **93**, 185503 (2004).

126. R. Klesse *Phys. Rev. B* **66**, 085409 (2002).

127. S. Motojima, X. Chen, S. Yang, *et al.*, *Diamond Relat. Mater.* **13**, 1989 (2003).

128. J. Du, C. Sun, S. Bai, *et al.*, *J. Mater. Res.* **17**, 1232 (2002).

129. M. Fujii, M. Matsui, S. Motojima, *et al.*, *J. Cryst. Growth* **237-239**, 1937 (2002).

130. C. Daraio, V. F. Nesterenko, S. Jin, *et al.*, *J. Appl. Phys.* **100**, 064309 (2006).

131. X. Chen, S. Zhang, D. A. Dikin, *et al.*, *Nano Lett.* **3**, 1299 (2003).

132. S. Zhang *Nat. Biotechnol* **21**, 1171 (2003).

133. P. R. Badaru, C. Daraio, S. Jin, *et al.*, *Nat. Mater.* **4**, 663 (2005).

134. P. R. Bandaru *J. Nanosci. Nanotechnol.* **7**, (2007).

135. B. I. Dunlap *Phys. Rev. B* **46**, 1933 (1992).

136. X. B. Zhang, X. F. Zhang, D. Bernaerts, *et al.*, *Europhys Lett.* **27**, 141 (1994).

137. Kin Tak Lau, Mei Lu, and David Hui *Composites: Part B* **37**, 437 (2006).

138. J. Liu, S. Webster, and D. L. Carroll, *Appl. Phys. Lett.* **88**, 213119 (2006).

139. S. Amelinckx, X. B. Zhang, D. Bernaerts, *et al.*, *Science* **265**, 635 (1994).

140. G. Diaz, M. Benaissa, J. G. Santiesteban, and M. Jose-Yacaman, *Fullerene science and technology* **6**, 853 (1998).

141. C.J. Su, D.W. Hwang, S.H. Lin, *et al.*, *Phys. Chem. Commun.* **5**, 34 (2002).

142. S.M. Huang, and L.M. Dai *J. Nanoparticle Res.* **4**, 145 (2002).

143. D. Pradhan, and M. Sharon *Mater. Sci. Eng. B* **96**, 24 (2002).

144. S. Takenaka, M. Ishida, M. Serizawa, et al., *J. Phys. Chem. B* **108**, 11464 (2004).

145. J. N. Xie, K. Mukhopadyay, J. Yadev, et al., *Smart Mater. Struct.* **12**, 744 (2003).

146. Y. Wen, and Z. Shen *Carbon* **39**, 2369 (2001).

147. N. Grobert, M. Terrones, S. Trasobares, *et al.*, *Appl. Phys. A Mater.* **70**, 175 (2000).

148. L. J. Pan, M. Zhang, and Y. Nakayama, *J. Appl. Phys.* **91**, 10058 (2002).

149. L.J. Pan, T. Hayashida, M. Zhang, *et al.*, *Jpn. J. Appl. Phys.* **40**, L235 (2001).

150. H.Q. Hou, Z. Jun, F. Weller, *et al.*, *Chem. Mater.* **15**, 3170 (2003).

151. V. Bajpai, L.M. Dai, and T. Ohashi, *J. Am. Chem. Soc.* **126**, 5070 (2004).

152. J. F. AuBuchon, L. H. Chen, A. I. Gapin,*et al.*, *Nano Lett.* **4**, 1781 (2004).

153. H. Takikawa, M. Yatsuki, R. Miyano, *et al.*, *Jpn. J. Appl. Phys.* **39**, 5177 (2000).

154. J. M. Mao and S. S. Xie *J. Mater. Sci. Lett.* **18**, 1151 (1999).

155. J. B. Bai *Mater. Lett.* **57**, 2629 (2003).

156. D. Y. Zhong, S. Liu, and E. G. Wang, *Appl. Phys. A Mater.* **83**, 4423 (2003).

157. C. N. R. Rao, A. Govindaraj, *Nanotubes and Nanowires* Royal Society of Chemistry, London, UK, 2005.

158. K. A. Dill and S. Bromberg, *Molecular Driving Forces: Statitical Thermodynamics in Chemistry and Biology* Garland Science, New York, 2003.

159. S. Motojima, M. Kawaguchi, K. Nozaki, *et al.*, *Appl. Phys. Lett.* **56**, 321 (1990).

160. S. Motojima, and Q. Chen *J. Appl. Phys.* **85**, 3919 (1999).

161. R. Gao, Z. L. Wang, and S. Fan, *J. Phys. Chem. B* **104**, 1227 (2000).

162. Y. Qin, X, Jiang, and Z. Cui, *J. Phys. Chem. B* **109**, 21749 (2005).

163. O. Gulseren, F. Ercolessi, and E. Tosatti, *Phys. Rev. Lett.* **80**, 3775 (1998).

164. A. Maritan, C. Micheletti, A. Trovato, *et al.*, **406**, 287 (2000).

165. G. T. Pickett, M. Gross, and H. Okuyama, *phys. Rev. Lett.* **85**, 3652 (2000).

166. R. T. K. Baker *Carbon* **27**, 315 (1989).

167. D. A. Porter and K. E. Easterling, *Phase Transformations in Metals and Alloys* Nelson Thornes, Cheltenham, UK, 1992.

168. C. Kuzuya, Y. Hishikawa, and S. Motojima, *J. Chem. Eng. Jpn.* **35**, 144 (2002).

169. V. K. Varadan and J. Xie *Smart Mater. Struct.* **11**, 728 (2002).

170. L. Pan, T. Hayashida, A. Harada, *et al.*, *Physica B* **323**, 350 (2002).

171. M. Zhang, Y. Nakayama, and L.J. Pan, *Jpn. J. Appl. Phys.* **39**, L1242 (2000).

172. R. A. Munson *Carbon* **5**, 471 (1967).

173. P. M. Chaikin and T. C. Lubensky, *Principles of Condensed Matter Physics* Cambridge University Press, New York,, 1995.

174. W. B. Pearson, *Handbook of Lattice Spacings and Structures of Metals* Pergamon, London, 1958.

175. H. Okamoto, *Binary Alloy Phase Diagrams* ASM International, Materials Park, OH, 1990.

176. A. Khasanov, J. He, J. Gaillard, *et al.*, *Appl. Phys. Lett.* **93**, 013103 (2008).